공학박사 학위논문

Investigation of Cu Electroless Deposition Mechanism Using OCP Measurement with QCM for the Application to Cu Damascene Process in Semiconductor Fabrication

구리 무전해 도금의 반도체 구리 다마신 공정에의 적용을 위한

OCP 측정과 **QCM**을 통한 구리 무전해 도금 메커니즘 연구

2013년 2월

서울대학교 대학원

화학생물공학부

임 태 호

Abstract

Semiconductor process has been dramatically developed by introducing Cu damascene process, which enables the replacement of Al to Cu as interconnection material. The development continues to improve the performance of devices, and it is achieved by scaling up of chip integration so far. However, recently, the reduction of Cu line width according to the integration makes it difficult to deposit both diffusion barrier and seed layer uniformly inside of narrow trenches and vias using conventional physical vapor deposition. Thus, alternative deposition methods are suggested to solve the problem, such as atomic layer deposition and electroless deposition. Cu electroless deposition attracts a lot of attention for the use of the next generation metallization method because the direct deposition is possible on both the conventional diffusion barriers and the next generation diffusion barriers such as Ru-alloy or Co-ally. In this study, the electrochemical real-time observation method for the Cu electroless deposition was designed: both the open-circuit potential and mass change of an electrode were measured simultaneously during the deposition. Using the method, the Cu electroless deposition could be investigated in detail, such as the mechanism of Cu electroless deposition and the adsorption behaviors of organic additives. Based on the study, the electroless bottom-up filling of sub-60 nm trenches was finally achieved, confirming the possibility that the Cu electroless deposition could be used for the next generation metallization method.

In the investigation of Cu electroless deposition, the effect of each component in the

electroless bath on Cu surface was understood preferentially. It was observed that the Cu was continuously oxidized in the alkaline bath. However, when ethylenediaminetetraacetic acid, a well-known complexing agent, was in the solution together, it was found to participate in the removal of Cu oxides formed on the surface as well as the complexation of Cu ions in the solution. Formaldehyde, a reducing agent, was adsorbed onto the Cu surface and inhibited further Cu oxidation. Both components maintained low oxygen content on the Cu surface in the alkaline solution. During the Cu electroless deposition process, the induction period was observed at the initial stage of the deposition and it was related with the time that the formaldehyde was adsorbed and became activated on the surface, indicating that the oxidation of formaldehyde was the rate-determining step. The effect of Cu oxides on the electroless Cu film was also investigated. It was revealed that the formaldehyde rarely adsorbed on the oxidized Cu surface unless the ethylenediaminetetraacetic acid removed the oxide by the complexation. The same phenomenon was observed in the real electroless deposition. The pre-formed Cu oxide caused the rough surface of electrolessly deposited film, resulting from the irregular adsorption of formaldehyde.

The effect of additive was investigated by injecting additives during the deposition. Additives were polyethylene glycol (PEG), 2,2'-dipyridyl, and 3-N,N-dimethylaminodithiocarbamoyl-1-propanesulfonic acid (DPS). The addition of PEG during the deposition caused the reduction of the deposition rate as the PEG was gradually adsorbed on the surface. It was revealed that the adsorption of PEG blocked active sites for the formaldehyde adsorption, resulting in the

suppression effect. The adsorption kinetics of PEG was strongly dependent on the diffusion coefficient of PEG, which was directly related to the molecular weight. It followed the adsorption-controlled kinetics when the diffusion coefficient was high, whereas that of PEG with low diffusion coefficient showed the diffusion-controlled kinetics. The strength of the suppression effect was also affected by the molecular weight of PEG: increasing the molecular weight enhanced the suppression effect. The adsorption behaviors of 2,2'-dipyridyl and DPS were also studied. 2,2'-dipyridyl was found to adsorb on the surface fast and reduce the deposition rate immediately. DPS was also adsorbed, accelerating or inhibiting the deposition according to its concentration. It was revealed that the suppression effect was enhanced when both 2,2'-dipyridyl and DPS were added together. The electroless filling was then performed on sub-60 nm trenches by using the suppression enhancement. The simple concentration optimization of two additives achieved the bottom-up filling.

Keywords: Cu, electroless deposition, additive, bottom-up filling, deposition mechanism

Student number: 2009-30249

Contents

List of Tables

List of Figures

Chapter I. Introduction

1.1. Metallization in ULSI technology

1.1.1. Cu damascene process

In the fabrication of integrated semiconductor processing chips, ultra large scale integration (ULSI) technology has been continuously developed as the demand for the fast operation speed keeps increasing. The integration process can not only increase the signal transfer speed in devices by decreasing the total length of signal path but reduce the unit chip price by increasing the total number of chips per a wafer.[1] There are two main factors affecting the signal speed, gate delay and resistance-capacitance delay (RC delay). The gate delay is the time delay between the signal input and output at the gate, while the RC delay is the delay caused by both the resistance of metal lines, which the signal current passes through, and the capacitance of dielectric. In 1990s, the decrease in the gate delay by the integration reduced the total signal delay because the length of metal lines in a chip was relatively short. However, as the total length of metal lines in a chip has been dramatically increased with the decrease of the cross-sectional area, the RC delay takes up the large portion of the total signal delay as shown in Figure 1.1 and Figure 1.2.[2,3,4,5] Therefore, the reduction of both the resistance and capacitance becomes main issues in the present metallization process.

One of main changes in the metallization for reducing the RC delay is the replacement of Al

to Cu as the interconnection material. Table 1 listed physical properties of Cu, Ag, and Al. Cu has lower bulk resistivity (1.67 μΩ·cm) than that of Al (2.66 μΩ·cm): the low resistivity of Cu directly reduces the RC delay. [6] Cu is also advantageous in the view of the heat dissipation during chip operation. Cu lines consume lower power than Al because of its low resistivity, resulting in less heat generation. Furthermore, Cu has the superior electromigration resistance compared to that of Al. The electromigration is the phenomena that the transport of material is caused by the gradual movement of the ions in a conductor due to the momentum transfer between conducting electrons and diffusing metal atoms. In highly integrated circuits, the electromigration is a serious problem because the cross-sectional area of metal lines is small, leading to high current density as shown in Figure 1.2. The electromigration may cause the disconnection or short circuit after the long-term operation. The electromigration resistance of Cu is much higher than Al, thus, Cu improves the reliability of the metal lines toward the breakdown by the electromigration.[7,8]

The replacement of Al to Cu brought out the huge change in the metallization process. In Al metallization, subtractive etching is used for the patterning of metal lines.[9] The flow chart of the subtractive etching is depicted in Figure 1.3 (a). An Al film is deposited on the whole wafer surface first, which is selectively protected with a masking layer such as photoresist. Dry etching like reactive ion etching then removes the film from the unprotected regions. After the patterning of Al film, dielectric is deposited on it. The repetition of such a series of processes forms the multilevel metal lines. However, the procedure explained so far is not applicable to

the Cu metallization because the by-products formed during the dry etching of Cu is not so volatile as those of Al, causing the difficulty in the residue removal. Therefore, damascene process is introduced to the Cu metallization.[10] The desired interconnection pattern is formed on the dielectric first by photolithography (Figure 1.3 (b)). Following barrier/seed layer deposition, the interconnection regions are filled with Cu. The excess Cu after the filling is then polished through chemical mechanical polishing (CMP) to get highly planar surface. Dual damascene process is the improved damascene process, which forms trenches and vias between interconnection levels at the same time as shown in Figure 1.4. Two layers of dielectric are deposited on the wafer with intervening etch stop layers. After the deposition of masking layer, the layer is opened with the etch stop layer where via is located. The upper dielectric is then etched away until the etch stop layer at the middle is exposed. The second etching with a new masking layer defining the location of trench forms the dual damascene structure. A barrier layer such as Ta/TaN or TiN/Ti is deposited on the structure prior to the seed layer deposition to inhibit the diffusion of Cu into the dielectric. The filling of Cu is then performed after the seed layer deposition. The process is completed with CMP by the removal of the excess Cu. The process can be repeated to build up multilevel metal lines. The introduction of the damascene process to the Cu metallization realized the highly planar multilevel metallization.

1.1.2. Cu deposition

One of the most important procedures in the damascene process is the Cu filling of trenches and vias without defect. Defects such as void or seam in the feature after the filling bring out the increase in the resistance of the metal line as well as the probability of electrical disconnection by the electromigration. Therefore, the bottom-up filling is required, which fills Cu from the bottom of the trenches and vias. There are four methods for the Cu filling, physical vapor deposition (PVD), chemical vapor deposition (CVD), electrodeposition (ED), and electroless deposition (ELD).

PVD is one of vacuum deposition methods to deposit metal films by the condensation of a vaporized form of the film material onto substrate surface.[11] The target material is generally vaporized by thermal heating, electron beam, plasma, etc. in vacuum. As the film is formed in the highly-clean vacuum, the physical properties of the film, such as the resistivity and roughness, are relatively better than those of films formed by other deposition methods. The PVD is widely used in the Al interconnection. However, the poor step coverage of the film arising from its anisotropic nature of PVD causes hardship for the application of the process to the Cu filling of the damascene structure with high aspect ratio.[12] PVD is used for the formation of Cu seed layer instead, which is essential for Cu ED. (Figure 1.5)

CVD is also a well-known vacuum deposition method that volatile organic-metal precursors react or decompose on surface, to form a film.[13] The deposition shows excellent step coverage and is capable of the Cu filling of damascene structure. It was reported that the use of iodine

during the deposition could achieve the bottom-up filling by accelerating the deposition rate at the bottom of the feature.[14,15] However, the resistivity of the film is high because the large amount of carbon is incorporated into the film. Furthermore, the precursors are toxic, leading to environmental problems. Atomic layer deposition (ALD) is also one of CVD methods, which controls the film thickness in atomic layer scale. In ALD, the precursors are separated during the deposition reaction by N_2 or Ar purging to prevent parasitic deposition. Therefore, repeating the precursor pulse and purge gas pulse abled the atomic layer control. The amount of the deposit is constant in each reaction cycle.

ED and ELD have been generally used in the metallization of printed circuit boards. Both two deposition methods are wet processes and attract a lot of attention in the metallization of semiconductor as the damascene process is introduced.

ED is the deposition method reducing metal ions to a metal film by supplying electrons to the substrate in a solution.[16] The electrodeposited film shows good step coverage and superior film properties. The low process cost and temperature are also advantages of ED. Furthermore, the bottom-up filling can be achieved by the addition of several organic additives to the ED bath.[17] Organic additives are classified into three main categories: suppressor, accelerator, and leveler. Suppressors are additives retarding the deposition by the adsorption, while accelerators promote the deposition by the replacement of adsorbed suppressors. Levelers are used for the minimization of the height difference in the film. The mechanism of the conventional bottom-up filling through ED is generally explained by curvature enhanced accelerator coverage (CEAC)

model, which deals with the competitive adsorption between accelerators and suppressors during the deposition.[18,19,20] Nowadays, Cu ED is widely used for the metallization of semiconductors. ED requires the Cu seed layer which is the current path because the direct deposition on diffusion barriers such as Ta/TaN is not facile due to its high resistivity.[21,22] The seed layer is normally deposited by PVD as explained above.

Different with ED, ELD reduced metal ions to a metal film with the aid of a chemical reducing agent instead of the external electrical power.[23] Therefore, it is available not only on conductive materials but also on insulators including diffusion barriers if catalyzing process for ELD is performed on the surface. The step coverage of the electroless film is known to be good, and the bottom-up filling can be also achieved by ELD. Moreover, as the deposition can be performed by simple immersion in the ELD bath, it is not required to set up special equipment for the process, resulting in cost reduction. Despite of those advantages, ELD have not been applied to the metallization of semiconductor process because of its low throughput and bath instability. However, as the size of metal line decreases, ELD is re-considered as one of metallization methods in the next generation.

1.1.3. Issues in present metallization process and Cu ELD

The introduction of the Cu damascene process was innovative and brought considerable technical advances in the semiconductor fabrication for a decade. Recently, several challenging

issues arise in the metallization process as the scaling-up of integration continues.

The formation of Cu seed layer has been universally carried out by PVD and it achieves good film properties with good adhesion to diffusion barriers. However, as the size of metal line has dwindled, depositing the thin layer uniformly throughout trenches and vias has become difficult due to the inherent directionality of PVD.[24] The problem then becomes a great obstacle for the PVD process to deposit the uniform thin film over trenches and vias shrinking to sub-tens of nanometer size as shown in Figure 1.6. The poor step coverage thus introduces a lot of defects in the Cu seed layer, leading to the poor reliability of Cu filling. Especially, the PVD seed layer on the side-wall of the narrow features is vulnerable, inducing many defects after Cu ED.[25,26] PVD has been continuously improved to compensate the drawback in various ways, such as a collimated PVD, oblique angled PVD, or ionized PVD.[27,28,29] However, the problem is not solved completely, and the poor step coverage of PVD is still a big issue in the seed layer formation. To overcome the problem, alternative seed layer formation methods have been focused. CVD and ALD are able to form a thinner and more conformal Cu film than PVD, but the resistivity of the film is still too high to use the film as Cu seed layer.[30,31] Another method is Cu ELD. The Cu ELD has been widely investigated as one of metallization methods in semiconductor process for a decade. As explained above, the deposition does not require an external electrical energy, therefore, it is considered to be applicable to the direct formation of Cu film on highly-resistive diffusion barriers. The formation of electroless Cu seed layer, as one of alternatives, was investigated by many researchers, and it was confirmed that the electroless

seed layer was more conformal than the PVD seed layer.[32,33,34] The Cu ELD is also considered as a bridging technique until the seed layer formation overcomes the non-uniformity problem. The so-called 'electroless seed layer repairing' reinforces the non-continuous PVD seed layer on trenches and vias by film thickening.[35,36]

Same as the Cu seed layer, the intrinsic directionality of PVD also makes it difficult to deposit diffusion barriers on narrow trenches. PVD Ta/TaN is known to be an excellent diffusion barrier because it effectively blocks the diffusion of Cu into Si substrate, and it is widely used in the metallization. However, as the required thickness of the barrier is reduced from 2.6 nm in 2012 to 1.9 nm in 2015 (Figure 1.2), it is difficult to form such a thin film on the narrow features using the advanced PVD. Therefore, other Ta-based diffusion barriers are also considered. The ternary alloy diffusion barriers such as TaSiN, TiSiN, and TaN are known to be deposited by ALD, thus, those barriers can be uniformly deposited on narrow trenches and vias.[37,38] However, they are not ultimate solutions because the next step of the damascene process, the deposition of Cu seed layer, is still in a trouble. Researchers have then proposed several methods as alternatives for the formation of both diffusion barrier and Cu seed layer. Adopting new barrier materials such as Ru and Co, which act as both a diffusion barrier and current path for direct Cu ED, is one of them. The Ru and Co can be deposited by ALD, and have low surface energy to Cu, which allows the direct Cu ED without a separate Cu seed layer.[39,40,41] It was reported that Ru alone was not enough to prevent the Cu diffusion into Si substrate when its film thickness was thinner than 5 nm, and Co caused the deterioration of Cu

film properties through its acidic dissolution and displacement reaction with Cu ions in the electrolyte during Cu ED.[42,43,44] Therefore, the deposition of Ru-alloy and Co-alloy is widely investigated and it is expected that those films can be used as the next generation barriers.[45,46,47] On those barriers, the Cu ELD is also highlighted as one of Cu metallization methods because Ru and Co themselves act as a catalyst for Cu ELD.[48,49] There is no need for catalyzing process prior to the Cu ELD, simplifying the deposition process compared to Cu ELD on a conventional Ta/TaN diffusion barrier.

The filling of trenches and vias can be also achieved by Cu ELD, which shows the possibility that the Cu metallization is accomplished by a single Cu ELD process without seed layer formation. Until now, Cu ELD is rarely used as the metallization method for the semiconductor fabrication because of its low deposition rate compared to Cu ED. However, as the sizes of trenches and vias become small, the low deposition rate of Cu ELD is no longer a big problem to overcome. The size shrinking of semiconductor devices opens up the possibility of the application of Cu ELD to the Cu damascene process.

Table 1. 1. Properties of Interconnection Materials[6]

Properties	Cu	Ag	Al
Resistivity (μΩcm)	1.67	1.59	2.66
Diffusion coefficient in Si (cm^2/s)	0.78	0.67	1.71
Activation energy in Si (eV)	2.19	1.97	1.48
Melting point (℃)	1085	962	660

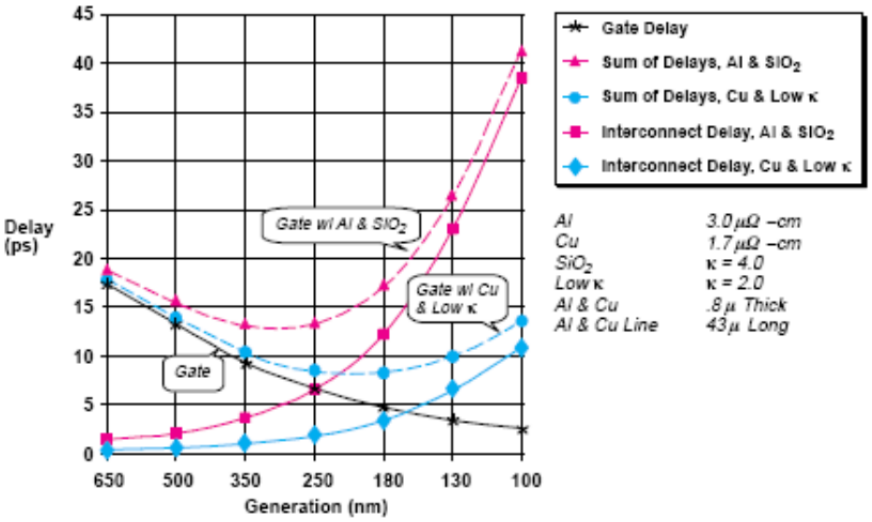

Figure 1. 1. Calculated gate and interconnect delay according to technology generation.[4]

Year of Production	*2011*	*2012*	*2013*	*2014*	*2015*	*2016*	*2017*
DRAM ½ Pitch (nm) (contacted)	*40.09*	*35.72*	*31.82*	*28.35*	*25.26*	*22.50*	*20.05*
Number of metal levels (includes ground planes and passive devices)	*12*	*12*	*13*	*13*	*13*	*13*	*14*
Total interconnect length (m/cm^2) – Metal 1 and five intermediate levels, active wiring only [1]	2,632	3,125	3,704	4,167	4,762	5,291	5,917
J_{max} (MA/cm^2) – intermediate wire (at 105°C) [7]	1.16	1.32	1.50	1.68	1.79	1.81	2.01
Interlevel metal insulator – effective dielectric constant (κ)	2.82-3.16	2.82-3.16	2.55-3	2.55-3	2.55-3	2.1-2.78	2.1-2.78
Interlevel metal insulator – average dielectric constant (κ)	2.99	2.99	2.78	2.78	2.78	2.44	2.44
Copper diffusion barrier and etch stop – bulk dielectric constant (κ)	3.5-4.0	3.5-4.0	3.0-3.5	3.0-3.5	3.0-3.5	2.6-3.0	2.6-3.0
Metal 1 wiring pitch (nm)	76	64	54	48	42	38	34
Metal 1 A/R (for Cu)	1.80	1.80	1.90	1.90	1.90	2.00	2.00
Barrier/cladding thickness (for Cu Metal 1 wiring) (nm) [3]	2.9	2.6	2.4	2.1	1.9	1.7	1.5
Conductor effective resistivity (μΩ- cm) Cu Metal 1 wiring including effect of width-dependent scattering and a conformal barrier	4.48	5.00	5.63	6.00	6.61	6.96	7.46
Interconnect RC delay (ps) for 1 mm Cu Metal 1 wire, assumes width-dependent scattering and a conformal barrier of thickness specified	3,429	5,373	7,813	10,539	15,164	17,216	23,050

Figure 1. 2. Technological requirements in Cu interconnection.[5]

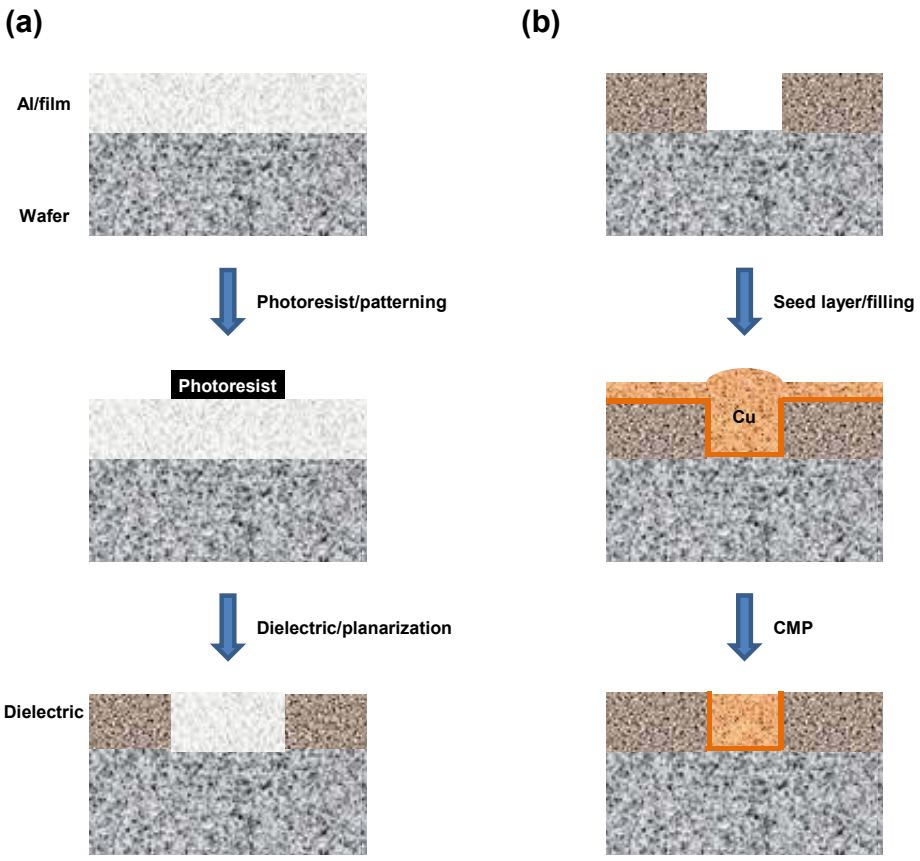

Figure 1. 3. Schemes of (a) subtractive etching and (b) single damascene process.

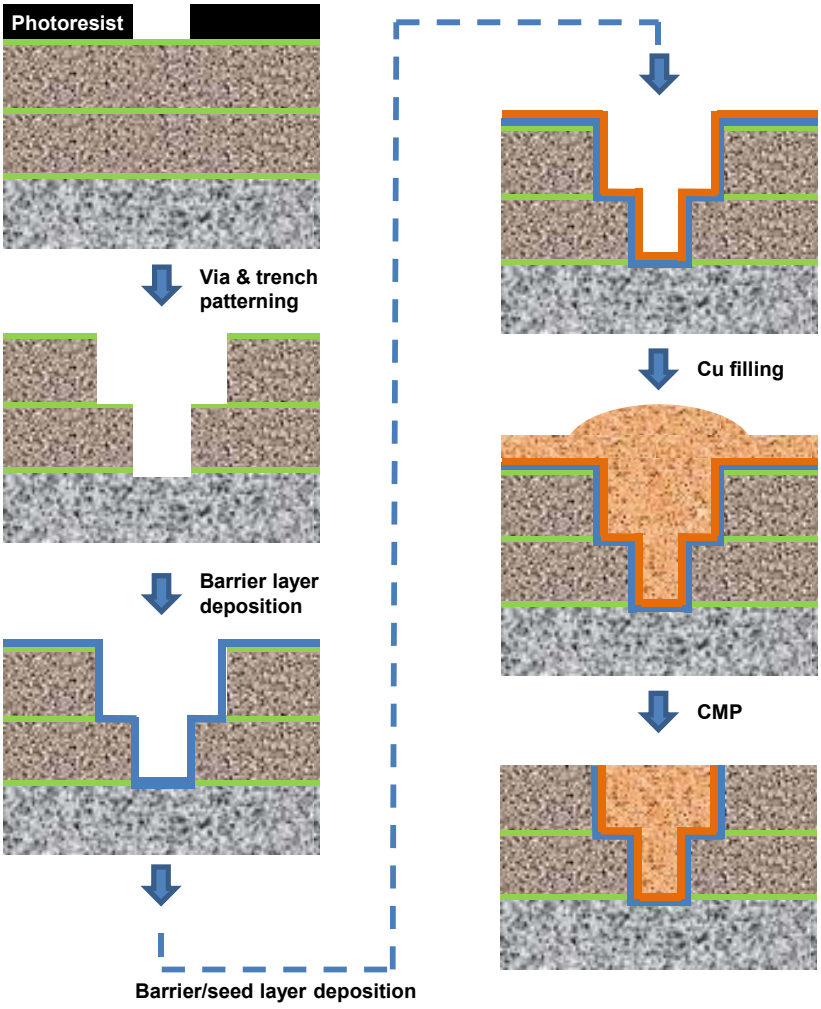

Figure 1. 4. Scheme of dual damascene process.

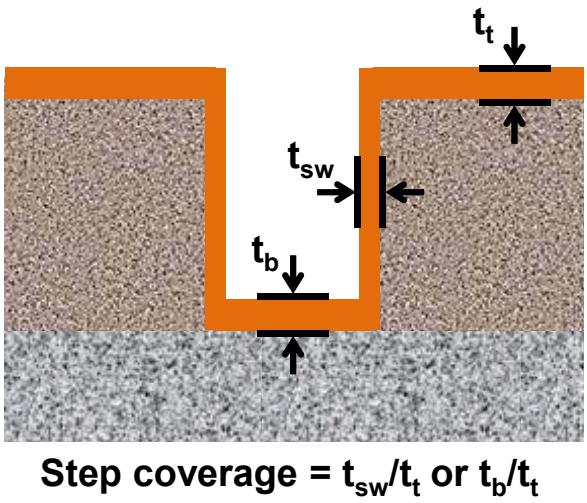

Figure 1. 5. Step coverage of Cu seed layer on trench.

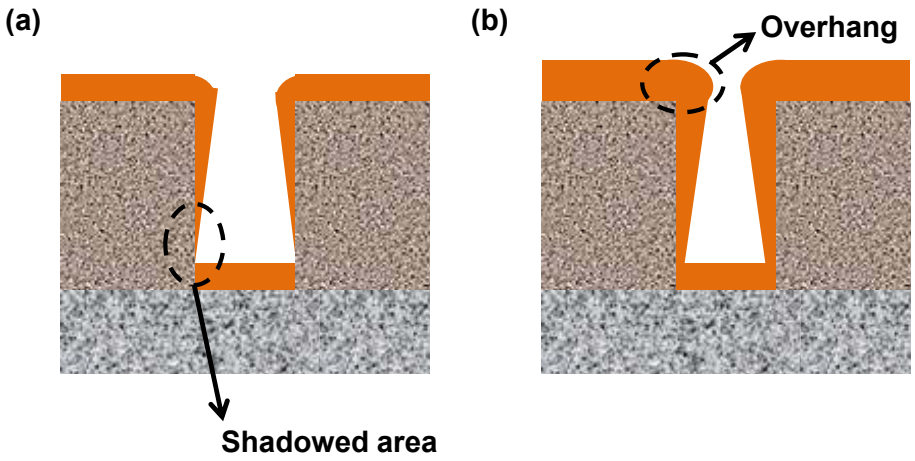

Figure 1. 6. Uniformity problem in the Cu seed layer deposited by PVD on trench, (a) less-deposited and (b) over-deposited.

1.2. ELD

1.2.1. Basics of ELD

ELD is a deposition method which is distinctly differentiated from ED using the external power supply. In ELD, metal ions in a solution are reduced by the oxidation of a reducing agent on surface, forming a metal film.[50] As electrons which reduce metal ions are supplied by the oxidation reaction of reducing agents, there is no need for the external source of electric current. Both two electrochemical reactions, the reduction of metal ions and the oxidation of reducing agents, occur simultaneously at the same electrode, at the same electrode-solution interface as shown in Figure 1.7.

$$M^{a+}_{solution} + ae^- \rightarrow M^0_{surface} \quad [1.1]$$

$$Red_{solution} \rightarrow Ox_{solution} + be^- \quad [1.2]$$

The overall reaction of ELD is,

$$M^{a+}_{solution} + (a/b)Red_{solution} \rightarrow M^0_{surface} + (a/b)Ox_{solution} \quad [1.3]$$

where Ox is the oxidation product of the reducing agent Red, and M^{a+} and M^0 are a metal ion and deposited metal on surface, respectively. Thus, cathodic and anodic sites exist on the same

electrode. Electrons, which are produced by the oxidation of reducing agents, flow between these sites during the deposition.

Theoretically, ELD is explained by the mixed potential theory derived from a concept for the interpretation of corrosion phenomena.[51,52] Assuming that the cathodic reaction [1.1] and anodic reaction [1.2] occur independently, the two partial reactions can be plotted in a current-potential (i-E) graph as in Figure 1.8. The equilibrium potential of the oxidation of a reducing agent is more negative than that of the reduction of a metal ion, so that the reducing agent can be oxidized to provide electrons for metal ions. The overall reaction of ELD is interpreted by superimposing the partial electrochemical reactions. According to the overall reaction [1.3], there is no external current flow out of the electrode because electrons produced by the reaction [1.2] are totally consumed by the reduction of metal ions. Therefore, the current flow between reactions [1.1] and [1.2] should be same when ELD takes place. The potential where the anodic and cathodic currents are same is regarded as the electrode potential of ELD and called as "mixed potential". Although it is reported that ELD is more complicated than represented by the mixed potential theory due to the interdependence of the partial reactions and side-reactions of ELD, it is still useful to understand the characteristics of ELD process.

Unlike the galvanic displacement reaction which reduces target metal ions onto other metallic surfaces by using the difference in the standard reduction potentials of the two metals, ELD uses the oxidation of a reducing agent on surface. Therefore, the chemical reaction should proceed on catalytic surfaces. ELD is an autocatalytic reaction that the deposited metal itself acts as a

catalyst for the oxidation of a reducing agent, leading to continuous film growth during the deposition. It limits materials which can be deposited by ELD. The survey revealed that single metals such as Co, Ni, Cu, Ag, Au, etc. are plateable by autocatalytic means.[53] (Figure 1.9) In some cases, metals which have no autocatalytic character are also co-deposited with other autocatalytic metals: NiP, NiWP, NiB, NiWB, CoP, CoWP, CoB, CoWB, etc.

For this reason, noncatalytic surfaces (e.g., insulators, noncatalytic metals) should be made catalytic for ELD prior to the deposition. The catalyzing process is generally termed as surface activation that generates catalytic nuclei on the noncatalytic surface. To date, several surface activation methods have been reported: one-step activation, two-step activation, and the deposition of nanocatalysts.[54,55,56] Pd, Rh, Ag, etc. have been widely used as such a catalyst. Figure 1.10 shows the schematic diagram of the film growth on catalytic nuclei. As each catalytic particle acts as a nucleus for ELD, the deposited metal grows in three dimensions and covers the particle preferentially at the initial stage. This growth mode continues until the metal clusters coalesce and thus cover the entire surface, followed by subsequent two-dimensional growth normal to the surface.[57,58] The time required to reach the two-dimensional growth mode from the start of the three-dimensional growth is determined by the density and average size of particles.[59] (See appendix.)

The general ELD bath has 4 components: the source of metal ions, reducing agent, complexing agent, and pH adjuster. Metal ions and reducing agents are main chemicals which participated in ELD process as above. The role of complexing agent in the bath is to stabilize

metal ions by forming metal ion-complexes. The ELD bath is generally alkaline because the most of reducing agents require hydroxide ions during the oxidation process. Thus, forming metal ion-complexes is essential to prevent the formation of metal-hydroxide species in the bath. It is also known that deposition rate is affected by the types of complexing agents because the complex-stability constant and the specific adsorption kinetics of the molecule are directly related with the deposition.[60] In addition, several organic additives are added to the bath for the improvement of the properties of the deposited film, the stabilization of the bath, and the elimination of side-reactions.

1.2.2. Mechanism of Cu ELD

The bath composition for Cu ELD is strongly dependent on the type of reducing agent. The typical reducing agents for Cu ELD are formaldehyde (HCHO) and glyoxylic acid, which have an aldehyde group in their molecular structure. A typical Cu ELD bath contains divalent Cu ions, ethylenediaminetetraacetic acid (EDTA) as a complexing agent, and HCHO as a reducing agent.[61] Sodium hydroxide, potassium hydroxide, or tetramethylammonium hydroxide is used as a pH adjuster. The overall reaction of Cu ELD on Cu surface is shown below when HCHO and EDTA are used as a reducing agent and complexing agent, respectively.[62]

$$[CuEDTA]^{2-} + 2HCHO + 4OH^- \rightarrow Cu + 2HCOO^- + 2H_2O + H_2 + EDTA^{4-} \quad [1.4]$$

The reduction of Cu-EDTA complexes proceeds by accepting electrons one by one on the surface.

$$CuEDTA^{2-} + e^- \rightarrow CuEDTA^{3-} \quad [1.5]$$

$$CuEDTA^{3-} + e^- \rightarrow CuEDTA^{4-} \quad [1.6]$$

$$CuEDTA^{4-} \rightarrow Cu^0 + EDTA^{4-} \quad [1.7]$$

However, the oxidation mechanism of HCHO is more complicated than that of the reduction. The majority of HCHO molecules are hydrolyzed in the alkaline solution, finally forming methylene glycol anions ($H_2C(OH)O^-$) as follows:

$$HCHO + H_2O \rightarrow H_2C(OH)_2 \quad [1.8]$$

$$H_2C(OH)_2 + OH^- \rightarrow H_2C(OH)O^- + H_2O \quad [1.9]$$

The methylene glycol anion adsorbs on the surface with dissociative adsorption, involving the breakage in the C-H bond. The electrochemical oxidation then occurs with hydrogen evolution.[63]

$$H_2C(OH)O^- + OH^- \rightarrow HCOO^- + H_2O + 1/2H_2 + e^- \quad [1.10]$$

The hydrogen evolution during the oxidation reaction has negative influence on the ductility, adhesion, and surface roughness of the deposited film.[64] However, it is reported that the HCHO oxidation on catalytic metals, which have the negative Gibbs free energy of hydrogen adsorption (e.g., Pt, Pd, Rh, etc.), does not accompany the hydrogen evolution.[65]

1.2.3. Organic additives in Cu ELD bath

Organic additives in Cu ELD bath play important roles in the above processes. The additives adsorb on surface during the deposition, and change deposition conditions in various ways. They can be classified into three categories according to its effect on the deposition, stabilizers, accelerators, and suppressors. Stabilizers retard the self-decomposition of ELD solution by the complexation with unstable Cu ions. 2,2'-dipyridyl and thiourea are famous as effective stabilizers.[66,67,68] Accelerators, which increase the deposition rate, are reported as guanidine and 8-hydroxy-7-iodo-5-quinoline sulfonic acid (HIQSA).[69] On the contrary, polyethylene glycol (PEG) and its derivatives are commonly used as suppressors. It is known that suppressors block active sites by the adsorption and suppress the deposition.[70] Other additives such as bis(3-sulfopropyl) disulfide (SPS), 3-N,N-dimethylaminodithiocarbamoyl-1-propanesulfonic acid (DPS), 2-mercaptobenzothiazole, benzotri-azole, etc. can act as both accelerator and suppressor, depending on their concentration.[71] The suitable combination of those additives can change the

film properties and deposit profile as one's purpose.

One of main interests in Cu damascene process is the Cu filling of trenches and vias, and it can be also achieved by ELD using the combination of organic additives. The electroless filling has been extensively studied in a number of years. The filling mechanism of Cu ELD is slightly different with CEAC model of Cu ED. There are three filling mechanisms suggested in Cu ELD as shown in Figure 1.11. One is the formation of the concentration gradient of a suppressor inside of trenches for the filling, resulting in 'V'-shape of filling profile. (Figure 1.11 (a)) The concentration of the suppressor at the top of the trench is generally higher than that at the bottom because the additive is diffused into the trench from the bulk and consumed continuously by the incorporation into the film during the deposition. Therefore, the deposition rate at the top surface would be much lower than that at the bottom, resulting in the bottom-up filling. S. Shingubara et al. and T. Osaka et al. achieved the electroless filling by using the method: SPS and PEG as a suppressor, respectively.[72,73] Another method is forming the concentration gradient of the additive which act as both the accelerator at low concentration and suppressor at high concentration. The deposition rate at the bottom, where the concentration of the additive is low, is then accelerated whereas the deposition rate at the top is strongly inhibited. In this case, bumps are formed on the top of the trench due to the acceleration effect. J. J. Kim et al. found that SPS, DPS, and 2-mercapto-5-benzimidazolesulfonic acid (MBIS) accelerated the deposition rate at low concentration and gained the bottom-up filling profile with bump formation.[74,75,76] The other method is using both the accelerator and suppressor to maximize the

suppression effect on the top of the trench. Hasegawa et al. and Yang et al. used the combination of both the accelerator and suppressor for the filling.[77,78] Accelerators were HIQSA and SPS, and the suppressor was PEG.

Figure 1.12 shows molecular structures of 2,2'-dipyridyl, PEG, DPS, and SPS. The direct relationship between the molecular structure and its effect on Cu ELD is not well-known. Generally, the heteroaromatic compounds with nitrogen atoms are used as stabilizers, such as 2,2'-dipyridyl. It is not clear why those kinds of molecules are effective on the stabilization of ELD bath. However, it is suspected that their strong adsorption on surface and complexation with metal ions through the π-conjugated ring structure are main causes of the effective stabilization.[68] PEG is the polymer having ether groups in its structure. Oxygen atoms with non-bonding electrons are assumed to participate in the adsorption. In Cu ELD, PEG is added to ELD solution as both a surfactant and suppressor. SPS and DPS are famous accelerators in Cu ED, which contain sulfur atoms. It is reported that they accelerate the reduction process of "$Cu^{2+} + e^- \rightarrow Cu^+$" which is the rate determining step of the total Cu ion reduction. The acceleration in the deposition rate is also observed in Cu ELD, however, the mechanism has not been revealed in detail.[74, 75]

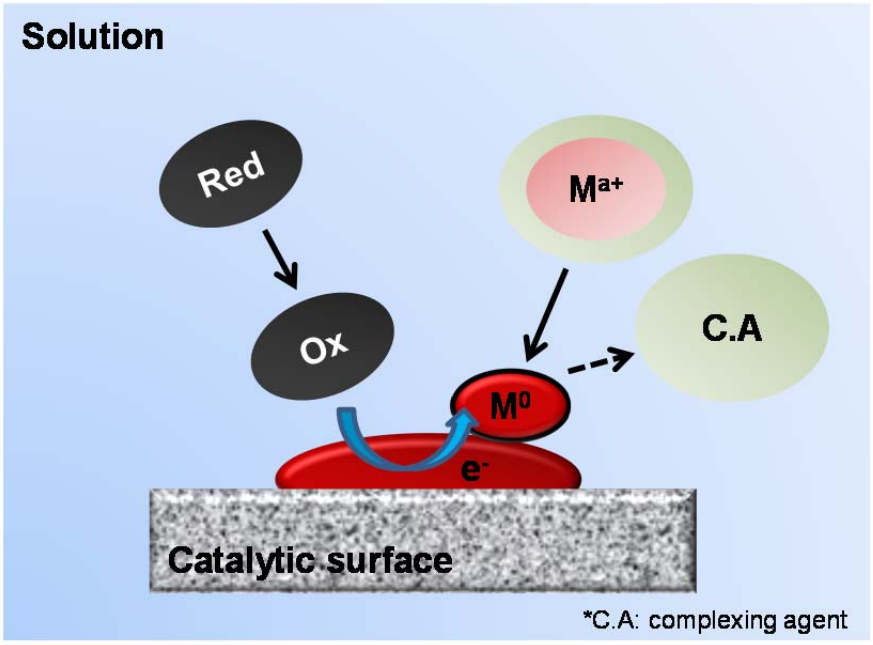

Figure 1. 7. Schematic diagram of ELD.

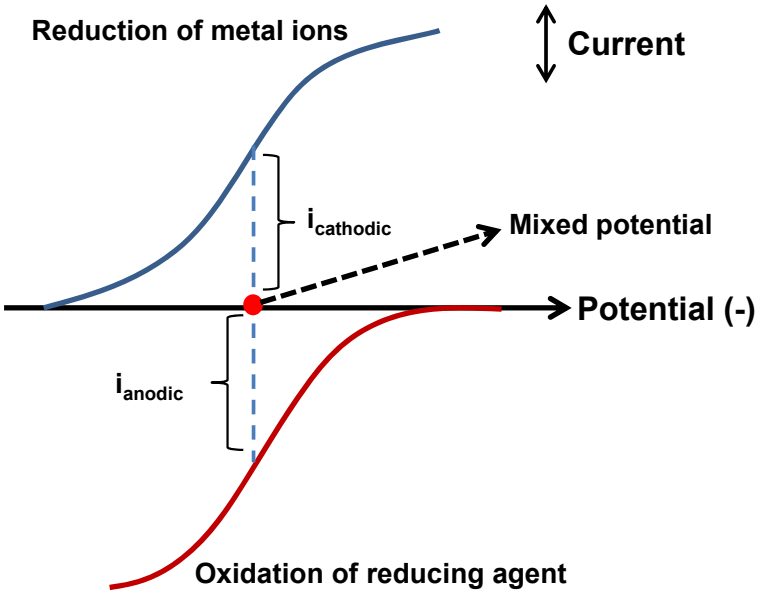

Figure 1. 8. Schematic diagram of the mixed potential electrode.

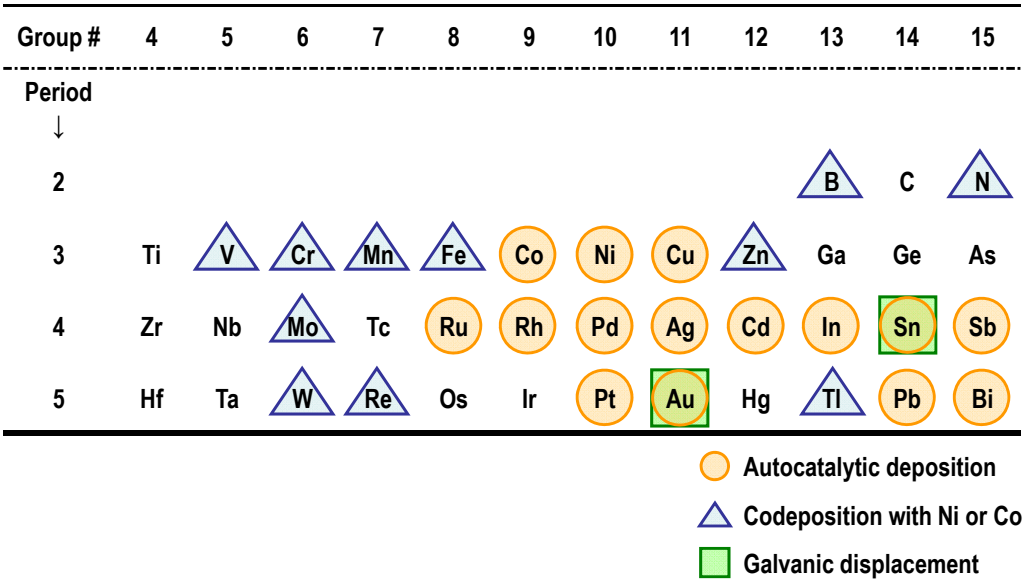

Figure 1. 9. Periodic table of elements which can be deposited by ELD.

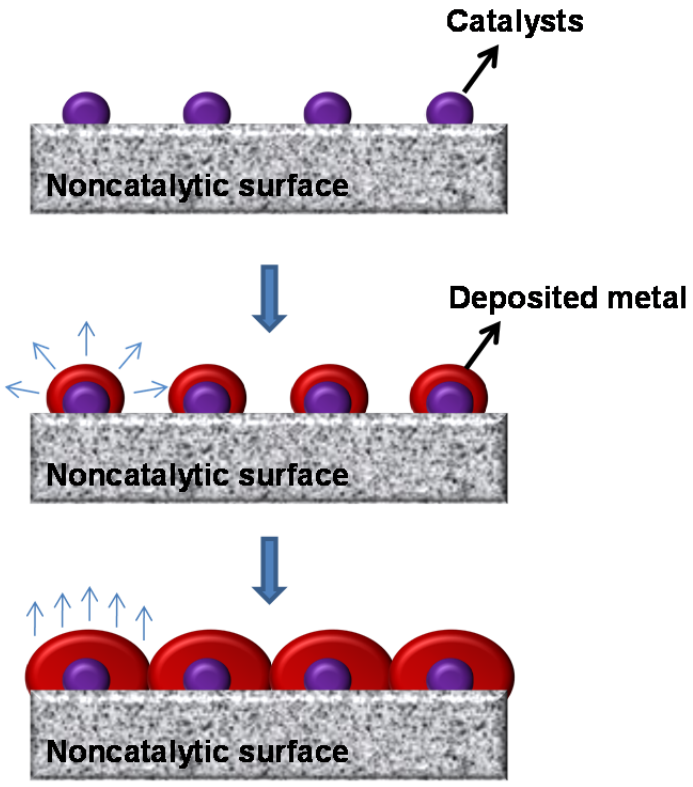

Figure 1. 10. Schematic diagram of electroless film growth on noncatalytic surface.

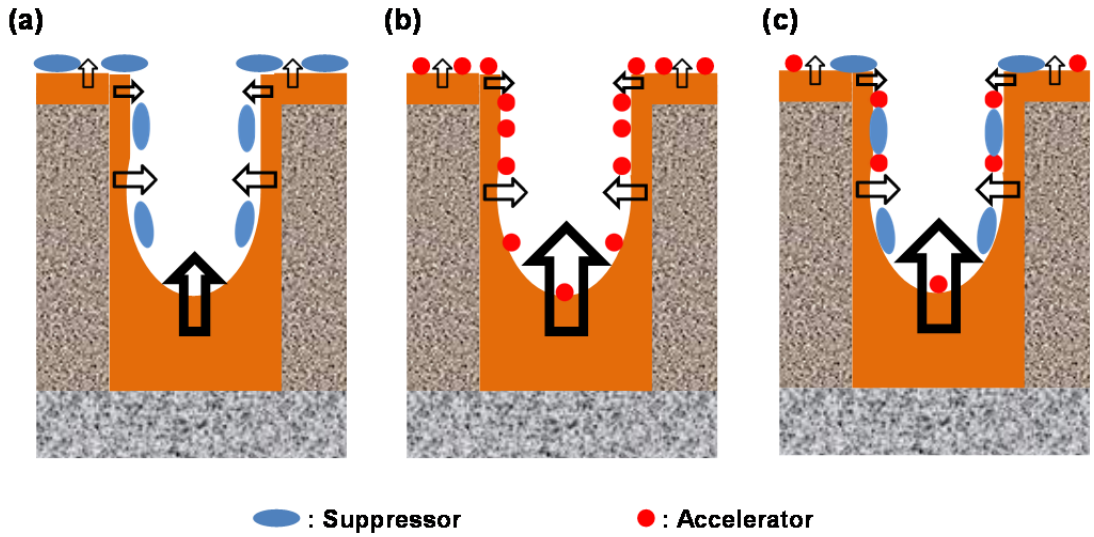

Figure 1. 11. Schematic diagram of the electroless filling mechanism, (a) the suppressor only, (b) the additive which acts as both the accelerator and suppressor, and (c) the combination of the accelerator and suppressor.

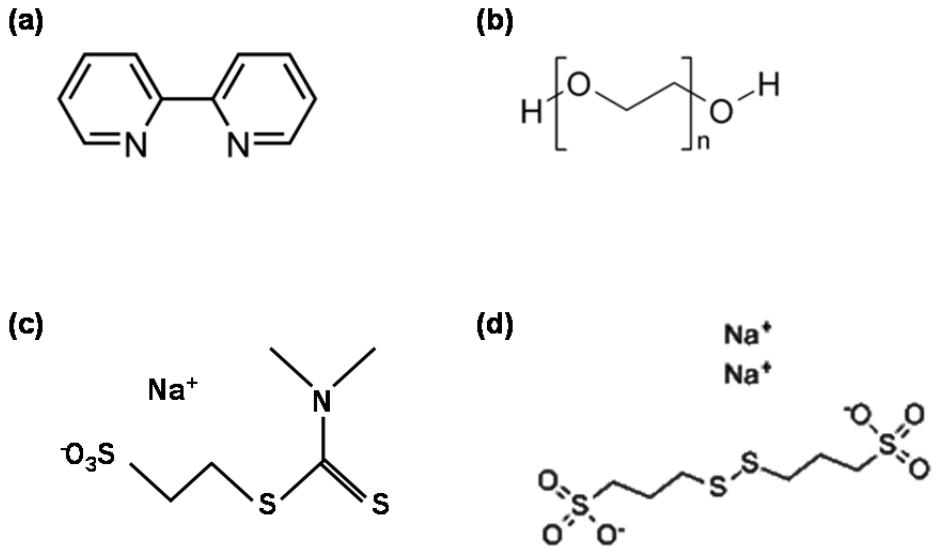

Figure 1. 12. The molecular structures of additives, (a) 2'2-dipyridyl, (b) PEG, (c) DPS, and (d) SPS.

1.3. Observation of Cu ELD

1.3.1. Analysis tools for Cu ELD

The mechanism of Cu ELD has been extensively studied by voltammetric measurements such as cyclic voltammetry (CV) and linear sweep voltammetry (LSV). Based on the mixed potential theory, the reduction of Cu ions and the oxidation of reducing agents are independent each other. Therefore, many researchers studied both partial reactions separately. L. D. Burke et al. investigated the oxidation mechanism of glyoxylate on Cu using CV, and interpreted it in terms of incipient hydrous oxide/adatom mediator (IHOAM) model of electrocatalysis.[79] T. M. Tam developed the *in-situ* measurement of the concentration of methylene glycol anions in ELD bath by calculating charges formed during the electrochemical oxidation.[80] P. Bindra et al. examined the mixed potential theory by comparing with real ELD system, finding the interdependence of the partial reactions.[81] Some studies also utilized CV and LSV to observe the additive effect on the reduction of Cu ions and oxidation of a reducing agent. M. Paunovic et al. tested the effects of additives on the reduction of Cu ions using CV in Cu ELD bath, and P. A. Kohl et al. investigated the effect of 2,2'-dipyridyl concentration on the oxidation of a reducing agent using LSV.[82,83]

Some researchers introduced additional electrochemical tools for the study. A. Vaškelis et al. reported that the rupture of C-H bond of HCHO was a rate-determining step in ELD using differential electrochemical mass spectrometry with CV.[84] O. R. Melroy et al. used quartz

crystal microbalance (QCM) to separate the real deposition current from the measured current of LSV in ELD solution, finding that HCHO catalyzed Cu ion reduction.[85]

However, it is a little ambiguous to conclude that CV and LSV studies in half-cell solution or full ELD solution represent the real ELD process perfectly because considerable overpotential was applied to the electrode. Therefore, the mechanism was also investigated by non-electrochemical tools. J. J. Kim et al. examined the reactivity of Cu ELD solution according to the types of complexing agents by using laser transmittance, and C.-H. Chung et al. used Fourier transform infrared spectrometry (FT-IR) to verify the reaction mechanism of Cu ELD.[86,87]

The observation methods frequently used are *ex-situ* investigations, such as the measurement of the deposition rate and the observation of surface morphology because of their easy accessibility.[88] The *ex-situ* investigation provides researchers with various kinds of practical information in the real deposition. However, it is not sufficient to understand the adsorption behavior of reactants and additives because their adsorption is time-dependent.

1.3.2. Real-time observation of Cu ELD by OCP measurement with QCM

In this study, the mechanism of Cu ELD was investigated by measuring the open-circuit potential (OCP) and mass change of Cu electrode. OCP is the potential of working electrode relative to reference electrode when no potential or current is applied. As OCP measurement

used the minimum overpotential for the minimization of current flow, there is low possibility that the electrode is affected by the applied overpotential. Furthermore, it is advantageous to check the state of the electrode because OCP is sensitive to electrode conditions, such as the chemical state of the electrode and the adsorption of chemicals.[89] QCM was also introduced to measure kinetic changes on the electrode during the OCP measurement. Like in general electrochemical measurement, the OCP and mass change can be regarded as the electrode potential and current, respectively. The combination of two methods realized the real-time observation of Cu ELD.

The OCP measurement with QCM during Cu ELD makes it possible to observe the adsorption behavior of reagents and additives on surface *in-situ*. Even though the reaction mechanism of Cu ELD was extensively investigated by many researchers, the adsorption of each constituent of Cu ELD bath and its effect on Cu surface were not studied in detail because it was not easy to observe the phenomena using conventional *ex-situ* analysis tools. Therefore, the adsorption of basic components of Cu ELD bath and their effects were first investigated by using the method for the complete understanding of the overall adsorption process during Cu ELD (chapter III). Based on this research, the adsorption behaviors of additives, which were essential for the filling of damascene structure, was then studied (chapter IV). The effect of additive has been also generally investigated *ex-situ* by observing the change in the deposition rate and surface morphology according to the additive concentration. The *ex-situ* investigation provides researchers with various kinds of practical information in the real deposition. However,

it is not sufficient to understand the adsorption behavior of additive because the adsorption is dynamic and competitive with other reagents. We investigated the adsorption behaviors of PEG, 2,2'-dipyridyl and DPS and their effects on the deposition in real-time and applied those additives to the filling of sub-60 nm trenches. Finally, the bottom-up filling of sub-60 nm trenches was systemically designed based on the investigation.

Chapter II. Experimental

2.1. Electrochemical analysis

2.1.1. OCP measurement with QCM

The OCP measurement was performed using a Potentiostat 263A (EG&G) and QCM (QCA917, EG&G) with a 2-electrode system as shown in Figure 2.1. The working electrode was a Cu-coated 9 MHz AT-cut quartz crystal (QA-A9M-Cu(M), mirror finish, Seiko EG&G model) with an exposed area of 0.196 cm^2. The Cu was deposited by PVD. Ag/AgCl electrode (KCl saturated, BAS Inc.) was used as the reference electrode.

Prior to all experiments, the working electrode was cathodically polarized at room temperature to remove native Cu oxides.[90] During the cathodic polarization, 5 mA/cm^2 of cathodic current was applied to the working electrode for 5 min in 0.1 M H_2SO_4 electrolyte. The electrode was then immersed in various test solutions consisting of basic chemicals for Cu ELD bath. The full Cu ELD solution was composed of 0.03 M $CuSO_4 \cdot 5H_2O$, 0.05 M EDTA, and 0.10 M p-HCHO (para-formaldehyde). In the investigation of additive effect, the electrode was kept for 200 s in the full Cu ELD solution until the deposition process became stabilized. After the stabilization, additives were injected to the bath. Additives were PEG, 2,2'-dipyridyl and DPS. The ELD solution was mildly stirred during the experiment to facilitate the bulk diffusion of additives after the injection. The pH of all solutions was adjusted to 12.8 by adding KOH and

temperature was kept at 70℃ using a thermostat.

2.1.2. Coulometric reduction method

The chemical state of Cu surface was examined by coulometric reduction method (CRM). CRM was performed with a 3-electrode system. Pt wire and Ag/AgCl electrode (KCl saturated, BAS Inc.) were used as the counter electrode and reference electrode, respectively. Cu oxides were reduced in a 0.1 M KCl solution with a cathodic current of 50 $\mu A/cm^2$ at room temperature during CRM.

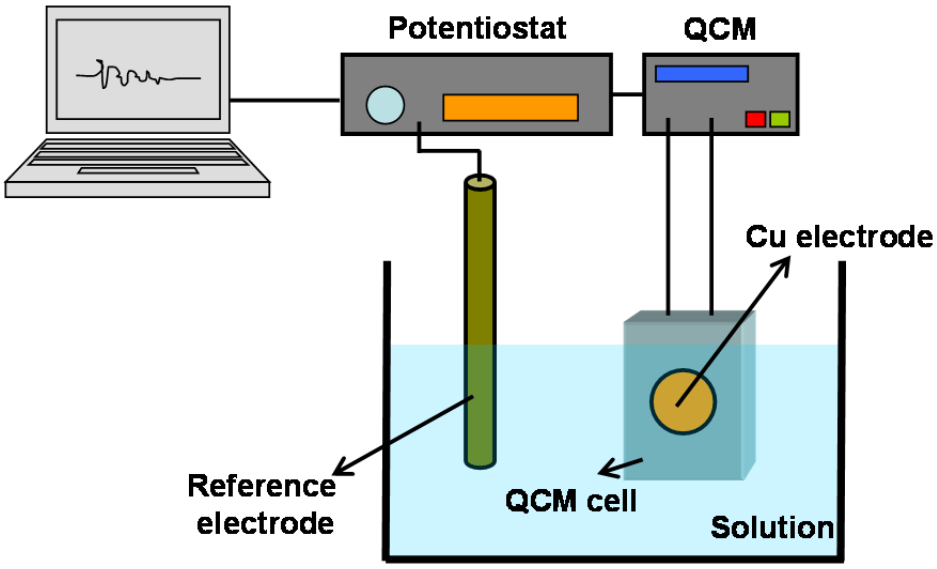

Figure 2. 1. The 2-electrode system for the electrochemical analysis.

2.2. Film analysis

2.2.1. Preparation of Cu ELD films

Simple immersion process without any electrochemical measurement was also performed for the comparison with OCP-QCM results. Cu ELD was performed on a 1.5 cm × 1.5 cm blanket coupon wafer of <PVD Cu (80 nm) / PVD Ta (15 nm) / PVD TaN (15 nm)> structure. The solution composition for the deposition was the same with the full Cu ELD solution used in the electrochemical analysis. The cathodic polarization was also introduced before Cu ELD. Sometimes, the Cu surface was intentionally oxidized to observe the effect of Cu oxides on Cu ELD. Native oxide was grown by leaving the substrate in the atmosphere for 1 day, and chemical oxide was formed by the immersion in 30 vol% H_2O_2 for 30 s to magnifying the oxide effect on ELD. The oxidation was performed at room temperature.

The electroless filling was also performed in sub-60 nm-wide trenches with the aspect ratio over 6 on SiO_2/Si substrates. The barrier layer (Ta/TaN) and Cu seed layer were deposited by PVD. Prior to the filling, the substrate was pretreated with 0.02 M citric acid (pH 4.5 by KOH) solution for 2 min to remove the native Cu oxide instead of the cathodic polarization which resulted in the severe dissolution of Cu at the side-wall of trenches. The pretreated substrate was rinsed in deionized water and immersed into the ELD solution.

2.2.2. Analysis tools

The sheet resistance of Cu film was measured by using a 4-point probe (CMT-SR 1000N, AIT). The surface morphology of the deposited Cu film was observed by means of atomic force microscopy (AFM; AFM5100, Agilent) and field emission scanning electron microscopy (FE-SEM; JSM-6701F, JEOL). The filling profile was also examined by FE-SEM. The sample was broken perpendicularly to the pattern for the observation of the cross-sectional filling feature. The chemical state of Cu surface was examined by X-ray photoelectron spectroscopy (XPS; AXIS-HSi, KRATOS) analysis. In the XPS analysis, as-prepared sample was moved to the XPS chamber immediately after the experiment to prevent air oxidation. The radiation source was Mg Kα from a Mg/Al dual anode at 450 W. The hemispherical energy analyzer was used for the detection of photoelectron energy in the fixed analyzer transmission (FAT) mode with the pass energy of 20 eV, and the energy resolution was 0.1 eV. The take-off angle during the analysis was 45˚.

Chapter III. Investigation of Cu ELD mechanism

3.1. Role of each chemical component in Cu ELD bath

3.1.1. Adsorption of each chemical component and its effect on Cu surface

To verify the role of each chemical component in Cu ELD solution, the electrochemical measurement was separately performed. The OCP and mass change of the electrode during the immersion in KOH, EDTA-KOH, HCHO-EDTA-KOH, and HCHO-KOH solutions are shown in Figure 3.1, respectively. The OCP was maintained around -0.2 V over 1000 s in KOH solution. The electrode potential of -0.2 V for Cu at pH 12.8 corresponds to the Cu oxide region in the Pourbaix diagram.[91] When the metallic Cu is exposed to the alkaline media at its OCP, dissolved oxygen begins to be adsorbed on the surface and reduced by following reaction:

$$O_2 + 4H^+ + 4e^- \rightarrow 2H_2O \quad [3.1]$$

The reduction of dissolved oxygen results in the oxidation of Cu.[92,93] The mass change of the electrode shows the oxidation. The Cu oxidation through the adsorption of dissolved oxygen increased the mass because oxygen atoms were incorporated into the surface, as shown in Figure 3.1 (b) [KOH]. The mass of the electrode was increased with increasing immersion time in the KOH solution. The fast increase rate before 100 s was mainly attributed to the fast

adsorption of dissolved oxygen on the fresh Cu surface, which resulted in the fast oxidation. The oxidation rate then decreased as the diffusion of dissolved oxygen into the film was retarded by the oxide growth.

In the presence of EDTA with KOH, however, the OCP was decreased to ca. -0.5 V, as shown in Figure 3.1 (a) [EDTA-KOH]. The initial mass increase before 100 s in Figure 3.1 (b) [EDTA-KOH], which was also observed by A. Vaškelis et al., was mainly ascribed to the fast oxidation of the Cu surface.[94] The diffusion of dissolved oxygen to the surface was much faster than that of EDTA (D_{O2} = 3.4 x 10^{-5} cm^2/s, D_{EDTA} = 6.0 x 10^{-6} cm^2/s, D: diffusion coefficient at 25℃).[95,96] Therefore, the oxidation rate could be fast in the initial stage. After 100 s, the mass of the electrode was continuously reduced with time. EDTA is known to make a strong complex with Cu ions.[97] That is, the oxides formed in the alkaline media presumably dissolve into complexed forms such as $[CuEDTA]^{2-}$. The formation and dissolution of Cu oxides occurred on the electrode, resulting in the continuous mass decrease. The dissolution rate was found to be 1.4 nm/min which was comparable with 1.1 nm/min, obtained from the immersion process without electrochemical measurements. The dissolution rate during the immersion was calculated by measuring sheet resistance before and after the immersion. The electrochemical behavior of the Cu electrode was also investigated in Cu-EDTA-KOH solution. The added Cu ions had little influence on the dissolution behavior.

The OCP and mass change of the electrode in the presence of HCHO are shown in Figure 3.1 [HCHO-EDTA-KOH]. The majority of HCHO molecules were reported to change their

structure to methylene glycol anion ($H_2C(OH)O^-$) in alkaline media. The anions are adsorbed on the Cu surface and reduce Cu ions by reacting with OH^- as follows:

$$2H_2C(OH)O^- + 2OH^- \rightarrow 2HCOO^- + 2H_2O + H_2 + 2e^- \quad [3.2]$$

The OCP was shifted to a more negative value (ca. -0.9 V) than that of EDTA-KOH, which was attributed to the adsorption of methylene glycol anions on the surface since the adsorbed methylene glycol shifted the OCP in the negative direction by giving electrons to the surface. With the adsorption, the mass increased until 100 s and then remained almost constant. This indicated that the electrode was not dissolved by EDTA in the presence of HCHO. To observe whether EDTA affected the OCP and mass change in the presence of HCHO, a Cu electrode was immersed in HCHO-KOH solution immediately after the cathodic polarization. The OCP and mass change of the electrode followed almost the same trend as those of HCHO-EDTA-KOH solution, as shown in Figure 3.1 [HCHO-KOH]. This demonstrated that the effect of EDTA was negligible on the electrochemical behavior in the presence of HCHO. The adsorption of methylene glycol anions inhibited further Cu oxidation and blocked the dissolution of Cu oxide by EDTA. However, in any combination, the oxidation-induced mass increase before 100 s was observed because of the fast diffusion of dissolved oxygen at the beginning of the immersion.

To investigate the existence of Cu oxide on the electrode, CRM was performed in 0.1 M KCl solution with the cathodic current of 50 $\mu A/cm^2$.[98] Figure 3.2 (a) shows the mass change of the

electrode during coulometric reduction (CR) with respect to the immersion time in EDTA-KOH solution. The mass was decreased as Cu oxide was reduced to Cu. The amount of mass decrease during CR peaked at 100 s, which was the time that the highest mass was recorded in Figure 3.1 (b) [EDTA-KOH]. Then it decreased as the immersion time increased. This trend coincided with the mass change shown in Figure 3.1 (b) [EDTA-KOH]. The oxide still existed on the electrode surface after 400 s of immersion due to the occurrence of two simultaneous reactions: the formation and dissolution of Cu oxide. A small amount of Cu oxide was considered to have continuously formed on the surface when it was being immersed in the EDTA-KOH solution. These observations revealed that EDTA acted as the complexing agent of Cu ions as well as the oxide remover maintaining the electrode surface with low oxygen content. The CR result after the immersion in HCHO-EDTA-KOH solution is also depicted in Figure 3.2 (b). The decrease in mass during CR also exhibited a similar trend to that shown in Figure 3.1 (b) [HCHO-EDTA-KOH]. The amount of mass reduction increased until 100 s and then remained constant at longer immersion times. Although a small amount of oxide must have been formed at the beginning, it was not further formed or removed through the immersion. Both the oxidation and dissolution of Cu oxide were inhibited in the presence of HCHO.

Figure 3.3 shows the potential-time curves of electrodes during CR after the immersion in KOH, EDTA-KOH, and HCHO-EDTA-KOH solutions. The chemical state of Cu oxide was inferred as Cu_2O, since a potential plateau was observed at ca. -0.5 V, which is the typical reduction potential of Cu_2O in 0.1 M KCl solution.[99]

XPS analysis was also performed to verify the chemical state of Cu. XPS analysis of Cu generally measures Cu 2p spectra; however, Auger Cu $L_3M_{4,5}M_{4,5}$ signals were utilized instead in this study to obtain discrete peaks of Cu(0) and Cu(I).[100] Figure 3.4 shows the XPS spectra of Auger Cu $L_3M_{4,5}M_{4,5}$ according to the immersion time. Cu(I) and Cu(0) were detected at 916.8 eV and 918.7, respectively. The deconvolution of the peaks was performed by using XPSPEAK41.[101,102] Figure 3.4 (a) shows the XPS spectra in KOH. The peak intensity related to Cu(I) increased with the immersion time, representing that Cu_2O was continuously formed by the oxidation. In terms of the dependence on the immersion time in EDTA-KOH solution, the peak intensity of Cu(0) was once decreased and increased again after 100 s, as shown in Figure 3.4 (b), which demonstrated that the formation of Cu_2O was faster than the dissolution in the early stage of the immersion. The spectra were nearly identical in HCHO-EDTA-KOH, though a slight decrease in Cu(0) peak intensity was observed after 100 s. (Figure 3.4 (c)) A small amount of Cu_2O remained, whereas the oxidation and dissolution of Cu oxide was inhibited by the adsorption of HCHO. It was not revealed whether Cu_2O was necessary for the adsorption of HCHO. However, a small amount of oxide species existed on the surface, as A. Vaškelis et al. had reported that an unknown oxy-species of Cu formed during Cu ELD.[63] Cu 2p spectra were also measured in all cases. No Cu(II) peak was observed from XPS spectra of Cu 2p, indicating that CuO was rarely formed on the surface.[101]

The thickness of Cu_2O was calculated from XPS spectra in Figure 3.4. The intensity ratio of Cu_2O/Cu was calculated using two characteristic peaks, which were located at 916.8 eV (Cu_2O)

and 918.7 eV (Cu). The following equation was used for the calculation:[100]

$$d = \lambda_{ox} \sin\theta \bullet \ln[((D_M\lambda_M)/(D_{ox}\lambda_{ox})) \bullet (I_{ox}/I_M) + 1] \quad [3.3]$$

where d denotes the oxide thickness, λ is the escape depth of the photoelectrons, θ is the take-off angle, D is the atomic density, and I is the area intensity of peak. The value of each constant was used as follows: λ_{Cu2O} = 2.91 nm, λ_{Cu} = 1.63 nm, D_{Cu2O} = 0.084 mol/cm^3, and D_{Cu} = 0.14 mol/cm^3.[100,102] The calculated thickness was listed in Table 3.1.

The immersion in KOH solution resulted in the continuous oxidation of Cu as in Table 3.1. The existence of EDTA and HCHO in the solution showed different behavior. In the case of the immersion in EDTA-KOH solution, the thickness of Cu_2O was increased until 100 s because the oxide formation was dominant at the initial stage. The thickness started to decrease after 200 s by the dissolution of oxide. At 400 s, even the electrode was etched, the oxide thickness from XPS spectra still showed the existence of Cu_2O, indicating that the small amount of Cu_2O was continuously formed during the dissolution. It was found that the Cu_2O formation was nearly stopped in HCHO-EDTA-KOH solution by the adsorption of methylene glycol anions. The oxide thickness was increased before 100 s, then the thickness became almost constant.

3.1.2. Cu ELD on Cu surface

The OCP and mass change of the electrode were also measured in the full ELD solution as shown in Figure 3.5. The OCP during ELD was fluctuated slightly before 200 s and then it reached constant value at ca. -0.7 V. The initial OCP fluctuation was assumed to be strongly related to the induction period which was frequently observed in general ELD process. The induction period is the time that the reduction of Cu ions and the oxidation of reducing agent become balanced. During this period, the deposition rate increased from 0.19 μg/s (69 nm/min) to 0.43 μg/s (156 nm/min) (Figure 3.5 inset), indicating that the deposition rate was accelerated as the reactions became steady-state.

The increase in the deposition rate during the period was also observed in the immersion experiment. Figure 3.6 shows the change of the deposition rate according to the time. The deposition rate increased from 37 nm/min to 99 nm/min in 200 s, and remained nearly constant. Those values were also comparable to the deposition rate calculated from QCM data. The deposition rate from the mass change was calculated by averaging $d(\Delta m)/dt$ until the fixed ELD times (50 s, 100 s, 200 s, 400 s).

As in Figure 3.7, the OCP during ELD was placed at ca. -0.7 V, which was right between -0.5 V and -0.9 V. These values are the OCPs of half-cell solutions, Cu-EDTA-KOH and HCHO-EDTA-KOH. The addition of HCHO or Cu ions to each half cell solution also moved the electrode potential near to the OCP of Cu ELD. When 10 mM Cu ions, one-third of the Cu ion concentration in the full ELD solution, were injected into HCHO-EDTA-KOH solution, ELD

started immediately after the addition with an abrupt OCP increase. However, the deposition started slowly, and the OCP decreased gradually in the case of 10 mM HCHO addition to Cu-EDTA-KOH solution, though the amount of HCHO was the same as that of Cu ions. (The concentration of the injected HCHO was one-tenth of the HCHO concentration in the full ELD solution.) The deposition rate was also slow compared to the case of Cu ion addition. This implied that HCHO required some time to become activated on the surface and suggested that the oxidation of HCHO was a rate determining step in Cu ELD.[103] These two OCP values converged regardless of the deposition rate. The OCP of the electrode was considered to have been mostly affected in large portion by the adsorption of HCHO rather than other chemicals, resulting in the similar OCP during Cu ELD. Though the OCP did not exhibit any clear dependency on the deposition rate, Cu ELD was considered to have followed the mixed potential theory to a certain extent.

Figure 3.8 shows the OCP and mass change after the addition of HCHO, which showed the slower response compared to the Cu ion addition. The deposition was not initiated when 5 mM of HCHO was added to Cu-EDTA-KOH solution. Slight decrease in OCP was observed, however, the mass of the electrode was continuously decreased, since the concentration of HCHO was estimated to be too low to inhibit the dissolution by EDTA. The deposition was initiated after the addition of HCHO exceeding 10 mM. The OCP decrease and deposition rate increase after the addition became faster with increasing HCHO concentration. 60 s ~ 90 s from the injection time elapsed for the deposition rate reaching steady-state. The deposition rates at

steady-state in both 10 mM and 20 mM cases were 0.04 μg/s (14 nm/min) and 0.05 μg/s (18 nm/min), respectively. (Figure 3.8 (b) inset) It was considered that the period was related to the time that methylene glycol anions adsorbed and became activated on the Cu surface. The induction period observed in Figure 3.5 might be also attributed to the adsorption and activation of methylene glycol anions.

Table 3. 1. Calculated Oxide Thickness according to the Immersion time

Solution	Immersion time	Cu_2O thickness
KOH	50 s	1.70 nm
	100 s	3.25 nm
	400 s	4.14 nm
EDTA-KOH	50 s	1.62 nm
	100 s	2.07 nm
	200 s	1.62 nm
	400 s	1.54 nm
HCHO-EDTA-KOH	50 s	1.63 nm
	100 s	1.87 nm
	400 s	1.91 nm

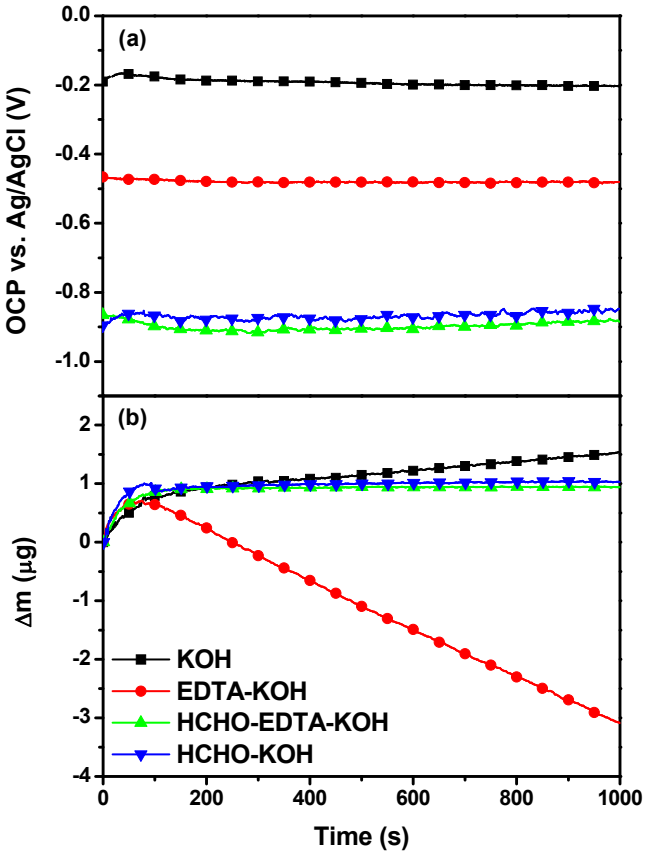

Figure 3. 1. (a) OCP and (b) mass change of cathodically polarized electrodes in KOH, EDTA-KOH, HCHO-EDTA-KOH, and HCHO-KOH solutions.

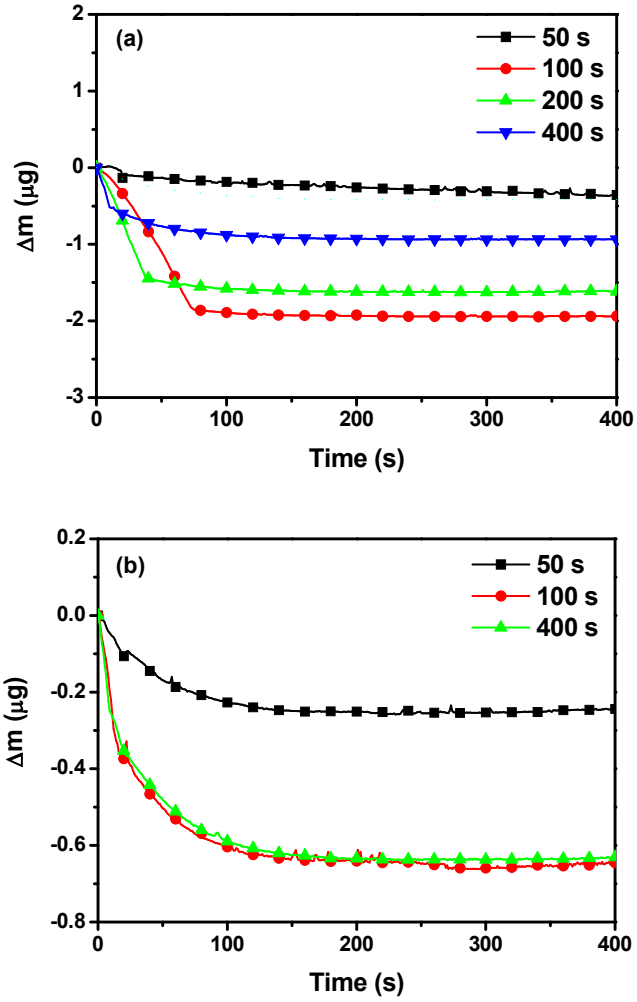

Figure 3. 2. Dependence of mass change during CR on the immersion time in (a) EDTA-KOH and (b) HCHO-EDTA-KOH solutions.

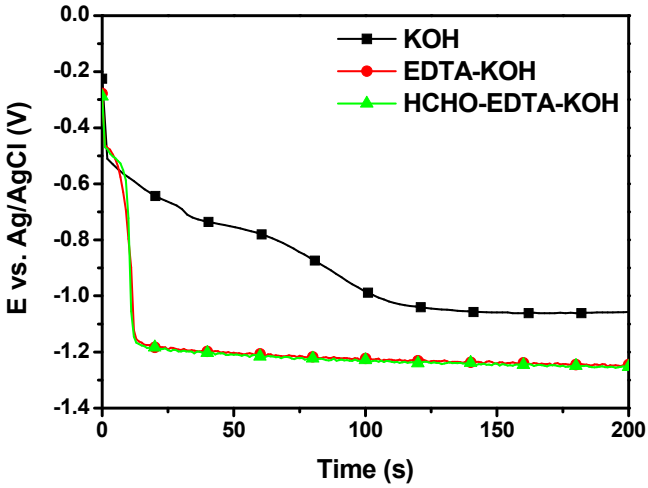

Figure 3. 3. Potential-time curves during CR after the immersion in KOH, EDTA-KOH, and HCHO-EDTA-KOH solutions for 400 s.

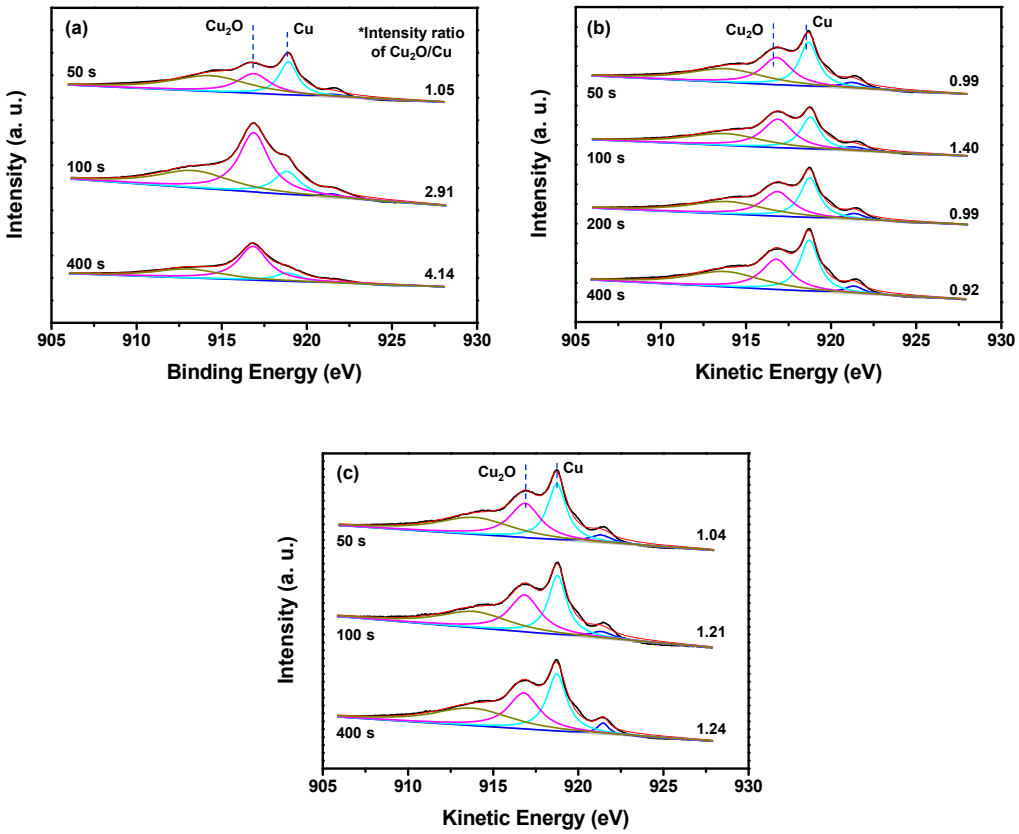

Figure 3. 4. XPS spectra of Auger Cu $L_3M_{4,5}M_{4,5}$ according to the immersion time in (a) KOH, (b) EDTA-KOH, and (c) HCHO-EDTA-KOH.

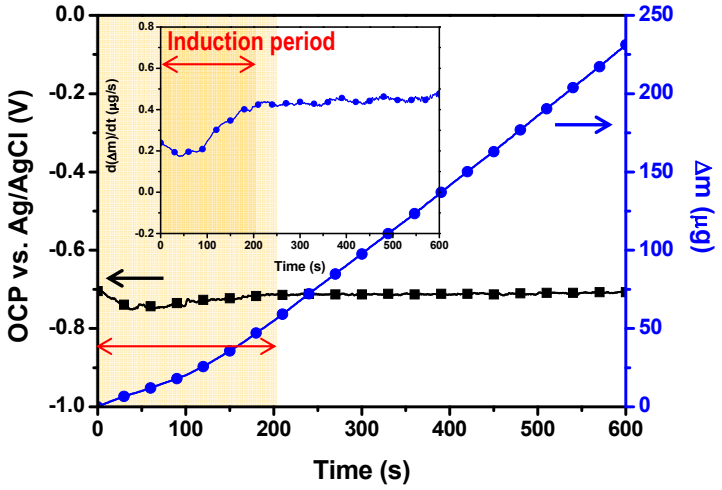

Figure 3. 5. OCP and mass change of cathodically polarized electrode in full ELD solution. (inset: d(Δm)/dt vs. time)

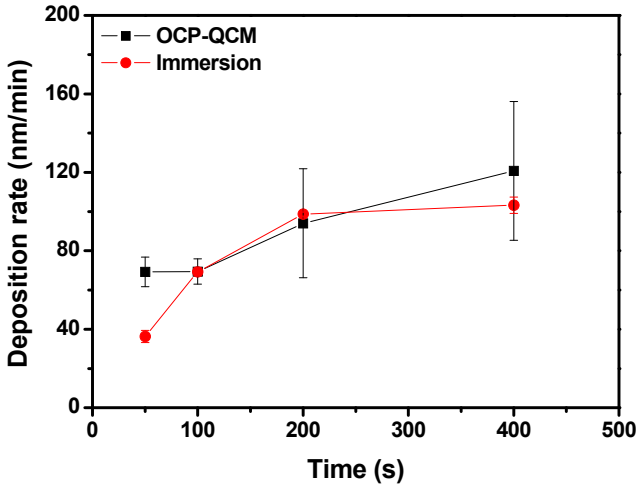

Figure 3. 6. Change of the deposition rate according to immersion time. In the case of the immersion process, the deposition rate was calculated from the change of sheet resistance before and after the deposition.

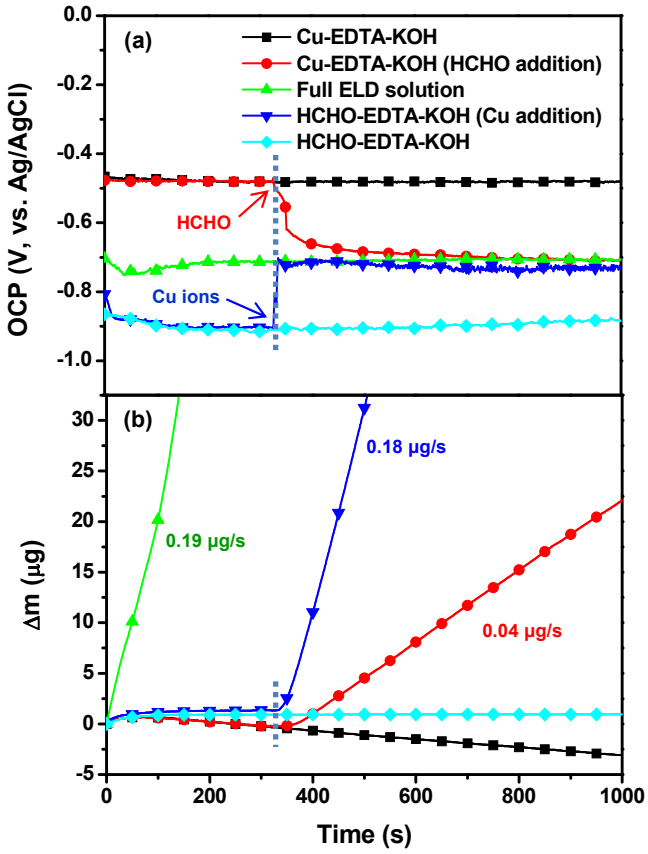

Figure 3. 7. (a) OCP and (b) mass change of cathodically polarized electrodes in various solutions. The added amount at 330 s was 10 mM for both Cu ions and HCHO.

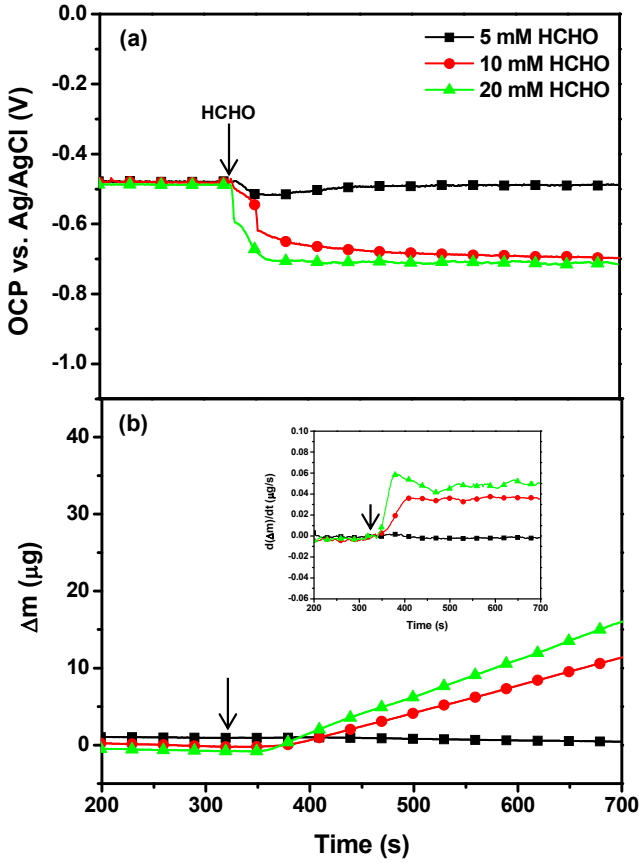

Figure 3. 8. (a) OCP and (b) mass change of cathodically polarized electrodes in Cu-EDTA-KOH solution. HCHO was added at 330 s. (Figure 7 (b) inset: d(Δm)/dt)

3.2. Effect of Cu oxide on Cu ELD

3.2.1. Adsorption of HCHO on oxidized Cu surface

In order to observe the effect of Cu oxide on Cu ELD, Cu oxide was formed after the cathodic polarization before the electrochemical measurement. Figure 3.9 shows XPS spectra of Cu 2p on the electrode. Only metallic Cu $2p_{3/2}$ was detected at 932.3 eV when the native Cu oxide was removed by the cathodic polarization. Cu 2p peaks were shifted to high binding energy region after the oxidation. The chemical shift was more obvious after H_2O_2 oxidation than air oxidation, indicating that the larger amount of Cu oxide with the higher oxidation state was formed. It was revealed that the oxide formed by both air and H_2O_2 oxidation was composed of both Cu_2O and CuO, as reported that Cu $2p_{3/2}$ binding energies of Cu_2O and CuO were 932.4 eV and 933.6 eV, respectively.[104,105] The oxide thickness after the air oxidation was calculated from the XPS spectra and it was 1.63 nm. The thickness of chemically-formed oxide was about 11.03 nm, which was calculated from QCM data.

The prepared electrodes were immersed in HCHO-KOH solution during the electrochemical measurement. Figure 3.10 (a) and (b) shows the OCP and mass change of the electrodes. HCHO was reported to exist as methylene glycol anions in the alkaline ELD solution. These anions adsorb and reduce Cu ions on the surface during ELD. On the cathodically polarized electrode, the OCP was placed around -0.9 V which indicated that methylene glycol anions adsorbed on the surface. The mass of the electrode also remained constant after 100 s because adsorbed

methylene glycol anions inhibited the further oxidation in the alkaline media. The mass increase in 100 s was found to be related to both the Cu_2O formation by dissolved oxygen and the adsorption of other chemicals on the electrode. When the Cu oxide was formed on the surface before the electrochemical measurement, the adsorption of methylene glycol anions showed a different behavior. On the air-oxidized electrode, the OCP was not much decreased as that of the cathodically polarized electrode and the mass was steadily increased by the Cu oxidation even methylene glycol anions were present in the solution. The OCP was slightly decreased at the beginning but it gradually increased again as the oxide grew. The OCP of the electrode after the H_2O_2 oxidation was also located at the less negative potential (-0.23V). The mass increase was also observed, however, the increase rate was slow because the thick oxide already covered the surface. The initial mass increase on both oxidized electrodes during the immersion was small compared to the cathodically polarized electrode because the pre-formed oxide was so thick that the diffusion of the dissolved oxygen into the film was retarded. From both results, it could be concluded that methylene glycol anions rarely adsorbed on the oxidized surface.[106]

However, when EDTA co-existed in the solution, the OCPs of oxidized electrodes decreased to the value around -0.9 V from the start of the immersion with the simultaneous mass decrease as shown in Figure 3.11. After the mass decrease, the same trend was observed as the case of the cathodically polarized electrode. The mass reduction at the initial stage was associated with the removal of Cu oxides by EDTA. It was suspected that EDTA removed the pre-formed Cu oxides and exposed Cu on the surface during the period. With the removal of the oxide covering the

surface, a small amount of Cu_2O also started to be formed with the adsorption of methylene glycol anions, resulting in re-increase in mass. The adsorbed methylene glycol anions then inhibited the further oxidation. Comparing Figure 3.11 with Figure 3.10, it was verified that the removal of Cu oxides helped the adsorption of methylene glycol anions.

3.2.2. Cu ELD on oxidized Cu surface

The graphs in Figure 3.12 are the OCP and mass change of the electrodes in the full ELD solution after the Cu oxide formation. On the cathodically polarized electrode, OCP was at -0.71 V and the deposition commenced right after the immersion. However, the OCP of the oxidized electrode was located above -0.5 V at the beginning. It was then decreased to the value similar with the OCP of the cathodically polarized electrode in a few seconds. The mass of the electrode was reduced in this region even the electrode was immersed in the full ELD solution. This phenomenon was also ascribed to the dissolution of Cu oxides. EDTA removed the Cu oxide covering the most part of the electrode at the initial stage, causing the mass reduction. However, while EDTA increased the area of exposed Cu surface during the dissolution, methylene glycol anions also adsorbed and reduced Cu ions on the surface. Those two reactions occurred simultaneously at the initial stage of the deposition. For example, after the H_2O_2 oxidation in Figure 3.12 (b), the mass of the electrode was reduced until 10 s. During this time, the dissolution amount of Cu oxides exceeded the amount of deposited Cu because the most part of

the surface was covered by the oxides. The mass increase after 10 s indicated that the deposition started to dominate the mass change according as the Cu oxide was removed.

The existence of pre-formed Cu oxides also strongly affected the surface evolution during Cu ELD. Figure 3.13 showed the sheet resistance change and surface roughness of the deposited films according to ELD time. The decrease in the sheet resistance was observed right after the immersion, and the surface roughness was gradually increased with the deposition time on the cathodically polarized surface in Figure 3.13 (a) and (b). The gradual increase in the surface roughness was suspected to result from natural film growth as the film was thickened. The sheet resistance change of the oxidized electrode in Figure 3.13 (a) demonstrated that Cu ELD hardly took place at the beginning. The amount of the sheet resistance decrease on the air-oxidized surface before 3 s was smaller than that of the cathodically polarized surface because the pre-formed Cu oxides were first removed by EDTA. A small amount of oxides formed by the air affected the surface roughness little as shown in Figure 3.13 (b). The lower initial surface roughness and smaller deposition amount of the air-oxidized surface resulted in the lower surface roughness than the cathodically polarized surface, throughout the deposition. In the case of the H_2O_2 oxidation, however, the sheet resistance of the Cu film was kept almost constant until 6 s of Cu ELD during the dissolution of Cu oxides. Small decrease in the sheet resistance in initial 6 s may be mainly originated from the oxide dissolution. The high surface roughness caused by the oxide formation at 0 s was dramatically reduced at 6 s, supporting that the large part of Cu oxides was removed during the period. It was likely that the dominant Cu ELD was

initiated on the surface after 6 s, causing the re-increase in surface roughness. However, the increase amount in the surface roughness was relatively large on the H_2O_2 oxidized surface compared to that of the cathodically polarized surface. Figure 3.14 shows surface morphologies at 12 s of ELD. On the H_2O_2-oxidized surface, many large protrusions were observed while the surface morphologies were similar with each other in the cases of the cathodically polarized and air oxidized electrodes. Since the remaining Cu oxide inhibited the adsorption of methylene glycol anions during Cu ELD, Cu nucleation at the initial stage of the deposition had to be poor.

The XPS spectra of Cu 2p on the H_2O_2 oxidized surface according to the deposition time are shown in Figure 3.15 (a). It was observed that CuO was removed from the surface as the deposition progressed. The intensity of Cu $2p_{3/2}$ for metallic Cu at 923.3 eV was increased with the deposition time while the peak at the higher binding energy, which was regarded as CuO, was decreased. The evanishment of the satellite peak in the rage from 937.5 eV to 945.0 eV also corroborated the removal of CuO. The existence of Cu_2O during the deposition was observed by Auger Cu $L_3M_{4,5}M_{4,5}$ peak as shown in Figure 3.15 (b). It was reported that the differentiation between Cu and Cu_2O was more simple in Auger Cu $L_3M_{4,5}M_{4,5}$ peaks than in Cu 2p peaks because the energy difference between them was large: 916.8 eV for Cu2O and 918.7 eV for Cu. The metallic Cu started to be observed at 6 s of the deposition, indicating that Cu_2O was also removed from the surface. The intensity of Cu was steadily increased until 12 s, though a small amount of Cu_2O was also observed.

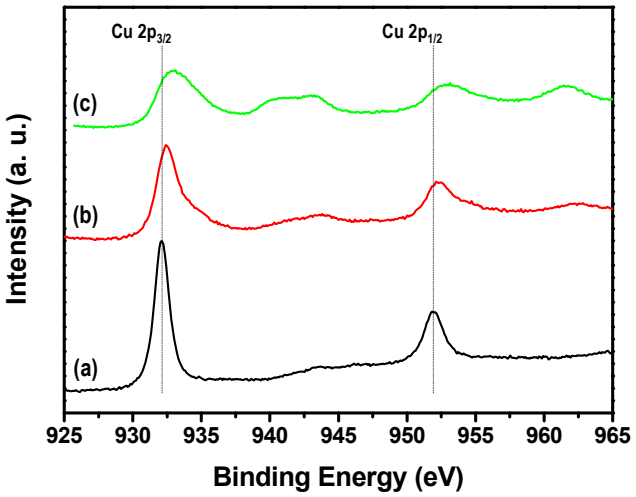

Figure 3. 9. XPS spectra of Cu 2p on Cu electrodes (a) after the cathodic polarization, (b) air oxidation, and (c) H_2O_2 oxidation.

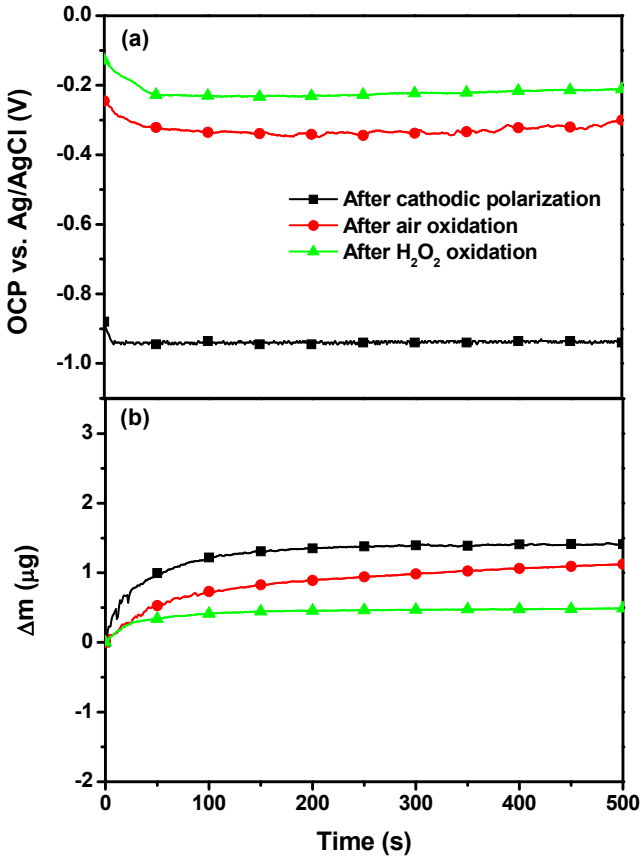

Figure 3. 10. (a) OCP and (b) mass change of electrodes in HCHO-KOH.

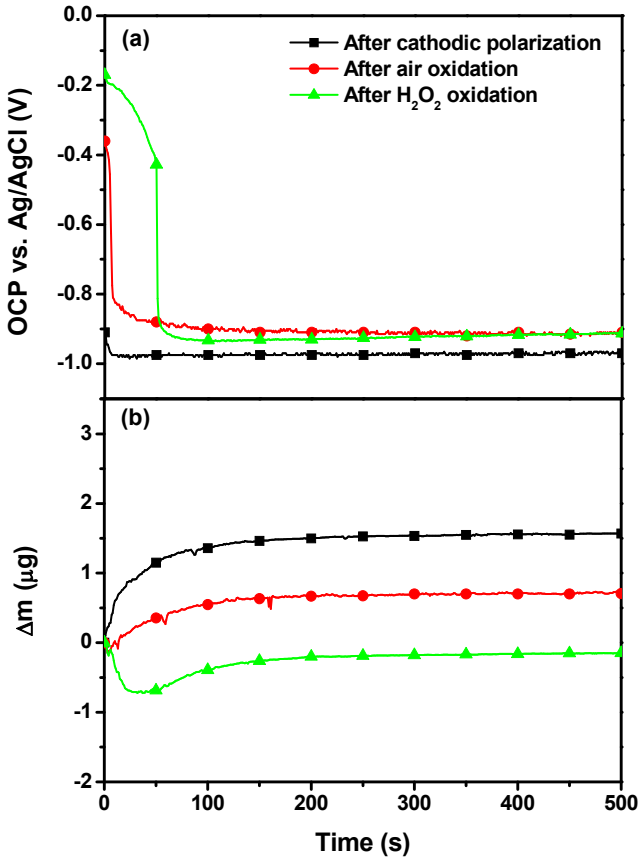

Figure 3. 11. (a) OCP and (b) mass change of electrodes in HCHO-EDTA-KOH.

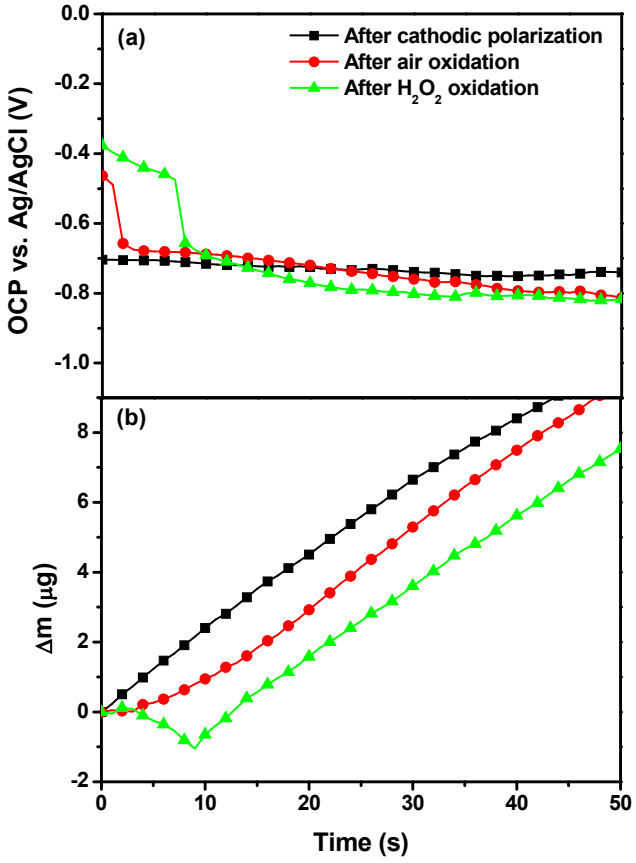

Figure 3. 12. (a) OCP and (b) mass change of electrodes in the full ELD solution.

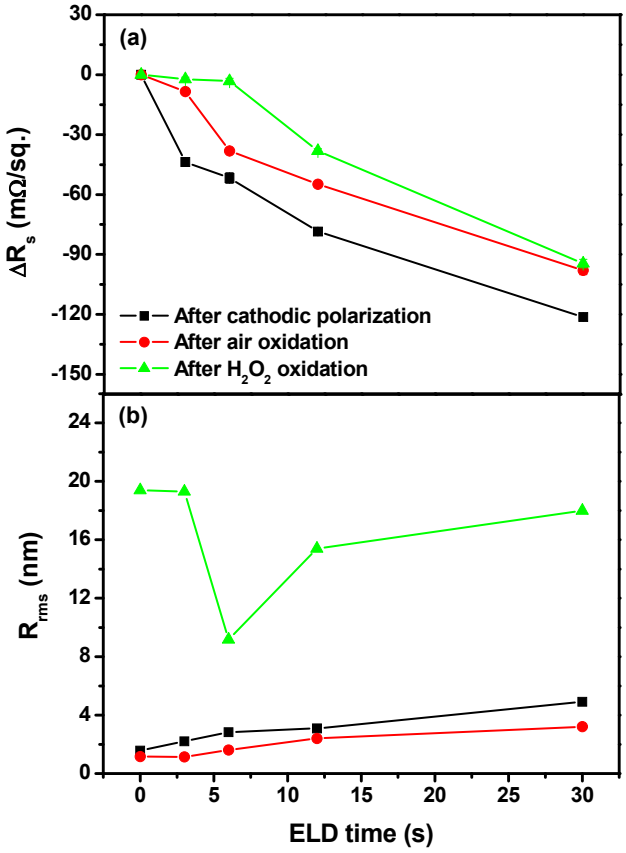

Figure 3. 13. (a) Sheet resistance change (ΔR_s) and (b) surface roughness (R_{rms}) of electroless Cu films according to the deposition time. ΔR_s was calculated by subtracting the initial sheet resistance from the measured one after Cu ELD.

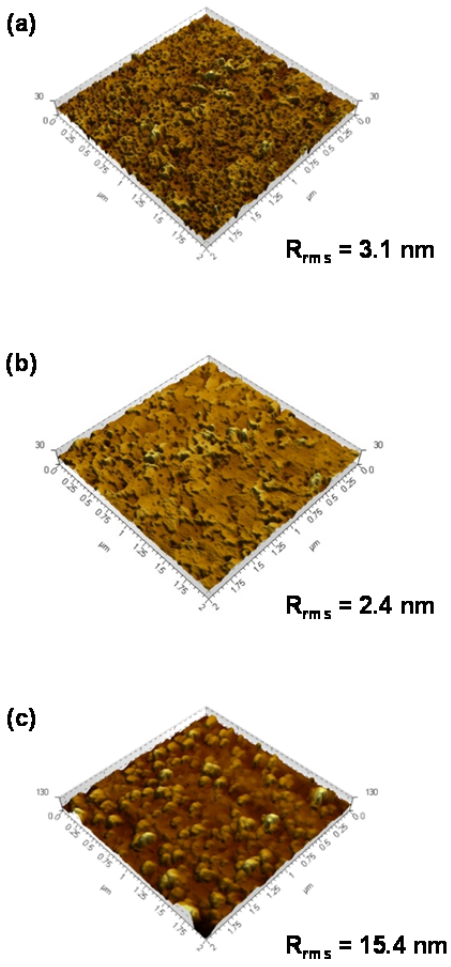

Figure 3. 14. Surface morphologies of electroless Cu films after (a) the cathodic polarization, (b) air oxidation, and (c) H_2O_2 oxidation. The deposition time was 12 s.

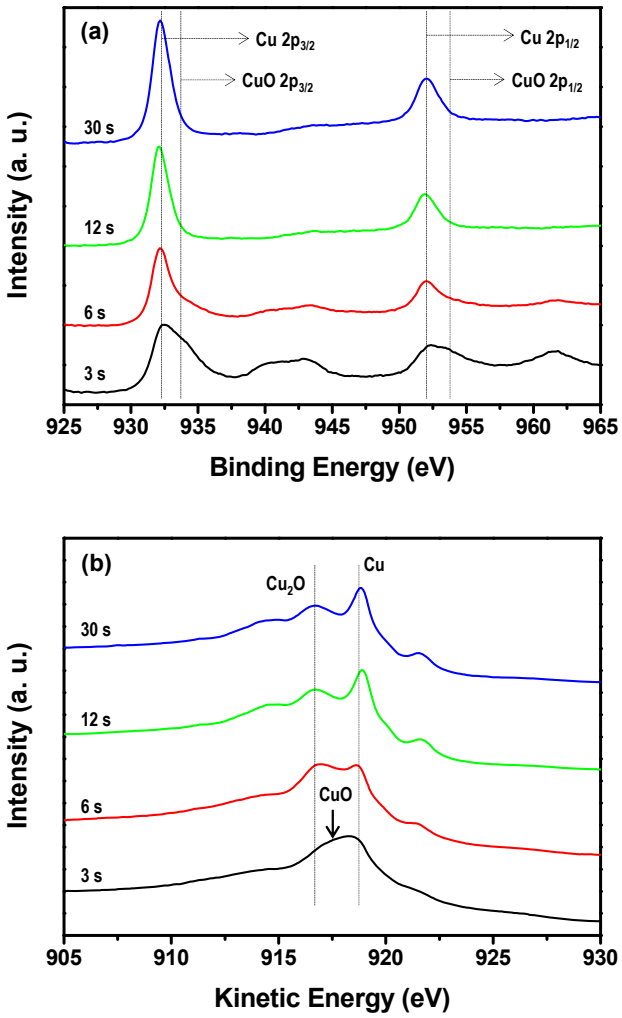

Figure 3. 15. XPS spectra of (a) Cu 2p and (b) Auger Cu $L_3M_{4,5}M_{4,5}$ on the H_2O_2 oxidized Cu electrode according to the deposition time.

3.3. Summary

The Cu ELD mechanism was studied in real-time using the combination of OCP measurement and QCM. It was revealed that EDTA removed Cu oxides during the immersion by the complexation. Methylene glycol anions, the form of HCHO in alkaline solution, were adsorbed on the Cu surface and inhibited further Cu oxidation or dissolution. A small amount of Cu_2O was formed during the immersion in EDTA-KOH and HCHO-EDTA-KOH solutions. In the full ELD solution, the induction period was observed in the initial stage of the deposition, and it was found that the adsorption and activation of methylene glycol anions on the surface was one of causes. The location of OCP during Cu ELD between the OCPs of the half-cell solutions and the OCP movement by the addition of Cu ions or HCHO suggested that Cu ELD followed the mixed potential theory.

The oxide effect on Cu ELD was also studied. It was verified again that EDTA removed Cu oxides during Cu ELD by the complexation. Methylene glycol anions adsorbed on the surface after EDTA removed the pre-formed oxide. Using both EDTA and HCHO in Cu ELD solution facilitated Cu deposition whether Cu surface was oxidized or not. However, the existence of Cu oxides resulted in the high surface rougness of the deposit because of the irregular adsorption of methylene glycol anions leading the poor Cu nucleation at the initial stage.

Chapter IV. Effect of organic additives on Cu ELD

4.1. PEG

4.1.1. Adsorption behavior of PEG during Cu ELD

Figure 4.1 (a) shows the OCP change according the injection amount of PEG8000 (Mw. 8000) during Cu ELD. The OCP was maintained constant value of ca. -0.70 V before the PEG8000 injection. After the injection at 200 s, the OCP started to decrease and converged on the similar OCP value (ca. -0.90 V) in a few tens of seconds, even though the concentration of PEG8000 was different. The concentration of PEG affected the decrease rate of OCP: the higher concentration resulted in the faster decrease in the OCP. The mass change during the OCP measurement was also shown in Figure 4.1 (b). The mass increase was gradually suppressed after the PEG8000 was injected. The suppression effect according to the PEG concentration was clearly observed in Figure 4.1 (b) inset. The initial deposition rate without PEG was ca. 0.55 μg/s, and it began to decrease after the PEG8000 injection. The decrease rate became fast as the concentration of PEG8000 increased. However, the deposition rate was also saturated in several tens of seconds regardless of the concentration. The saturated deposition rate was ca. 0.02 μg/s. The change in the deposition rate exhibited the same trend as the change of OCP. It indicated that the adsorption of PEG8000 induced the decrease in OCP value with the suppression of the deposition. Thus, the decrease rate of the OCP and deposition rate can be regarded as the

adsorption speed of PEG8000, and the convergence of both values signifies the saturation of PEG8000 adsorption on the surface.

It is known that the adsorbed PEG blocks the active sites for Cu ELD, which results in the suppression effect. Figure 4.2 shows the OCP and mass change of the electrode in the HCHO-free Cu ELD bath consisting of 0.03 M $CuSO_4 \cdot 5H_2O$ and 0.05 M EDTA (pH 12.8) with and without PEG8000. Before the injection of HCHO, the OCP without the injection of PEG8000 was located ca. -0.49 V and the mass was continuously decreased with the rate of 0.01 μg/s by the dissolution of Cu through the complexation with EDTA. Both two values were merely changed after 0.50 μM of PEG8000 was injected at 200 s, indicating that the adsorption of PEG8000 had little influence on the dissolution behavior of Cu. It was suspected that the continuous dissolution of Cu disturbed the stable adsorption of PEG8000 on the surface. However, the obvious different behavior was observed when 0.10 M of HCHO was injected at 400 s. In the PEG-free bath, the OCP value dropped to ca. -0.70 V after the injection with the fast increase in the deposition rate up to 0.50 μg/s as the deposition started. The sudden decrease to -0.7 V in the OCP was also observed in the presence of PEG8000 after the HCHO injection. The deposition rate was increased up to 0.20 μg/s at the same time, but it was then gradually decreased with the further decrease in the OCP. It seemed that PEG8000, which was not strongly adsorbed on the surface when HCHO was absent, began to adsorb on the surface as HCHO inhibited the dissolution of Cu and induced the deposition process. Therefore, the increase speed of the deposition rate was similar with that of the PEG-free case at the initial

stage of the HCHO injection. As PEG8000 adsorbed on the surface after the injection of HCHO stopped the dissolution, the deposition rate decreased. The adsorption of PEG8000 then reduced active sites for the HCHO adsorption.

Assuming that the OCP change was related with the coverage of PEG on Cu surface, coverage vs. time graph was obtained according to the molecular weight of PEG by using the following equation:

$$\text{PEG coverage } (\theta) = (E_i - E_t)/(E_i - E_s) \quad [4.1]$$

where E_i is the initial OCP prior to the PEG injection, E_s is the OCP after the saturation, and E_t is the OCP at the given time. The graphs are shown in Figure 4.3, Figure 4.4, and Figure 4.5 with different PEG molecular weight. The coverage of PEG was increased steadily from the injection time and reached the saturation coverage ($\theta = 1$) in all cases. However, the time required to reach the saturation coverage was dependent on the concentration and molecular weight of PEG.

The adsorption kinetics of organic additives during the deposition is generally simulated by considering both the diffusion and adsorption itself. The general relation between the rate of surface coverage change and the concentration gradient at the electrode surface is expressed by[107]

$$\partial\theta/\partial t = (D/\Gamma_s)\cdot(\partial C/\partial x)_{x=0} \quad [4.2]$$

where θ is the surface coverage ($0 \leq \theta \leq 1$), t is time, Γ_s is the saturation coverage, x is the distance from the electrode surface, and D and C are the diffusion coefficient and concentration of adsorbate, respectively.

When the adsorption is controlled by the diffusion process, the concentration of adsorbate at the electrode surface is significantly lower than the bulk concentration (C*). In this case, the concentration at the surface can be regarded as zero for all t. Assuming that the adsorption is confined to a monolayer, following analytical solution can be obtained;[108]

$$\theta = 1\text{-}\exp[-(t/T)^{1/2}] \quad [4.3]$$

where $T = (\pi\Gamma_s^2)/(4DC^{*2})$. There is no term associated with the effect of adsorbate because the adsorption is totally controlled by the diffusion.

On the contrary, the diffusion can be much faster than the adsorption rate of adsorbate. As the amount of consumed adsorbate by the adsorption process is much smaller than that diffusing from the bulk, the surface concentration is considered to be same with the bulk concentration. The rate of the adsorption is determined by[108]

$$\theta = 1\text{-}\exp[-(kC^*/\Gamma_s)\cdot t] \quad [4.4]$$

where k denotes the adsorption rate constant. In the both two cases, it is assumed that the adsorption follows Langmuir-like behavior with no desorption.

The diffusion-controlled and adsorption-controlled kinetics were also simulated in Figure 4.3, Figure 4.4, and Figure 4.5. The desorption of PEG and the competitive adsorption between PEG and HCHO were neglected because the coverage of PEG reached the unity ($\theta = 1$) in all cases regardless of the PEG concentration as shown in Figure 4.1. The diffusion coefficient and saturation coverage of PEG used in the simulation were listed in Table 4.1. The diffusion coefficient according to the molecular weight was calculated from the empirical relation, $D = 1.465 \times 10^{-4} \times M^{-0.557}$, where M is the molecular weight of PEG.[109] The saturation coverage was estimated from the projected area of PEG. The area was calculated from the hydrodynamic radius of PEG, assuming PEG was spherical.[110] The diffusion coefficient and saturation coverage were decreased with the increase in the molecular weight of PEG. The adsorption rate constant used in the simulation was 0.002 cm/s.[107]

The adsorption behavior of PEG1500 is shown in Figure 4.3. At 0.25 μM, the adsorption nearly followed the diffusion-controlled model. It suggested that the adsorption rate of PEG1500 was much faster than the diffusion at the low concentration. As the concentration increased, the adsorption began to follow the adsorption-controlled model as shown in Figure 4.3 (b) and (c). The increase in the bulk concentration, which led to the high diffusion flux of PEG1500 from the bulk to the surface, changed the adsorption behavior from the diffusion-

controlled model to the adsorption-controlled model. The high diffusion coefficient of PEG1500 was also supposed to contribute such a change. However, the coverage change still followed the diffusion-controlled model before 20 s in the both cases. The concentration of PEG1500 at the electrode surface was so low that the adsorption was temporally influenced by the diffusion at the initial stage of the adsorption.

Figure 4.4 and 4.5 show the adsorption behavior of PEG8000 and PEG100000, respectively. The adsorption of both PEGs was totally governed by the diffusion irrespective of their bulk concentration. The diffusion-controlled adsorption of PEGs having high molecular weight was originated from their low diffusion coefficient. It was suspected that the behavior was controlled by the adsorption at the high surface coverage ($\theta \approx 1$) because the adsorption rate became slower as the coverage increased. However, in the experiment, the adsorption-controlled kinetics at the high surface coverage was not easy to be distinguished. The result was corresponded with other reports. The result was corresponded with other reports. U. Landau et al. suggested that the adsorption rate constant of PEG4000 was much higher than the mass transfer coefficient, resulting in the diffusion-controlled adsorption during Cu ED.[111] Mota et al. also reported that the adsorption of PEG8000 on mercury electrode followed the diffusion-controlled adsorption when the surface coverage was below 0.8.[107]

At the same concentration, the time required to reach the saturation coverage seemed to be the shortest when the molecular weight of PEG was 100000 even its diffusion coefficient was the smallest. It was due to the smallest saturation coverage of PEG100000. The diffusion

coefficient and saturation coverage became low as the molecular weight of PEG increased. Therefore, Γ_s^2/D in Table 4.1, which was the part of T in equation [4.3], was also decreased with the molecular weight. The small Γ_s^2/D caused the fast saturation.

The OCP and mass change of the electrode were measured with the different molecular weight of PEG at the same concentration (0.50 μM) as in Figure 4.6. The injection of PEG decreased the OCP value in all cases, however, the decrease in the OCP was increased as the molecular weight increased. The change in the deposition rate in Figure 4.6 (b) inset showed the almost same trend. The OCP of PEG1500 after the saturation was only ca. -0.81 V and the deposition rate was reduced to 0.08 μg/s, while those values of PEG8000 were ca. -0.90 V and 0.02 μg/s, respectively. The addition of PEG100000 decreased the OCP to ca. -0.93 V with the deposition rate of 0.01 μg/s after the saturation. It suggested that PEG having the higher molecular weight gave the stronger suppression effect with the fast saturation time at the same molar concentration. The strong suppression effect of PEG100000 was supposed to mainly come from its large size. The steric hindrance of the large molecule effectively disturbed the adsorption of HCHO during the deposition.

The OCP and mass change were also measured at the same monomer concentration, and it was shown in Figure 4.7. The molar concentration of PEG1500, PEG8000, and PEG100000 were 2.7 μM, 0.50 μM, and 0.04 μM, respectively. At the same monomer concentration, the saturation time was the shortest in the case of PEG1500 while PEG100000 showed the slowest adsorption. However, the OCP value after the saturation was less negative than those of

PEG8000 and PEG100000 as also observed in Figure 4.6. The slower saturation time in the higher molecular weight was associated with both the molar concentration and diffusion coefficient of PEG. As the bath containing PEG with high molecular weight had the small number of PEG molecules at same monomer concentration, the saturation time had to be slow. However, the suppression effect after the saturation was still strong at the high molecular weight.

Figure 4.8 shows the change of the deposition rate according to PEG concentration with different molecular weight without electrochemical measurement. The deposition was performed for only 1 min to characterize the adsorption behavior of PEG. Figure 4.8 (a) shows the deposition rate according the molar concentration of PEG. PEG1500 showed the weakest suppression effect even the concentration was higher than those of other PEGs. The time to reach the saturation coverage was the longest, and the deposition rate after the saturation was also the highest. Therefore, the deposition amount during 1 min was the largest at the same molar concentration. On the contrary, PEG100000 suppressed the deposition effectively at the low concentration below 0.5 μM because of the fastest adsorption and the lowest deposition rate after the saturation. The deposition rate according to the monomer concentration was depicted in Figure 4.8 (b). The deposition rate of PEG100000 was higher than others below 16 mg/L because the adsorption speed of PEG100000 was slow. The saturation of the deposition rate with the increase in the PEG concentration was also observed in both cases. The two cases were well-matched with Figure 4.6 and 4.7. . It was regarded that the time to reach the saturation coverage seemed to be an important factor affecting the short-time deposition, while the

deposition rate after the saturation might be important in the long-time deposition.

4.1.2. Surface morphology of electroless Cu film with PEG

Figure 4.9 shows the surface morphologies of Cu deposits after ELD according to the PEG molecular weight at the same concentration. The deposition thickness was fixed at ca. 160 nm by controlling the deposition time. The morphology change was related to the size of adsorbed PEG molecules which suppressed the nucleation of Cu during Cu ELD by disturbing the adsorption of HCHO on the surface. It was suspected that the size of Cu nuclei was decreased with the increase of the PEG molecular weight, resulting in the smooth surface with the large PEG. It also demonstrated that the larger PEG suppressed the nucleation more effectively at the same concentration.

However, the effect of the PEG molecular weight on the surface morphology was not clearly apparent at the same monomer concentration compared to the case with the same molar concentration, as shown in Figure 4.10. The surface morphology with PEG1500 did not show big transition even the molar concentration was increased up to 2.7 μM because the suppression effect of PEG1500 was relatively weak. Meanwhile, the surface morphology with PEG100000 was thoroughly changed. The number of molecules of PEG100000 was too small to have strong influence on the morphology during the deposition time (2 min).

4.1.3. Gap-filling with PEG

The adsorption behavior of PEG explained so far showed that the adsorption speed was strongly dependent on its concentration and diffusion coefficient, even though the adsorption was observed on the flat surface. The dependency was expected to be much strengthened when the deposition was performed on a patterned substrate because PEG should diffuse into the bottom of narrow trenches. Figure 4.11 shows the change in the ratio of the film thickness at the bottom to the side-wall of sub-60 nm trenches according to the concentration of PEG8000. The ratio was increased with the increase of the concentration, and finally saturated. It demonstrated that the deposition rate at the bottom was faster that that at the side-wall due to the concentration gradient of PEG inside of the trench. The filling with PEG8000 was then tried as shown in Figure 4.12. However, the filling profile was not obtained with varying the concentration of PEG8000. The top of trenches was closed before the filling, indicating that the suppression effect at the top should be much enhanced. The molecular weight of PEG was increased for the effective suppression at the top. Figure 4.13 showed filling profiles according to the concentration of PEG10000. However, the bottom-up filling was not observed either.

Table 4. 1. Diffusion Coefficient and Saturation Coverage of PEG

	Diffusion coefficient D (cm^2/s)	Saturation coverage Γ_s (mol/cm^2)	Γ_s^2/D ($s \cdot mol^2/cm^6$)
PEG1500	2.49×10^{-6}	4.14×10^{-11}	6.88×10^{-16}
PEG8000	9.81×10^{-7}	6.20×10^{-12}	3.92×10^{-17}
PEG100000	2.40×10^{-7}	3.70×10^{-13}	5.71×10^{-19}

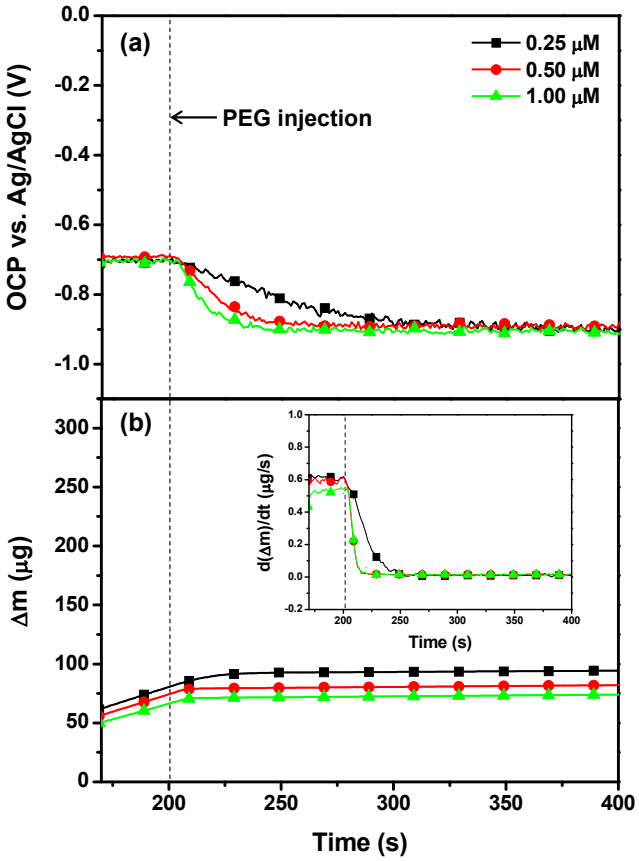

Figure 4. 1. (a) OCP and (b) mass change of Cu electrodes during Cu ELD after the injection of PEG8000. PEG was injected at 200 s. (inset: d(Δm)/dt vs. time)

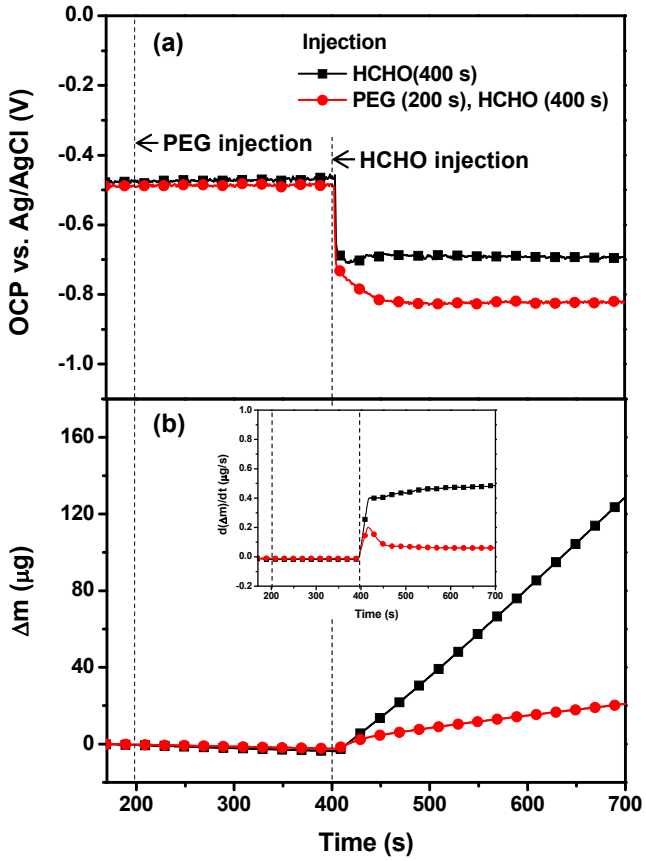

Figure 4. 2. (a) OCP and (b) mass change of Cu electrodes in Cu-EDTA-KOH bath. 0.50 μM PEG8000 and 0.1 M HCHO were injected at 200 s and 400 s, respectively. (inset: d(Δm)/dt vs. time)

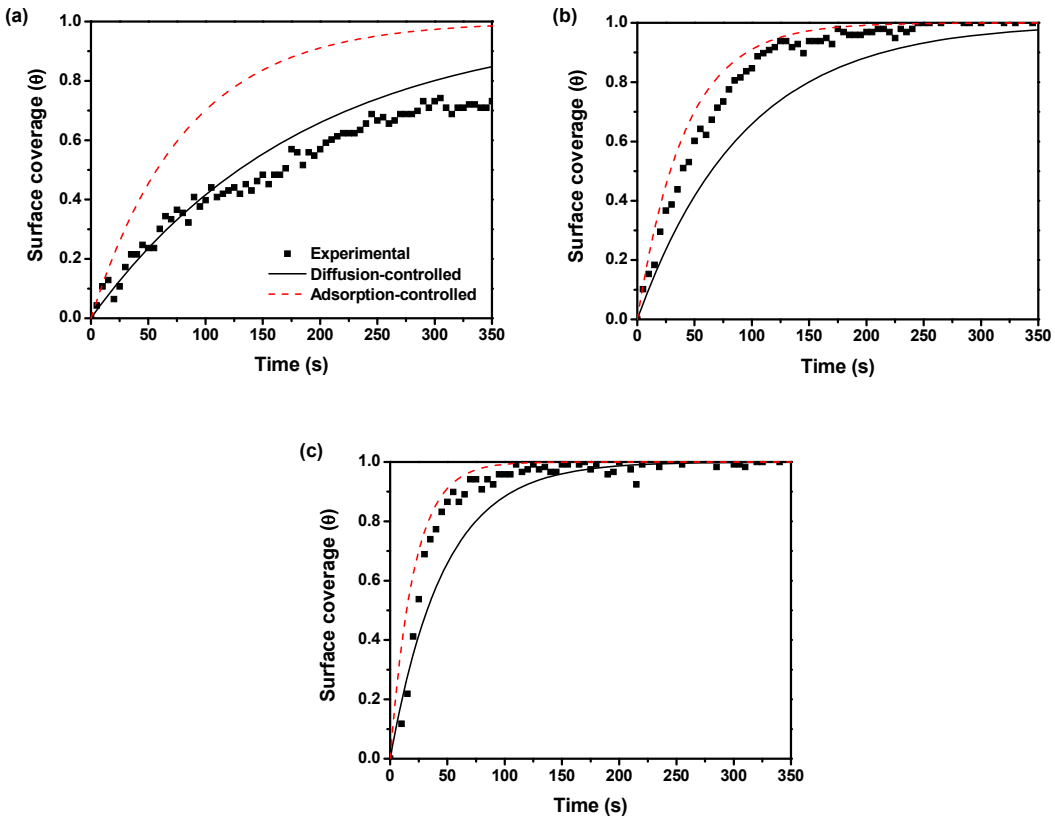

Figure 4. 3. Simulated and experimental surface coverage curves of PEG1500 according to the ELD time with different molar concentration, (a) 0.25 μM, (b) 0.50 μM, and (c) 1.00 μM. The injection time (200 s) was regarded as 0 s.

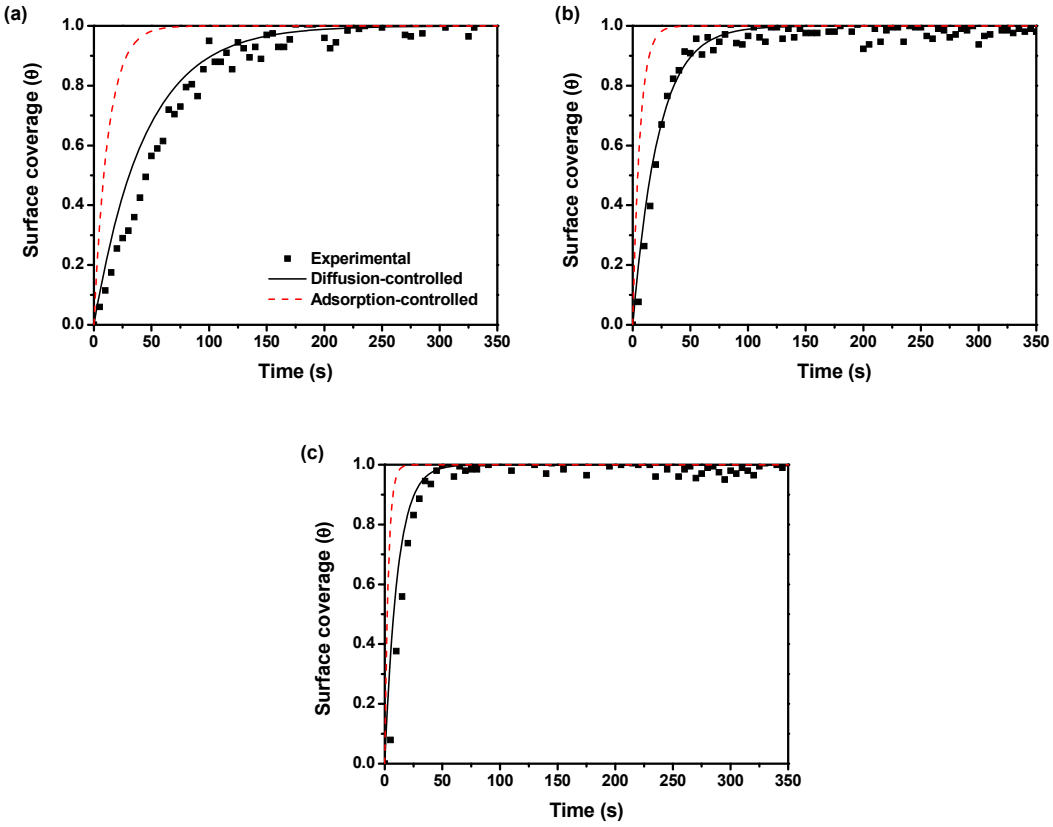

Figure 4. 4. Simulated and experimental surface coverage curves of PEG8000 according to the ELD time with different molar concentration, (a) 0.25 μM, (b) 0.50 μM, and (c) 1.00 μM. The injection time (200 s) was regarded as 0 s.

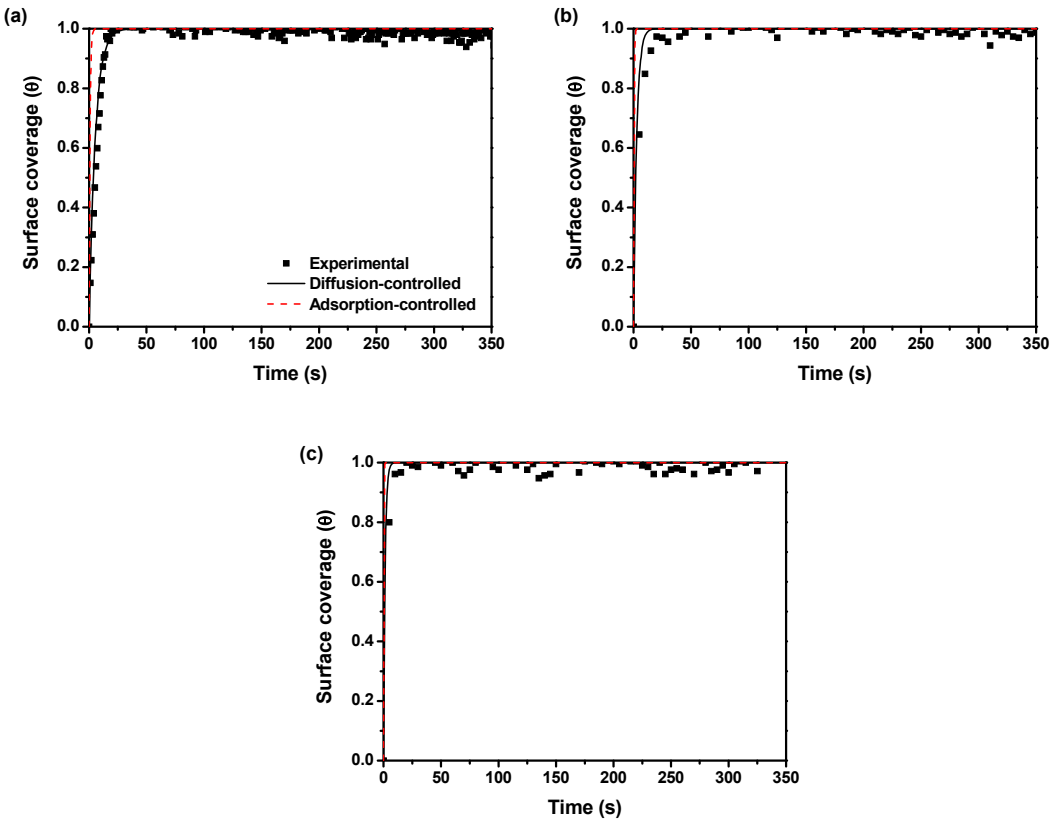

Figure 4. 5. Simulated and experimental surface coverage curves of PEG100000 according to the ELD time with different molar concentration, (a) 0.25 μM, (b) 0.50 μM, and (c) 1.00 μM. The injection time (200 s) was regarded as 0 s.

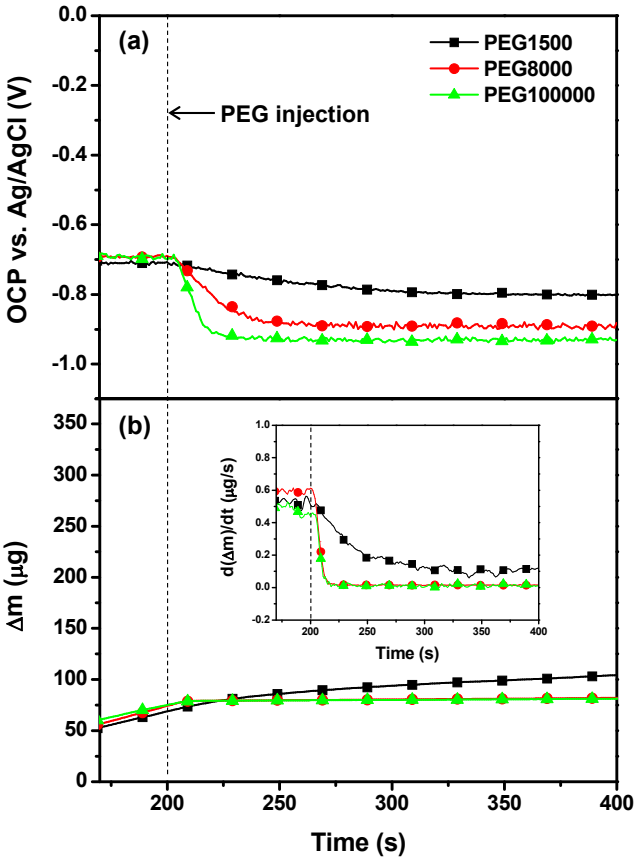

Figure 4. 6. (a) OCP and (b) mass change of Cu electrodes during Cu ELD after the injection of 0.50 μM PEG. PEG was injected at 200 s. (inset: d(Δm)/dt vs. time)

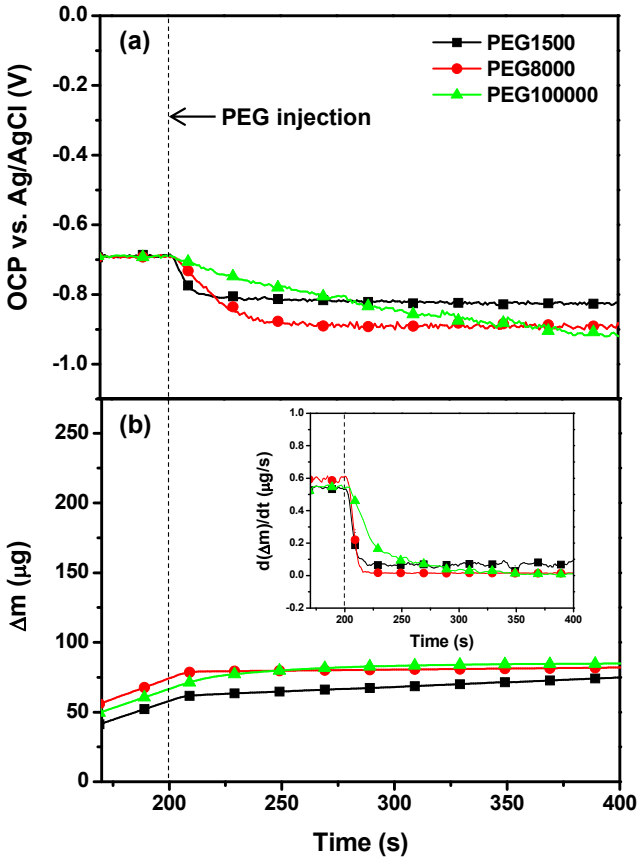

Figure 4. 7. (a) OCP and (b) mass change of Cu electrodes during Cu ELD after the injection of 4 mg/L PEG. PEG was injected at 200 s. (inset: d(Δm)/dt vs. time)

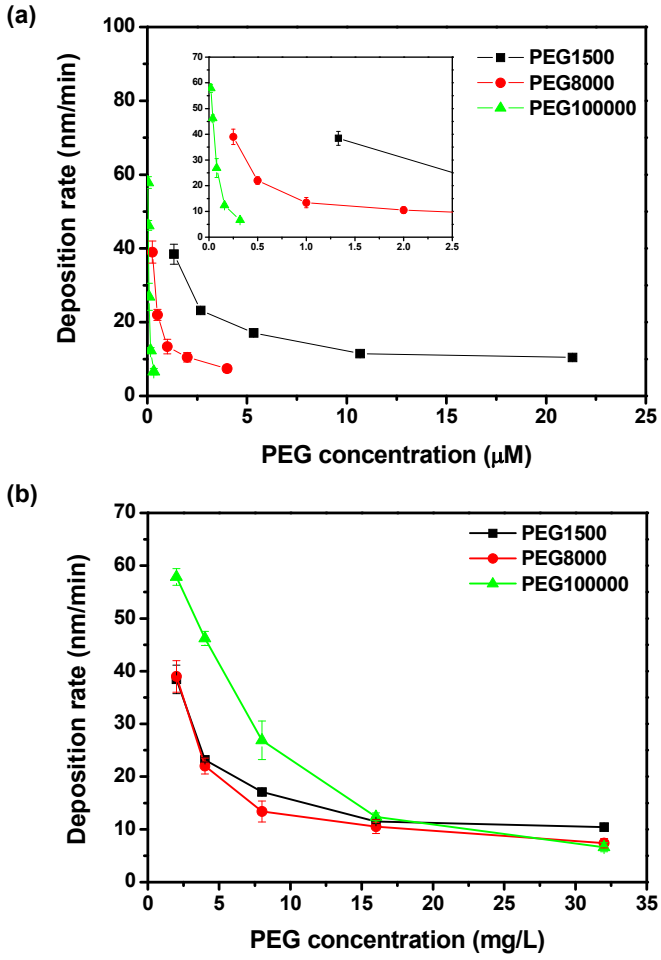

Figure 4. 8. The deposition rate according to the concentration of PEG, (a) molar concentration and (b) mass concentration. The deposition time was 1 min (inset: magnified image in the concentration rage of 0 μM ~ 2.5 μM).

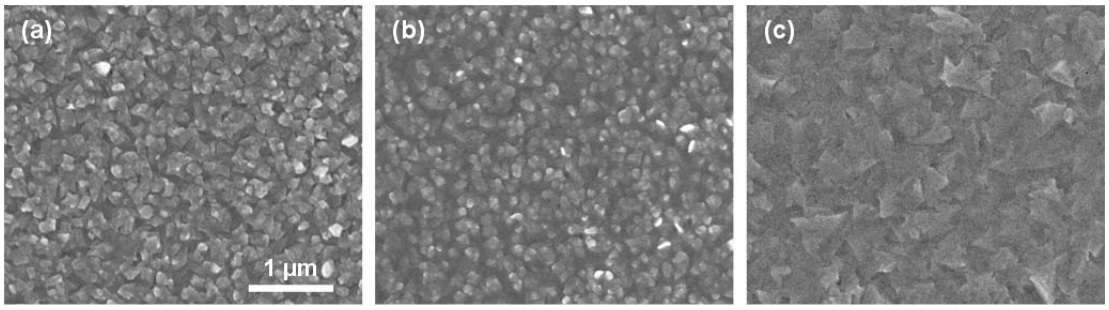

Figure 4. 9. Surface morphologies of Cu deposits with 0.50 μM of (a) PEG1500 (2 min), (b) PEG8000 (4 min), and (c) PEG100000 (45 min). The thickness of the deposits was ca. 160 nm.

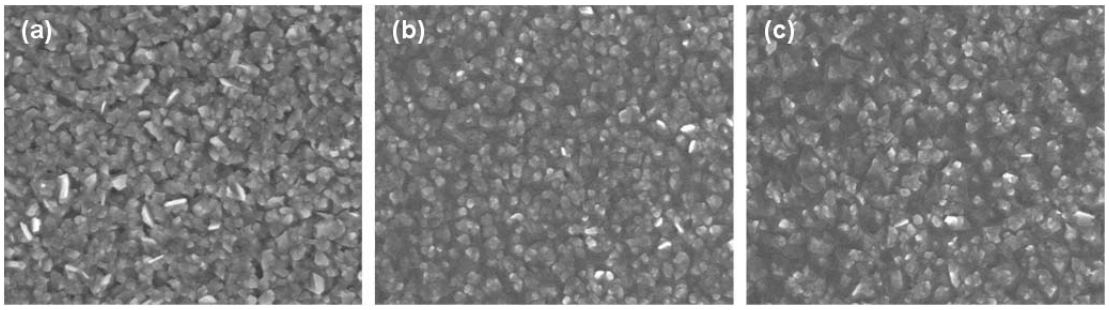

Figure 4. 10. Surface morphologies of Cu deposits with 4 mg/L of (a) PEG1500, (b) PEG8000, and (c) PEG100000. The thickness of the deposits was ca. 160 nm.

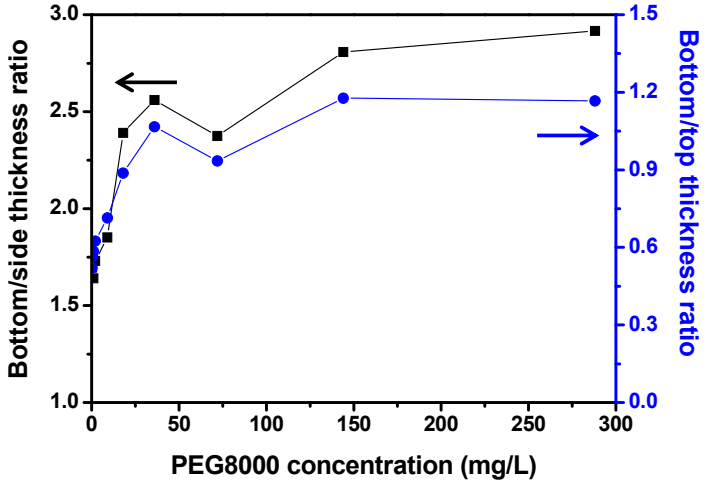

Figure 4. 11. The bottom/side and bottom/top thickness ratio according to the concentration of PEG8000. The deposition time was 1 min.

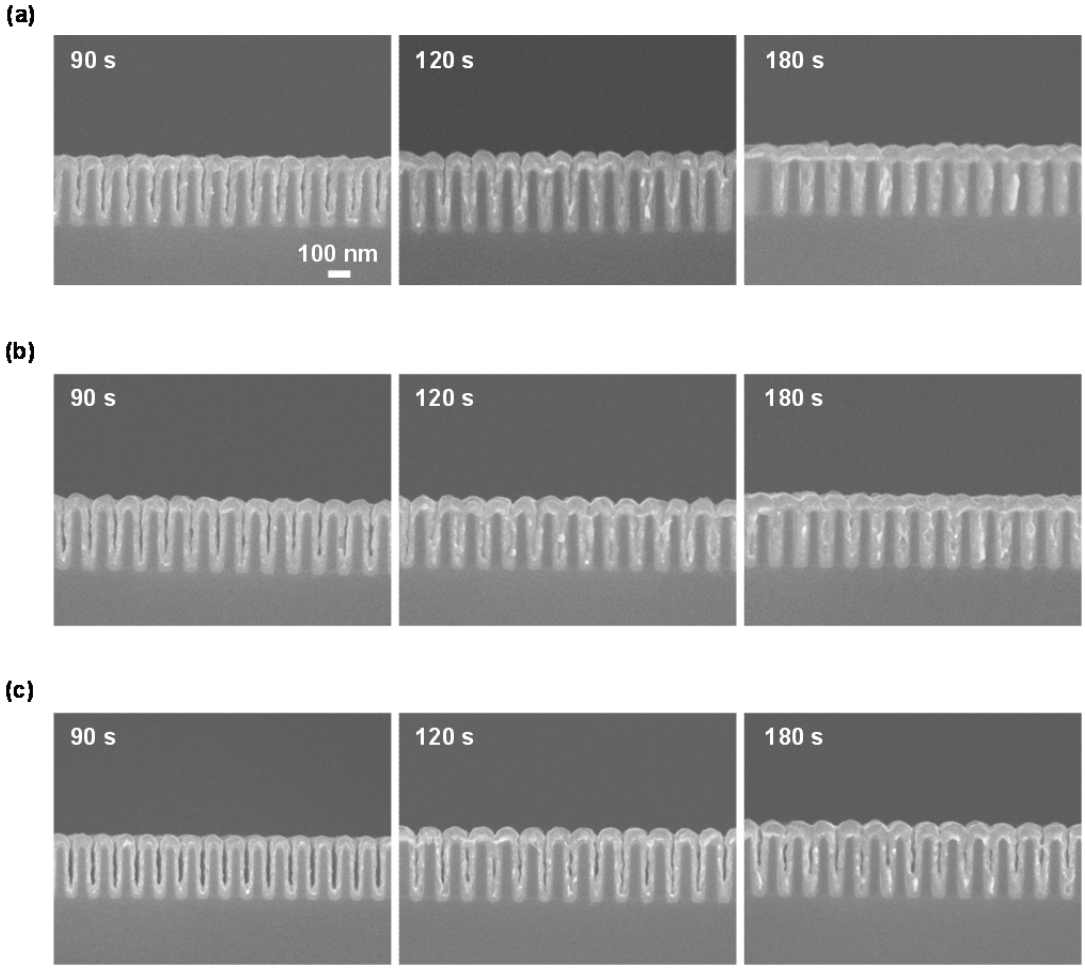

Figure 4. 12. Filling profiles according to the concentration of PEG8000, (a) 36 mg/L, (b) 72 mg/L, and (c) 144 mg/L.

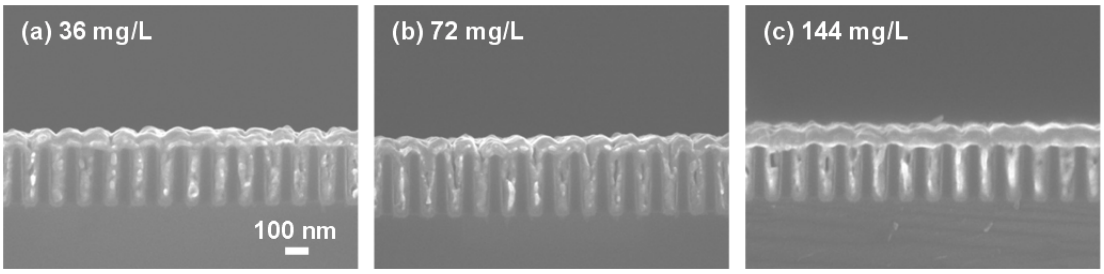

Figure 4. 13. Filling profiles according to the concentration of PEG100000. The deposition time was 3 min for (a) and (b), and 5 min for (c).

4.2. Combination of 2,2'-dipyridyl and DPS

4.2.1. Adsorption behavior of 2,2'-dipyridyl

The addition of 2,2'-dipyridyl to the ELD bath improves the physical properties of Cu deposits, such as the ductility and surface smoothness.[67] Furthermore, it is also effective on the stabilization of the bath. Figure 4.14 shows the suppression effect of 2,2'-dipyridyl. The addition of 2,2'-dipyridyl at 200 s shifted the OCP value to the negative direction, and the degree of the shift mounted with increasing the concentration of 2,2'-dipyridyl. It reflected that the adsorption 2,2'-dipyridyl reduced OCP during Cu ELD. The mass increase was retarded with the adsorption, as shown in Figure 4.14 (b). The reduction of the deposition rate occurred right after the injection, and the deposition rate was then stabilized in 10 s. It indicated that the adsorption of 2,2'-dipyridyl on the surface was fast. The degree of the reduction in the OCP and deposition rate became saturated at the high concentration of 2,2'-dipyridyl because the adsorption sites for the additive were limited on the surface. The deposition rate, which was originally ca. 0.52 μg/s, was reduced down to ca. 0.13 μg/s by the addition of 400 mg/L 2,2'-dipyridyl.

Figure 4.15 is the change of the deposition rate according to the concentration of 2,2'-dipyridyl in the immersion process without electrochemical measurement. The similar trend was observed as Figure 4.13 except the 3 mg/L of 2,2'-dipyridyl addition which accelerated the deposition rate slightly.

4.2.2. Adsorption behavior of DPS

The effect of DPS addition was shown in Figure 4.16 and Figure 4.17. The low concentration of DPS was reported to accelerate the deposition rate in Cu ELD and it was confirmed again in the measurement.[75] The deposition was accelerated with the addition of DPS below 1 mg/L, as depicted in Figure 4.16 (b). In this range, the OCP was also decreased as DPS adsorbed on the surface. The OCP was stabilized after 80 s from the addition, which was much longer time than 10 s of 2,2'-dipyridyl case. In this period, the temporary decrease in the deposition rate was observed in Figure 4.16 (b) inset. However, it was soon recovered and even accelerated up to 0.66 μg/s (1 mg/L DPS). It was supposed that DPS required the induction time to be activated for the acceleration. It was not sure, however, it was suspected that DPS changed its form to another on Cu surface during the induction time, which facilitated the acceleration of the deposition. At the higher concentration than 2 mg/L, the OCP decreased fast, but it began to increase again. At 4 mg/L of DPS, the OCP increase was found to stop when it reached ca. -0.66 V. The deposition was also strongly suppressed at those conditions. The deposition rate was reduced to 0.58×10^{-2} μg/s at 2 mg/L and 0.10×10^{-2} μg/s at 4 mg/L, respectively. The initial OCP decrease after the addition of DPS stood for the DPS adsorption, however, the latter OCP increase seemed to show another part of the DPS adsorption. It was reported that DPS changed its form by tautomerization at high concentration, causing the suppression of Cu ED.[112] In the

same way, the OCP increase at the high concentration in ELD might be also attributed to the tautomerization of DPS on the surface, which suppressed Cu ELD.

4.2.3. Synergetic effect of 2,2'-dipyridyl and DPS

When 2,2'-dipyridyl and DPS were added together, the suppression effect of DPS appeared at the lower concentration than 1 mg/L. Figure 4.18 (a) and (b) show the OCP and mass change of the electrode after the addition of both additives at once. With the addition, the OCP immediately decreased, and the deposition rate also decreased to 0.16 μg/s in 10 s from the injection time, regardless of DPS concentration. This fast decrease in the deposition rate was mainly due to the fast adsorption of 2,2'-dipyridyl rather than that of DPS. The concentration of 2,2'-dipyridyl was relatively higher than DPS, thus, the adsorption of 2.2'-dipyridyl was dominant in the initial stage. The DPS adsorption was clearly observed after 10 s from the injection time. With the adsorption of DPS, the deposition rate was additionally decreased from 0.16 μg/s to 1.10 x 10^{-2} μg/s even the concentration was lower than 1 mg/L, as shown in Figure 4.18 (b) inset. The value of 0.10 x 10^{-2} μg/s was the deposition rate at 4 mg/L of DPS in Figure 4.16, and the deposition rate was saturated at this value regardless of the DPS concentration. The OCP increase was also observed when the deposition was suppressed, indicating that the similar suppression occurred with the case that DPS was used alone. It demonstrated that the inhibition effect of DPS was enhanced with the addition of 2,2'-dipyridyl. The inhibition speed

became fast with the concentration of DPS: the time that the OCP started to increase was reduced, and the decrease in the deposition rate became fast. It was assumed that DPS adsorbed slowly and accumulated on the surface with 2,2'-dipyridyl. The saturation of the deposition rate independent of the DPS concentration supported the assumption. The acceleration effect was not observed in the concentration range of 0.5 mg/L ~ 2 mg/L DPS in the presence of 100 mg/L 2,2'-dipyridyl.

2,2'-dipyridyl and DPS were added in order, to confirm that the combination of 2,2'-dipyridyl and DPS enhanced the suppression effect. Additives were added at (1) 200 s and (2) 300 s as shown in Figure 4.19. In both cases, OCP was decreased with the first addition. The OCP behavior was also similar with each other after the second addition irrespective of whether the additive was 2,2'-dipyridyl or DPS. The second addition caused the decrease and re-increase in the OCP, indicating that Cu ELD was strongly suppressed by DPS. Changes in the deposition rate by the addition were shown in Figure 4.19 (b) inset. When 2,2'-dipyridyl was added first, the deposition rate was decreased as expected. Then the additional injection of DPS led to the further decrease in the deposition rate to 0.10×10^{-2} μg/s. On the contrary, the first addition of DPS accelerated the deposition rate up to 0.61 μg/s at 300 s. However, the injection of 2,2'-dipyridyl at 300 s quickly reduced the deposition rate to 0.10×10^{-2} μg/s. The acceleration effect of DPS was thoroughly eliminated by the addition of 2,2'-dipyridyl. The independence of the final deposition rate without reference to the addition order demonstrated that the adsorption of 2,2'-dipyridyl and DPS were not separative, but interdependent. It could be concluded that the

enhancement of the suppression effect was originated from the interaction between 2,2'-dipyridyl and DPS during Cu ELD.

4.2.4. Gap-filling of sub-60 nm trenches

The electroless filling of sub-60 nm trenches was performed with the additives. Figure 4.20 shows the filling profile according to the DPS concentration without 2,2'-dipyridyl. The concentration range of DPS was set as 4 mg/L ~ 16 mg/L, which were higher values than the DPS concentration used in the electrochemical analysis, considering the surface area of the substrate. It was reported that the filling of 500-nm trenches was achieved by only DPS.[75] However, voids were observed inside of sub-60 nm trenches in all cases conducted in this study. It was supposed that the filling with DPS only was not sufficient to induce the bottom-up filling on sub-60 nm trenches. As shown in Figure 4.16, DPS was found to require the induction time for the acceleration of ELD. The induction time might be too long for the filling of such narrow trenches to obtain the acceleration effect at the bottom. Furthermore, the concentration gradient of DPS inside of trenches might be relatively small compared to large trenches, leading to the inefficient suppression at the top and the acceleration at the bottom. The increase in the DPS concentration dramatically suppressed the deposition. However, the further increase in DPS concentration to reinforce the suppression effect resulted in the irregular deposition as shown in Figure 4.20 (d).

1200 mg/L of 2,2'-dipyridyl was then added with DPS in Figure 4.21 to enhance the suppression effect. 4 mg/L of DPS in Figure 4.21 (a) still showed voids inside of trenches. It seemed that 4 mg/L of DPS was insufficient to suppressed the deposition at the top of the trenches. The bottom-up filling profile was obtained without any voids when DPS concentration was 12 mg/L. (Figure 4.21 (c)) It was assumed that the fast adsorption of 2,2'-dipyridyl reduced the deposition rate at the initial stage of the deposition. Then DPS slowly adsorbed on the trench surface with the adsorption speed proportional to the concentration gradient, which was established inside of trenches due to the diffusion and consumption of DPS. As the decrease in the deposition rate was proportional to the DPS concentration, the bottom of the trenches was suppressed lastly, leading to the successful bottom-up filling. Over 16 mg/L, the deposition was strongly suppressed due to excessive DPS concentration.

Figure 4.22 and Figure 4.23 show filling profiles and the change in the thickness ratio according to the deposition time when 2,2'-dipyridyl and DPS was 1200 mg/L and 12 mg/L, respectively. It was clearly observed that Cu was deposited from the bottom of the trenches. The bumps were not formed because the acceleration effect of DPS was not observed in the presence of 2,2'-dipyridyl.

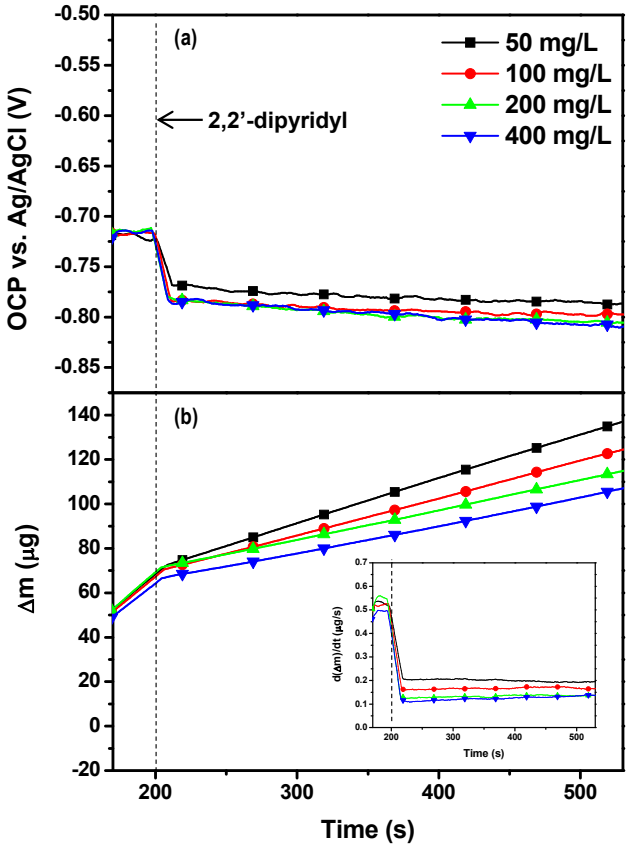

Figure 4. 14. (a) OCP and (b) mass change of electrodes in Cu ELD solution with 2,2'-dipyridyl concentration. 2,2'-dipyridyl was added at 200 s. (inset: d(Δm)/dt with time)

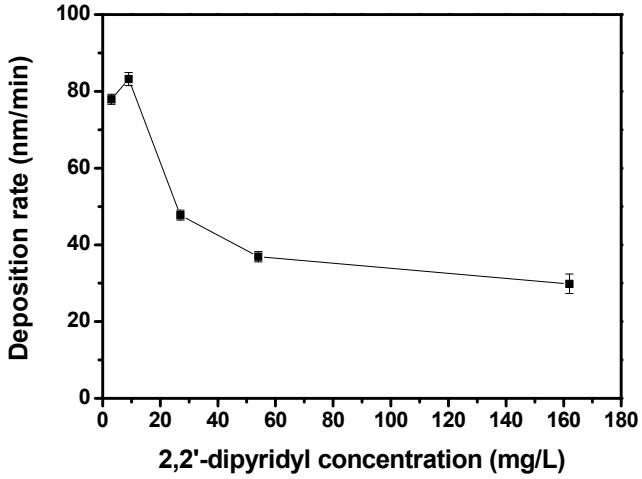

Figure 4. 15. The change of the deposition rate according to the concentration of 2,2'-dipyridyl.

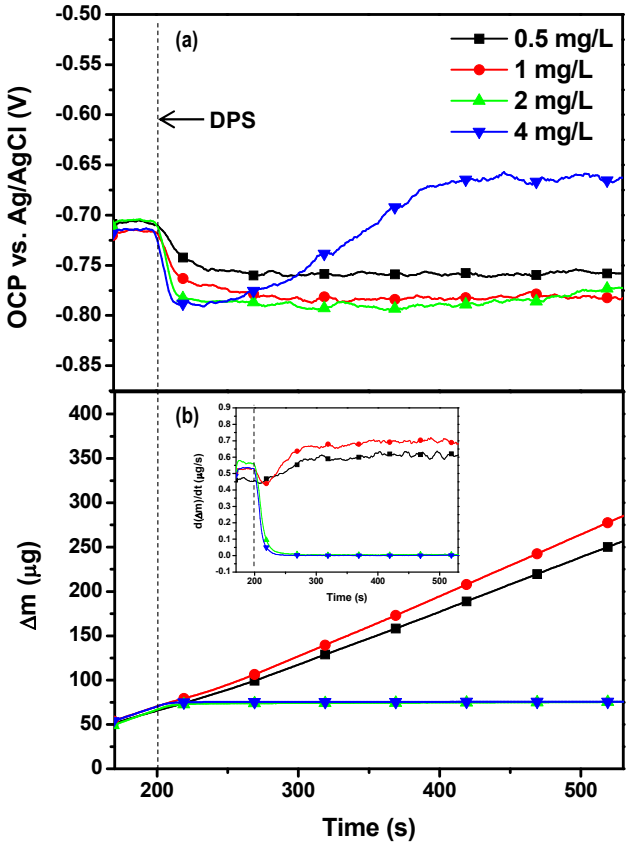

Figure 4. 16. (a) OCP and (b) mass change of electrodes in Cu ELD solution with DPS concentration. DPS was added at 200 s. (inset: d(Δm)/dt with time)

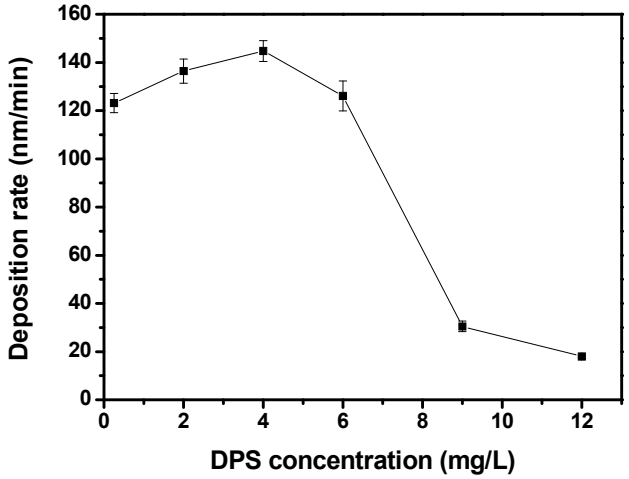

Figure 4. 17. The change of the deposition rate according to the concentration of DPS.

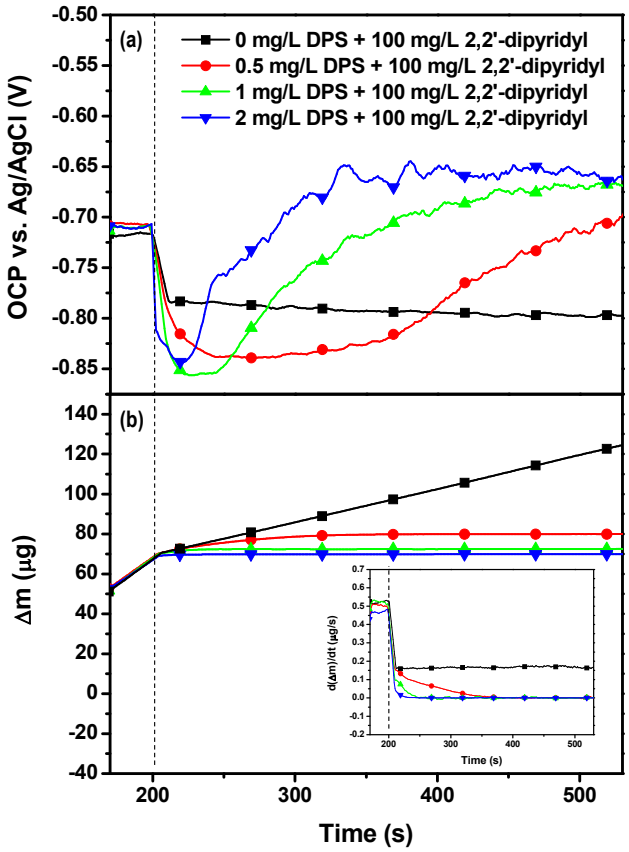

Figure 4. 18. (a) OCP and (b) mass change of electrodes in Cu ELD solution with DPS concentration in the presence of 100 mg/L 2,2'-dipyridyl. Both DPS and 2,2'-dipyridyl were added at 200 s. (inset: d(Δm)/dt with time)

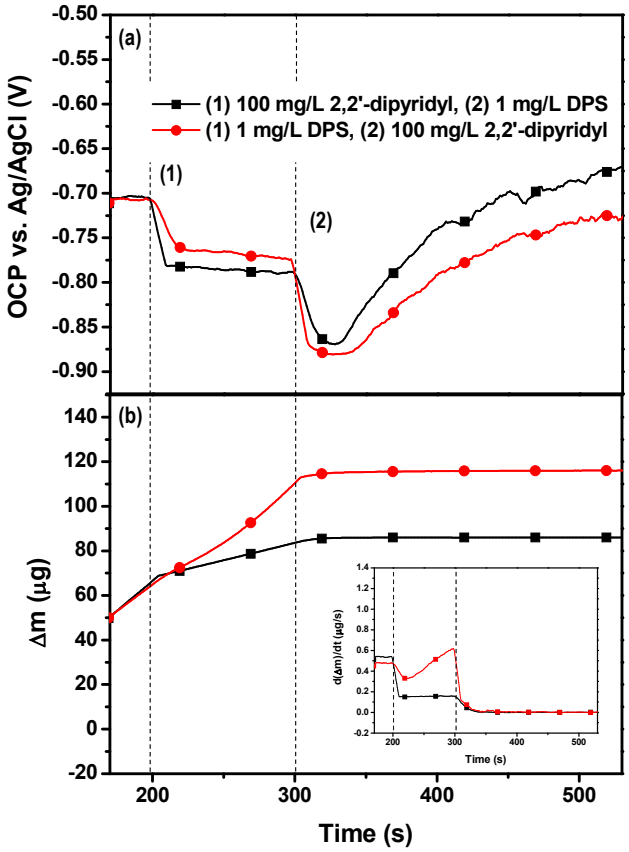

Figure 4. 19. (a) OCP and (b) mass change of electrodes in Cu ELD solution according to the order of the additive injection. Additives were added at (1) 200 s and (2) 300 s. (inset: d(Δm)/dt with time)

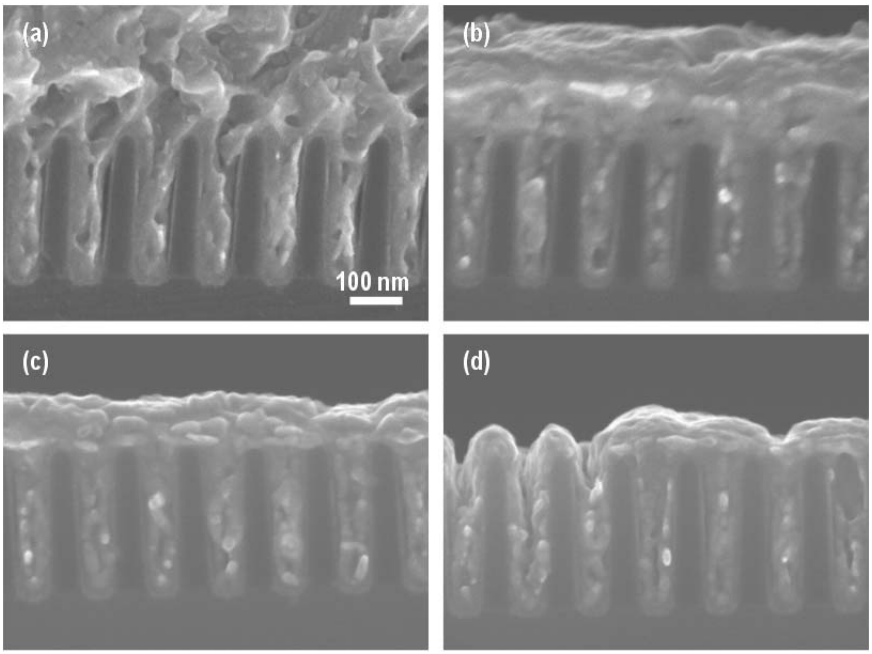

Figure 4. 20. Electroless Cu filling profiles according to (a) 4 mg/L, (b) 8 mg/L, (c) 12 mg/L, and (d) 16 mg/L of DPS without 2,2'-dipyridyl. The deposition time was 7 min.

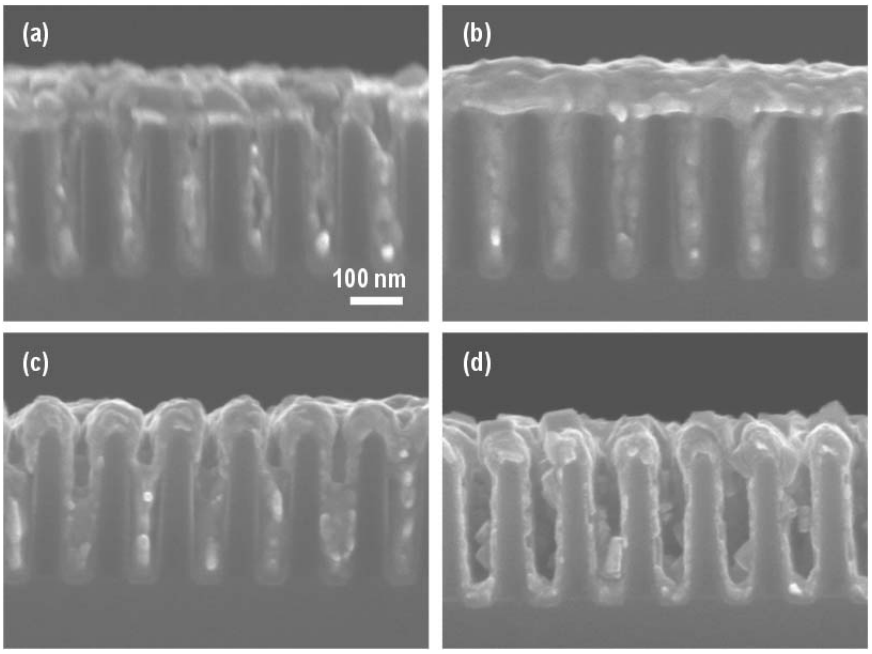

Figure 4. 21. Electroless Cu filling profiles according to (a) 4 mg/L, (b) 8 mg/L, (c) 12 mg/L, and (d) 16 mg/L of DPS with 1200 mg/L of 2,2'-dipyridyl. The deposition time was 7 min.

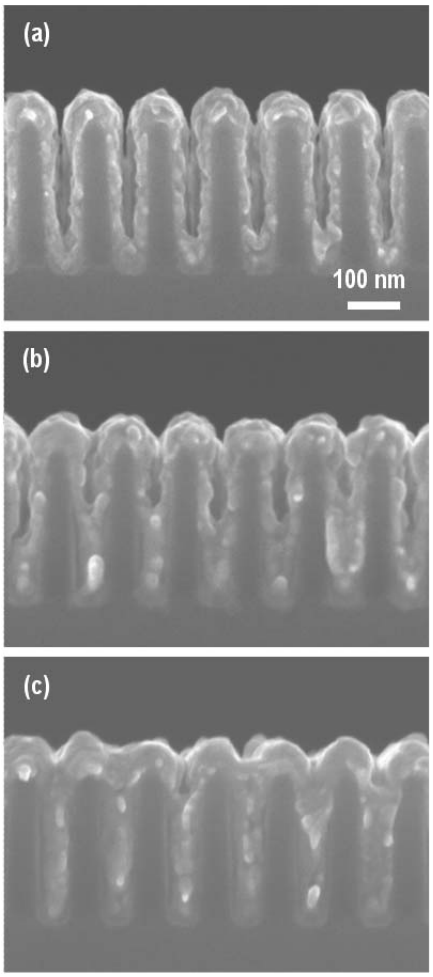

Figure 4. 22. Electroless Cu filling profiles with 1200 mg/L of 2,2'-dipyridyl and 12 mg/L DPS, (a) 2 min, (b) 4 min, and (c) 8 min.

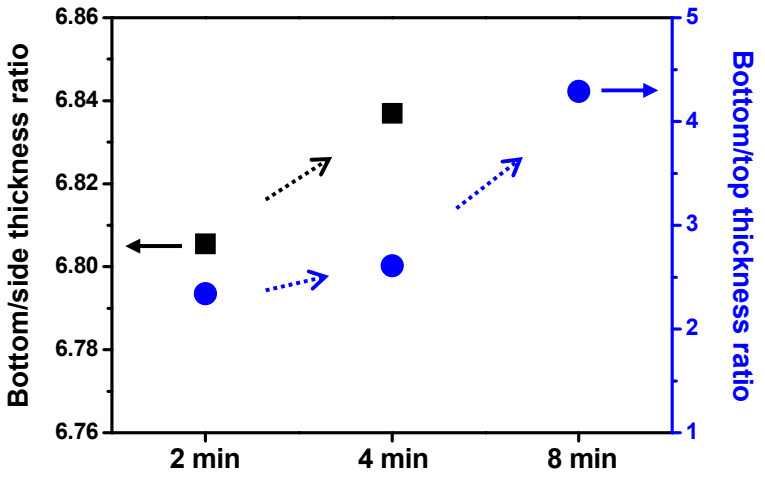

Figure 4. 23. The bottom/side and bottom/top thickness ratio according to the deposition time.

4.3. Summary

The adsorption of PEG during Cu ELD was investigated by the OCP measurement with QCM. The adsorption of PEG suppressed the deposition by blocking the active sites for HCHO adsorption. The adsorption kinetics of PEG was controlled by the diffusion as well as adsorption. PEG1500, which had the comparatively high diffusion coefficient, showed the adsorption-controlled kinetics at high concentration. However, PEG8000 and PEG100000 followed rather the diffusion-controlled kinetics because their diffusion coefficients were small. The effect of PEG with different molecular weight was compared at the same molar concentration as well as the same monomer concentration. The adsorption speed of PEG was largely dependent on the molar concentration while its suppression effect was considerably affected by the molecular weight. The suppression effect became stronger with increasing the molecular weight of PEG due to the steric hindrance of the molecules. Using the diffusion-controlled kinetics of PEG adsorption, the filling of sub-60 nm trenches was tried. However, the filling was failed due to the weak suppression of PEG at the top of the trenches.

The effects of 2,2'-dipyridyl and DPS on Cu ELD were also investigated. The adsorption of 2,2'-dipyridyl reduced the deposition rate fast, and the degree of the reduction was increased with its concentration. DPS was found to act as both an accelerator and suppressor, depending on its concentration. At the high concentration of DPS, the deposition was inhibited, and it was assumed to be related with the tautomerization of DPS. The suppression effect was enhanced by

the addition of 2,2'-dipyridyl with DPS. With 2,2'-dipyridyl, the addition of a trace of DPS could inhibit the deposition. The suppression became stronger as DPS adsorbed on the surface, and the speed of DPS adsorption was increased with increasing DPS concentration. Using those properties, the filling of sub-60 nm trenches was performed. The filling with single DPS was not successful, however, the filling with both 2,2'-dipyridyl and DPS achieved the bottom-up filling. The combination of 2,2'-dipyridyl and DPS effectively inhibited the deposition at the top of the trenches.

V. Conclusion

In this research, the mechanism of Cu ELD was investigated using the OCP measurement assisted by QCM for the application to the metallization in Cu damascene process. The OCP measurement with QCM realized the real-time observation of the adsorption behaviors of both reactants and additives during Cu ELD. The study was divided into two sections, 1) the investigation of basic Cu ELD mechanism and 2) the observation of additive adsorption during the deposition.

1. In the investigation of basic Cu ELD mechanism, the role of each chemical component in Cu ELD bath was investigated individually. It was observed that Cu surface in alkaline solution was continuously oxidized by dissolved oxygen, forming Cu_2O. However, when EDTA was introduced into the alkaline bath, the oxide formed in the solution was continuously dissolved out by the complexation with EDTA at the same time. Both the formation and dissolution of Cu oxide were stopped by the addition of HCHO into the bath, which indicated that the adsorption of HCHO on the surface inhibit the further oxidation and dissolution. From those results, it could be concluded that the presence of EDTA and HCHO in the ELD bath kept the Cu surface from the oxidation during Cu ELD. The real Cu ELD was also performed during the electrochemical measurement, and the induction period was observed on the Cu surface in the initial stage of the deposition. During the period, the deposition rate was found to be lower than

that after the period. The induction period observed at the initial stage of Cu ELD was strongly related with the adsorption and activation of HCHO.

The existence of pre-formed Cu oxides on the surface affected the deposition even EDTA removed Cu oxides from the surface. It was observed that HCHO rarely adsorbed on the oxidized surface in the absence of EDTA. The adsorption occurred with EDTA because EDTA removed the oxides at the initial stage of the immersion and helped the adsorption of HCHO. The same procedure was also observed in the full ELD solution; the deposition took place concurrently with the oxide removal. Although the deposition occurred on the surface whether the oxides were formed or not, the surface morphology was largely affected by the pre-formed oxides. The large amount of oxides resulted in the high surface roughness with many protrusions due to the irregular adsorption of HCHO while EDTA removed the oxides.

2. The adsorption of PEG during Cu ELD was investigated first. It was found that PEG gradually adsorbed on the surface during Cu ELD, reaching the saturation coverage. The deposition rate was also suppressed as PEG adsorbed. The adsorption speed of PEG was affected by the concentration of PEG, while the suppression effect after the saturation was not. The adsorption of PEG during the deposition followed Langmuir adsorption. The simulation of PEG adsorption revealed that the adsorption kinetics depended on the diffusion coefficient of PEG. PEG1500, which has the relatively high diffusion coefficient, showed the kinetic-controlled adsorption. However, PEG8000 and PEG100000 followed the diffusion-controlled

adsorption due to their low diffusion coefficients. The effect of the molecular weight of PEG was also observed at the same molar concentration and at the same monomer concentration. The adsorption speed of PEG100000 was the fastest at the same molar concentration, while it was the slowest at the same monomer concentration. It was suspected that the number of molecules and the saturation coverage were important factors affecting the adsorption speed. The suppression effect of PEG100000 was the strongest in both conditions, resulting from its large steric hindrance. The electroless filling of sub-60 nm trenches was tried with PEG, however, it was failed due to its ineffective suppression at the top of trenches.

The adsorption behaviors of 2,2'-dipyridyl and DPS were also investigated. The addition of 2,2'-dipyridyl into the ELD bath reduced the deposition rate, whereas the addition of DPS showed both acceleration and suppression effects according to its concentration. When both two additives were used together, the suppression effect of the deposition was enhanced. The addition of the small amount of DPS to the bath containing 2,2'-dipyridyl reduced the deposition rate further even its concentration range was in the acceleration region when it was used alone. In that case, the adsorption of 2,2'-dipyridyl was dominant at the initial stage due to its larger concentration than DPS. The additional suppression by the DPS adsorption was clearly observed after the adsorption of 2,2'-dipyridyl. Using the enhanced suppression effect, the bottom-up filling of sub-60 nm trenches was successfully achieved.

References

1. J. D. Meindl, J. A. Davis, P. Zaresh-Ha, C. S. Patel, K. P. Martin, and P. K. Kohl, *IBM J. Res. Dev.*, **46**, 245 (2002).

2. R. L. M. Dang and N. Shigyo, *IEEE Electr. Device L.*, **2**, 196 (1981).

3. S. Bothra, B. Rogers, and C. M. Osburn, *IEEE T. Electron Dev.*, **40**, 591 (1993).

4. The National Technology Roadmap for Semiconductors, *1997 Edition*, Semiconductor Industry Association (1997).

5. Interconnect, *ITRS roadmap (on-line document), 2011 edition*, International Technology Roadmap for Semiconductors (2011).

6. S. P. Muraka, *Mat. Sci. and Eng. R.*, **19**, 87 (1997).

7. J. R. Black, *IEEE T. Electron Dev.*, **ED-16**, 338 (1969).

8. S. Venkatesan, A. V. Gelatos, V. Misra, B. Smith, R. Islam, J. Cope, B. Wilson, D. Tuttle, R. Cardwell, S. Anderson, M. Angyal, R. Bajaj, C. Capasso, P. Crabtree, S. Das, J. Farkas, S. Filipiak, B. Fiordalice, M. Freeman, P. V. Gilbert, M. Herrick, A. Jain, H. Kawasaki, C. King, J. Klein, T. Lii, K. Reid, T. Saaranen, C. Simpson, T. Sparks, P. Tsui, R. Venkatraman, D. Watts, E. J. Weitzman, R. Woodruff, I. Yang, N. Bhat, G. Hamilton, and Y.Yu, *IEDM Tech. Dig.*, 769 (1997).

9. R. C. Jaeger, *Introduction to Microelectronic Fabrication*, 2nd Edition, Prentice Hall, New

Jersey, USA (2002).

10. C.-C. Yu, *Damascene Process*, US Patent, 61,976,78 B1 (2001).

11. D. M. Mattox, *Handbook of Physical Vapor Deposition (PVD) processing*, Noyes Publications, New Jersey, USA (1998).

12. M. Proust, F. Judong, J.M. Gilet, L. Liauzu, and R. Madar, *Microelectron. Eng.*, **55**, 269 (2001).

13. H. O. Pierson, *Handbook of Chemical Vapor Deposition*, William Andrew, New Mexico, USA (1999).

14. E. S. Hwang and J. Lee, *Electrochem. Solid-State Lett.*, **3**, 138 (2000).

15. D. Josell, D. Wheeler, and T. P. Moffat, *Electrochem. Solid-State Lett.*, **5**, C44 (2002).

16. M. Paunovic and M. Schlesinger, *Fundamentals of Electrochemical Deposition*, 2nd Edition, John Wiley & Sons, Inc., New Jersey, USA (2006).

17. S.-K. Kim and J. J. Kim, *Electrochem. Solid-State Lett.*, **7**, C98 (2004).

18. T. P. Moffat, D. Wheeler, W. H. Huber, and D. Josell, *Electrochem. Solid-State Lett.*, **4**, C26 (2001).

19. D. Josell, D. Wheeler, W. H. Huber, J. E. Bonevich, and T. P. Moffat, J. Electrochem. Soc., 148, C767 (2001).

20. T. P. Moffat, D. Wheeler, S.-K. Kim, and D. Josell, *J. Electrochem. Soc.*, **153**, C127 (2006).

21. A. Radisic, Y. Cao, P. Taephaisitphongse, A. C. West, and P. C. Searson, *J. Electrochem. Soc.*, **150**, C362 (2003).

22. S. Schaltin, L. D'Urzo, Q. Zhao, A. Vantomme, H. Plank, G. Kothleitner, C. Gspan, K. Binnemans, and J. Fransaer, *Phys. Chem. Chem. Phys.*, **14**, 13624 (2012).

23. V. E. G. Leuze and B. Saulgau, *Electroplating and Electroless Plating of Copper & its Alloys*, N. Kanani ed., Finishing Publications Ltd., Herts, UK (2003).

24. J. Reid, Jpn. *J. Appl. Phys.*, **40**, 2650 (2001).

25. N. M. Martyak and P. Ricou, *Mater. Sci. Semi. Proc.*, **6**, 225 (2003).

26. J. H. Sukamto, E. Webb, T. Andryushchenko, and J. Reid, *J. Appl. Electrochem.*, **34**, 283 (2004).

27. T. Karabacak and T.-M. Lu, *J. Appl. Phys.*, **97**, 124504 (2005).

28. S. M. Rossnagel, *J. Vac. Sci. Technol. B*, **16**, 2585 (1998).

29. J. A. Thornton, *J. Vac. Sci. Technol. A*, **4**, 3059 (1986).

30. Z. Li, A. Rahtu, and R. G. Gordon, *J. Electrochem. Soc.*, **153**, C787 (2006).

31. T. Au, Q. M. Wang, H. Li, J.-S. M. Lehn, D. V. Shenai, and R. G. Gordon, *J. Electrochem. Soc.*, **159**, D382 (2012).

32. C. H. Lee, S. Hwang, S.-C. Kim, and J. J. Kim, *Electrochem. Solid-State Lett.*, **9**, C157 (2006).

33. T. Smy, L. Tan, S. K. Dew, M. J. Brett, Y. Shacham-Diamand, and M. Desilva, *J. Electrochem. Soc.*, **144**, 2115 (1997).

34. H. T. Ng, S. F. Y. Li, L. Chan, F. C. Loh, and K. L. Tan, *J. Electrochem. Soc.*, **145**, 3301 (1998).

35. S. K. Cho, T. Lim, H.-K. Lee, and J. J. Kim, *J. Electrochem. Soc.*, **157**, D187 (2010).

36. T. Andryuschenko and J. Reid, in IEEE International Interconnect Conference 2001, IEEE, p. 33 (2000).

37. H. Kim, J. Vac. Sci. Technol. B, 21, 2231 (2003).

38. A. E. Kaloyeros and E. Eisenbraun, *Annu. Rev. Mater. Res.*, **30**, 363 (2000).

39. D. Josell, D. Wheeler, C. Witt, and T. P. Moffat, *Electrochem. Solid-State Lett.*, **6**, C143 (2003).

40. T. P. Moffat, M. Walker, P. J. Chen, J. E. Bonevich, W. E. Egelhoff, L. Richter, C. Witt, T. Aaltonen, M. Ritala, M. Leskela, and D. Josell, *J. Electrochem. Soc.*, **153**, C37 (2006).

41. S. K. Cho, S.-K. Kim, H. Han, J. J. Kim, and S. M. Oh, *J. Vac. Sci. Technol. B*, **22**, 2649 (2004).

42. R. Chan, T. N. Arunagiri, Y. Zhang, O. Chyan, R. M. Wallace, M. J. Kim, and T. Q. Hurd, *Electrochem. Solid-State Lett.*, **7**, G154 (2004).

43. T. N. Arunagiri, Y. Zhang, O. Chyan, M. El-Bouanani, M. J. Kim, K. H. Chen, C. T. Wu, and

L. C. Chen, *Appl. Phys. Lett.*, **86**, 083104 (2005).

44. P. Fricoteaux and J. Douglade, *Surf. Coat. Tech.*, **184**, 63 (2004).

45. M. Damayanti, T. Sritharan, S. G. Mhaisalkar, and Z. H. Gan, *Appl. Phys. Lett.*, **88**, 044101 (2006).

46. J.-B. Yeh, D.-C. Perng, and K.-C. Hsu, *J. Electrochem. Soc.*, **157**, H810 (2010).

47. H. Shimizu, K. Sakoda, and Y. Shimogaki, *Microelectron. Eng.*, *in press* (2012), http://dx.doi.org/10.1016/j.mee.2012.08.008

48. Q. Chen, X. Lin, C. Valvede, V. Paneccasio, R. Hurtubise, P. Ye, E. Kudrak, and J. Abys, *ECS trans.*, **6**, 179 (2007).

49. I. Ohno, O. Wakabayashi, and S. Haruyama, *J. Electrochem. Soc.*, **132**, 2323 (1985).

50. A. Brenner and G. Riddell, *J. Res. Nat. Bur. Standards*, **37**, 31 (1946).

51. M. Saito, *J. Met. Finish. Soc. Jpn.*, **17**, 14 (1966).

52. M. Paunovic, *Plating*, **55**, 1161 (1968).

53. *Advances in Electrochemical Science and Engineering Volume 3*, H. Gericher, R. C. Alkire, and D. M. Kolb ed., Vch Verlagsgesellschaft mbH, Weinheim, Germany (1993).

54. R. Sard, *J. Electrochem. Soc.*, **117**, 865 (1970).

55. S. Y. Chang, C. W. Lin, H. H. Hsu, J. H. Fang, and S. J. Lin, *J. Electrochem. Soc.*, **151**, C81 (2004).

56. T. Osaka and H. Takematsu, *J. Electrochem. Soc.*, **127**, 1021 (1980).

57. Ying-Chao Sung, Chin-Han Lai, Su-Jien Lin, and Sou-Yi Chang, *Electorochem. Solid-State Lett.*, **9**, C85 (2006).

58. Xiaomin Wu and Wei Sha, *Appl. Surf. Sci.*, **255**, 4249 (2009).

59. J. P. Marton and M. Schlesinger, *J. Electrochem. Soc.*, **115**, 16 (1968).

60. M. Paunovic, *J. Electrochem. Soc.*, **124**, 349 (1977).

61. A. Molenaar, M. F. E. Holdrinet, and L. K. H. Van Beek, *Plating*, **61**, 238 (1974).

62. Y. Shacham-Diamand and V. M. Dubin, *Microelectron. Eng.*, **33**, 47 (1997).

63. Z. Jusys, G. Stalnionis, E. Juzeliūnas and A. Vaškelis, *Electrochim. Acta*, **43**, 301 (1998).

64. S. Nakahara and Y. Okinaka, *Acta Metall.*, **31**, 713 (1983).

65. P. Bindra and J. Roldan, *J.Electrochem.Soc.*, **132**, 2581 (1985).

66. F. Hanna, Z. A. Hamid, and A. A. Aal, *Mater. Lett.*, **58**, 104 (2003).

67. M. Oita, M. Matsuoka, and C. Iwakura, *Electrochim. Acta*, **42**, 1435 (1997).

68. H.-C. Koo and J. J. Kim, *J. Electrochem. Soc.*, **155**, D176 (2008).

69. A. Hung, *J. Electrochem. Soc.*, **132**, 1047 (1985).

70. H. Zhang, X. Zou, and J. Sun, *J. Compos. Mater.*, **0**, 1 (2012).

71. Z. Wang, O. Yaegashi, H. Sakaue, T. Takahagi, and S. Shingubara, *J. Electrochem. Soc.*, **151**, C781 (2004).

72. S. Shingubara, Z. Wang, O. Yaegashi, R. Obata, H.i Sakaue, and T. Takahagi, *Electrochem. Solid-State Lett.*, **7**, C78 (2004).

73. M. Hasegawa, N. Yamachika, Y. Shacham-Diamand, Y. Okinaka, and T. Osaka, *Appl. Phys. Lett.*, **90**, 101916 (2007).

74. C. H. Lee, S. C. Lee, and J. J. Kim, *Electrochim. Acta*, **50**, 3563 (2005).

75. C. H. Lee, S. K. Cho, and J. J. Kim, *Electrochem. Solid-State Lett.*, **8**, J27 (2005).

76. C. H. Lee, A. R. Kim, H.-C. Koo, and J. J. Kim, *J. Electrochem. Soc.*, **156**, D207 (2009).

77. M. Hasegawa, Y. Okinaka, Y. Shacham-Diamand, and T. Osaka, *Electrochem. Solid-State Lett.*, **9**, C138 (2006).

78. Z. Yang, X. Wang, N. Li, Z. Wang, and Z. Wang, *Electrochim. Acta*, **56**, 3317 (2011).

79. L. D. Burke, G. M. Burton, and J. A. Collins, *Electrochim. Acta*, **44**, 1467 (1998).

80. T. M. Tam, *J. Electrochem. Soc.*, **132**, 806 (1985).

81. P. Bindra and J. Roladan, *J. Appl. Electrochem.*, **17**, 1254 (1987).

82. M. Paunovic and R. Arndt, *J. Electrochem. Soc.*, **130**, 794 (1983).

83. J. Li, H. Hayden, and P. A. Kohl, *Electrochim. Acta*, **49**, 1789 (2004).

84. Z. Jusys and A. Vaškelis, *Electrochim. Acta*, **42**, 449 (1997).

85. B. J. Feldman and O. R. Melroy, *J. Electrochem. Soc.*, **136**, 640 (1989).

86. K. J. Park, H.-C. Koo, T. Lim, M. J. Kim, O. J. Kwon, and J. J. Kim, *J. Electrochem. Soc.*,

158, D541 (2011).

87. Y.-J. Oh and C.-H. Chung, *Thin Solid Films*, **515**, 2137 (2006).

88. Y.-M. Lin and S.-C. Yen, *Appl. Surf. Sci.*, **178**, 116 (2001).

89. T. Du, D. Tamboli, V. Desai, and S. Seal, *J. Electrochem. Soc.*, **151**, G230 (2004).

90. J. Flis and D. J. Duquette, J. Electrochem. Soc., **131**, 254 (1984).

91. S. Tamilmani, W. Huang, S. Raghaven, and R. Small, *J. Electrochem. Soc.*, **149**, G638 (2002).

92. Y. Feng, K.-S. Siow, W.-K. Teo, K.-L. Tan, and A.-K. Hsieh, *Corrosion*, **53**, 389 (1997).

93. Y. S. Chu, I. K. Robinson, and A. A. Gewirth, *J. Chem. Phys.*, **110**, 5952 (1999).

94. R. Pauliukaitė, G. Stalnionis, Z. Jusys, and A. Vaškelis, *J. Appl. Electrochem.*, **36**, 1261 (2006).

95. G. W. Hung and R. H. Dinius, *J. Chem. Eng. Data*, **17**, 449 (1972).

96. C. N. Fredd and H. S. Fogler, *SPE J.*, **3**, 34 (1998).

97. A. E. Martell and R. D. Hancock, *Metal Complexes in Aqueous Solutions*, Plenum Press, New York, USA (1996).

98. S. Lee and R. W. Staehle, *J. Electrochem. Soc.*, **142**, 2189 (1995).

99. H. Gil and C. Leygraf, *J. Electrochem. Soc.*, **154**, C272 (2007).

100. M. Finšgar, S. Peljhan, A. Kokalj, J. Kovač, and I. Milošev, *J. Electrochem. Soc.*, **157**,

C295 (2010).

101. P. Druska and H.-H. Strehblow, *Surf. Interface Anal.*, **23**, 440 (1995).

102. I. Milošev and H.-H Strehblow, *J. Electrochem. Soc.*, **150**, B517 (2003).

103. R. Schumacher, J. J. Pesek, and O. R. Melroy, *J. Phys. Chem.*, **89**, 4339 (1985).

104. S. Poulston, P. M. Parlett, P. Stone, and M. Bowker, *Surf. Interface Anal.*, **24**, 811 (1996).

105. J. Iijima, J.-W. Lim, S.-H. Hong, S. Suzuki, K. Mimura, and M. Isshiki, *Appl. Surf. Sci.*, **253**, 2825 (2006).

106. O. A. Demchenko and D. I. Belkin, *Kinet. Catal+*, **52**, 26 (2011).

107. A. M. Mota, M. L. S. Gonçalves, J. P. Farinha, and J. Buffle, *Colloid. Surface. A*, **90**, 271 (1994).

108. D. B. Hibbert, J. J. Gooding, and P. Erokhin, *Langmuir*, **18**, 1770 (2002).

109. C. Y. Chang, W. T. Tsai, C. H. Ing, and C. F. Chang, *J. Colllod. Interf. Sci.*, **260**, 273 (2003).

110. J. K. Armstrong, R. B. Wenby, H. J. Meiselman, and T. C. Fisher, *Biophys. J.*, **87**, 4259 (2004).

111. R. Akolkar and U. Landau, *J. Electrochem. Soc.*, **151**, C702 (2004).

112. S. K. Cho, S.-K. Kim, and J. J. Kim, *J. Electrochem. Soc.*, **152**, C330 (2005).

국문초록

반도체 공정은 구리 다마신 공정의 도입으로 기존의 배선 재료인 알루미늄을 구리로 전환하면서 혁신적인 발전을 이루었으며, 현재까지 집적도 증가와 적층 기술로 소자의 성능 향상을 도모하였다. 하지만 근래에 들어서 소자의 집적도 증가에 따른 구리 선폭의 감소가 야기하는 확산 방지층/구리 씨앗층 형성 문제로 인하여 차세대 반도체 소자 제작에 어려움을 겪고 있다. 이러한 문제점들을 해결하기 위하여 원자층 증착법, 무전해 도금 등 다양한 방법이 고안되고 있다. 특히 구리 무전해 도금은 확산 방지층 위 구리 씨앗층을 균일하게 형성할 수 있을 뿐 아니라, 원자층 증착 방법을 이용한 루테늄 합금 또는 코발트 합금 계열의 차세대 확산 방지층 위에서도 구리 박막 형성이 가능하여 차세대 구리 배선 방법으로 주목 받고 있다. 본 논문에서는 개회로전압 측정과 수정진동자저울을 통해 전극의 무게 변화를 측정함으로써 구리 무전해 도금을 실시간으로 관찰할 수 있는 방법을 개발하였으며, 이를 통해 구리 무전해 도금의 메커니즘과 구리 무전해 도금에 사용되는 첨가제의 역할을 연구하였다. 또한 60 nm 미만의 트렌치에서 구리 초등각 전착을 성공시켜, 차세대 구리 배선 방법으로의 구리 무전해 도금 적용 가능성을 확인하였다.

구리 무전해 도금 메커니즘 연구에서는 우선, 구리 무전해 도금 용액을 구성하는 요소가 구리 전극에 미치는 영향을 개별적으로 파악하였다. 구리 전극은 염기성 용액 내에서 지속적으로 산화되었다. 하지만 착화제인 에틸렌디아민산이 용액 내에 함께 존재하면, 용존 산소에 의하여 지속적으로 산화되는 구리 전극 표면의 산화물과 착화합물을 형성 · 용해시키는 것으로 나타났다. 환원제인 포름알데히드는 구리 전극 표면에 흡착하여 추가적인 전극의 산화를 억제하였다. 따라서 이러한 두 반응물은 구리 무전해 도금 시에 표면에 구리 산화막 형성을 억제하는 역할을 한다고 볼 수 있다. 또한 실제 구리 무전해 도금 시에 도금 초기에 관찰되는 유발 기간 동안에는 도금 속도가 유발 기간 이후의 도금 속도에 비해 낮은 것을 확인하였는데, 이는 포름알데히드의 흡착과 산화가 일어나기까지의 시간과 관련이 있는 것으로 나타났다. 이와 함께 구리 산화막이 구리 무전해 도금 박막에 미치는 영향도 연구하였다. 표면에 구리 산화막이 존재할 경우에, 에틸렌디아민산이 구리 산화막을 제거하기 전까지는 포름알데히드의 흡착이 원활하지 않은 것으로 나타났다. 이러한 현상은 실제 구리 박막에서도 동일하게 반영되었으며, 도금 전 구리 산화막이 많이 형성되어 있을수록 포름알데히드의 불균일한 흡착으로 인해 표면이 거칠어짐을 확인할 수 있었다.

구리 무전해 도금에 이용하는 대표적인 첨가제로, 억제제인 PEG와 안정제인 2,2'-dipyridyl, 가속제겸 억제제인 DPS의 영향을 연구하였다. 구리 무전해 도금 중 PEG는 점진적으로 구리 표면에 흡착하였으며, 흡착과 함께 도금 속도를 감소시켰다. PEG의 흡착으로 인한 도금 속도의 감소는 흡착한 PEG가 포름알데히드의 흡착을 방해하기 때문인 것으로 나타났다. 무전해 도금 중 PEG의 흡착 동특성은 PEG의 분자량과 직접적으로 연관이 있는 확산계수에 크게 영향을 받았다. 분자량이 작은 PEG는 흡착 지배 동특성을, 분자량이 큰 PEG는 확산 지배 동특성을 나타내는 것을 확인할 수 있었다. 뿐만 아니라 같은 몰농도, 같은 단량체 농도에서 PEG의 분자량에 따른 효과도 확인하였으며, PEG 분자량이 클수록 억제효과가 크게 나타났다. 2,2'-dipyridyl 과 DPS 또한 그 흡착 동향을 살펴보았으며, 2,2'-dipyridyl은 농도가 증가함에 따라 도금 속도를 감소시켰고, DPS는 농도에 따라 도금 속도를 가속시키거나 억제시켰다. 하지만 두 첨가제를 동시에 첨가하였을 경우에는 두 첨가제의 상호작용으로 인하여 도금 속도가 빠르게 억제됨을 확인할 수 있었다. 이러한 성질을 이용하여 60 nm 미만의 트렌치의 초등각 전착에 성공하였다.

주요어: 구리, 무전해 도금, 첨가제, 초등각 전착, 전착 메커니즘

학번: 2009-30249

Appendix I

Optimization of Catalyzing Process on Ta Substrate for Copper Electroless Deposition Using Electrochemical Method

An electrochemical monitoring method was introduced to optimize catalyzing process prior to Cu electroless deposition on a Ta/TaN barrier. It utilized the electro-oxidation of dimethylaminoborane on the Pd particles formed on the substrate after the catalyzing process. The anodic current of the dimethylaminoborane oxidation was only detected when Pd particles existed, and its peak current showed a linear dependency on the Pd particle density. It was also found that the oxidation on Pd particles was an irreversible process accompanying 3-electron transfer. Using the electrochemical method, the optimization of the catalyzing process was performed to maximize the number of Pd particles per unit area (1 cm^2). After the optimization, Cu electroless deposition was performed. A minimum 18-nm-thick Cu seed layer was successfully obtained and the adhesion strength was good enough to maintain the flaking-free film even after Cu electrodeposition.

1. Introduction

With the development of semiconductor devices, Cu has been employed in the metallization process as a conduction material instead of Al to reduce RC delay (resistance-capacitance delay) in signal transfer.[1] Electrodeposition (ED) is generally used to form Cu conduction lines, and it requires a Cu seed layer for the current path because ordinary diffusion barriers, such as Ta/TaN and TiN/Ti, are highly electrical-resistive. Conventional Cu seed layer formation is usually carried out via physical vapor deposition (PVD). However, as the size of the metal line has dwindled, depositing the thin layer uniformly throughout the vias and trenches has become very difficult due to the intrinsic directionality of PVD. The poor step-coverage thus introduces a lot of defects in Cu seed layer, leading to poor reliability of the Cu filling.[2, 3] In contrast with PVD, Cu electroless deposition (ELD) shows conformal deposition characteristics with relatively good step-coverage.[4] Therefore, Cu ELD has become a promising candidate for the deposition of Cu seed layers in the next semiconductor process.[5, 6]

The prerequisite of seed layer deposition by Cu ELD is to form catalysts on the diffusion barriers owing to their chemical inactivity. The catalyzing process is generally termed as surface activation, and Pd has been widely used as such a catalyst. To date, several surface activation methods have been reported in the literature including: one-step activation, two-step activation, and the deposition of Pd nanoparticles.[7-10] These processes determine the density and size distribution of Pd particles formed on the surface. They govern not only the minimum thickness for the formation of a continuous ELD film but also the adhesion strength between the film and substrate. At the initial stage of Cu ELD, Cu grows in three dimensions and covers Pd particles

preferentially as shown in Figure 1. This growth mode continues until Cu clusters coalesce and thus cover the entire surface, followed by subsequent two-dimensional growth (2D) normal to the surface.[11, 12] The time required to reach the 2D growth mode from the start of the three-dimensional (3D) growth is defined as the incubation time. This incubation time is an indicator of the completion of the continuous film, and is determined by the density and average size of Pd particles.[13]

For this reason, many efforts have been devoted to increasing the density of Pd particles. The density was generally measured from surface images by counting the Pd particles on a diffusion barrier. The method is still powerful in particle quantification so far, however, it has some limitations because it is sample-destructive and strongly depends on the resolution of images. Several methods have thus been suggested to complement the particle-counting method, which involves the electrochemical induction of hydrogen adsorption/desorption on Pd particles and the measurement of electroless deposition rate on Pd.[14-16] However, these methods still have their drawbacks. The hydrogen adsorption/desorption on Pd is not directly related to the chemical reactions in ELD, and the measurement of the deposition rate right on Pd is difficult because it occurs over a very short period of time.

In our study, another evaluation method was developed by using the electrochemical oxidation of a reducing agent, dimethylaminoborane (DMAB), which has been widely employed in Cu ELD. Even though the oxidation of reducing agents on Cu or Pd film has been investigated in many previous studies, using the electrochemical approach to estimate the Pd

particle density on an inactive diffusion barrier is still rare.[17, 18] This study focused on the relationship of DMAB oxidation with Pd particle density and the technical issues in the direct electrochemical analysis of Pd particles on a Ta/TaN barrier.

2. Experimental

The substrate used in the experiment was Ta (PVD, 7.5 nm)/TaN (PVD, 7.5 nm)/Si. It was cut into 1.5 cm × 1.5 -cm squares. Prior to the experiments, all substrates were ultrasonicated with isopropyl alcohol (IPA) for 1 min to remove organic contaminants and then rinsed in DI water.

The two-step activation was adapted in this work due to its relative ease to obtain various Pd particle densities while almost maintaining the size distribution. The schematic diagram of the two-step activation is depicted in Figure 2. Before the activation step, native Ta oxide was removed by the immersion in etching solution for 5 min. The solution used for Ta oxide etching was composed of 20 ml/L HF (48-51%) and 20 ml/L HNO_3 (60-62%). After the removal, the substrate was dipped into DI water three times for 10 s each. Sn sensitization was then performed in a solution consisting of 30 mM $SnCl_2$ and 40 - 100 ml/L HCl (35-37%) as the first step in the two-step activation. Following Sn sensitization, Pd activation was accomplished by immersing in a solution containing 0.6 mM $PdCl_2$ and 1.5 - 12 ml/L HCl. The concentration of HCl and the immersion time in both processes were varied to optimize the catalyzing process. The substrate was rinsed with DI water twice for 10 s each to remove any residual chemical

after Sn sensitization and Pd activation steps. Samples were dried through N_2 blowing after Pd activation. All of these processes were conducted at room temperature.

A linear sweep voltammetry (LSV) was performed on the as-prepared samples. During the electrochemical analysis, each substrate was loaded in the electrochemical cell and exposed to the electrolyte as a working electrode with an area of 1 cm^2. The other part of the substrate was completely sealed from the electrolyte. A saturated calomel electrode (SCE) and a Pt wire were used as a reference electrode and a counter electrode, respectively. The range of potential sweep was from -1.0 V to 0.3 V (vs. SCE) with a scan rate of 20 mV/s. The solution of 0.05 M DMAB was used as electrolyte. pH of the solution was adjusted to 13.5 by adding KOH. All electrochemical analysis was conducted at room temperature.

The catalyzing process was optimized in order to achieve the maximum Pd particle density by using the electrochemical method. Variables that can be optimized included the composition of solution and process time in each step. After optimization, Cu ELD was carried out on the substrate with a bath composition of 4 mM $CuSO_4 \cdot 5H_2O$, 8 mM EDTA, 14 mM p-HCHO, and 69 mM KOH. The deposition temperature was 70℃. For the adhesion test, Cu ED was also performed at room temperature by applying -200 mV (vs. open circuit potential) in the electrolyte made up of 0.25 M $CuSO_4 \cdot 5H_2O$, 1.0 M H_2SO_4, 88 μM polyethylene glycol (PEG-3400, Mw. 3400), 1 mM NaCl, and 50 μM SPS (bis(3-sulfopropyl)disulfide). The charge consumed in the deposition was 140 mC corresponding to the deposition thickness of around 100 nm.

Potentiostat 263A (EG&G) was applied in the electrochemical analysis. The sheet resistance of film was measured using a four-point probe (CMT-SR 1000N). The surface morphology was examined by a field emission scanning electron microscope (FE-SEM, JSM-6330F) and the number of Pd particles was counted from SEM images. In the SEM analysis, the Pd density and particle size were measured using at least three different spots on the same sample.

3. Electrochemical oxidation on Pd particles

LSV was characterized in KOH solution (pH 13.5) prior to the electrochemical analysis of DMAB oxidation. Figure 3 shows the linear voltammograms of substrates after each treatment step. No obvious difference in the curve shape was observed between Figure 3 (i) and (ii). It implies that the adsorbed Sn colloids had no influence on the shape of the current-potential curve in KOH solution. The small anodic current detected over -0.3 V from both samples was related to Ta oxidation during the potential sweep. Meanwhile, as shown in Figure 3 (iii), the cathodic current was measured on the Pd-activated surface below -0.1 V. It might have been attributed to the catalytically-induced hydrogen evolution occurring on Pd particles after activation.[19] It was also expected that the oxidation of Ta proceeded in the same manner on the Pd-activated substrate, but the cathodic current of hydrogen evolution might overlap the anodic current.

Even when 0.05 M of DMAB was added to the KOH solution, there was no distinguishable

change in current profiles of samples (i) before and (ii) after Sn sensitization as shown in Figure 4 (a). It indicated that the substrate and Sn colloids were also electrochemically-inactive on the oxidation of DMAB. The small anodic current contributed by the Ta oxidation was still observed in the both cases even when DMAB was present in the solution. However, in the case of the Pd-activated sample, a large anodic current was obviously detected instead of the cathodic current resulting from hydrogen evolution. (Figure 4 (iii) and (iv)) This anodic current was found to be associated with the oxidation reaction of DMAB on Pd particles. It was supposed that each Pd particle would act as a small catalyst for DMAB oxidation, enhancing the charge transfer at the interface. (iii) and (iv) in Figure 4 (a) demonstrated that Pd particles promoted the electro-oxidation of DMAB. The peak of the anodic current was increased from -0.54 mA/cm^2 to -2.11 mA/cm^2 with the increase of Pd particle density from 1.33×10^{10} #/cm^2 to 5.05×10^{10} #/cm^2. (Figure 4 (b)) The higher Pd particle density, the higher anodic current was detected.

Based on the result, substrates with various Pd particle densities were examined by the electrochemical analysis. The samples were randomly prepared by varying the process time and concentrations of species in the solution at each pretreatment step. The size of the Pd particles formed on the samples was in the range of 10 nm ~ 20 nm. Figure 5 illustrates the relationship between the peak current and the Pd particle density. The peak current of DMAB oxidation was found to be proportional to the Pd particle density and both were linearly dependent. Since only Pd acted as a catalyst for DMAB oxidation, the higher Pd particle density provided more

reaction sites for the oxidation, inducing the larger anodic current. Therefore, each Pd particle on the surface could be regarded as a small and real working electrode on the DMAB oxidation.

Many literatures describe the complex electron transfer reaction in the oxidation of DMAB. The oxidation reaction of DMAB is generally known to occur as shown in the following reactions.[20, 21] It has been reported that DMAB dissociates fast in an alkaline solution and forms hydroxytrihydroborate ion (BH_3OH^-):

$$(CH_3)_2NHBH_3(aq) + OH^-(aq) \rightarrow BH_3OH^-(aq) + (CH_3)_2NH(aq) \quad (1)$$

The BH_3OH^- is then oxidized electrochemically via two ways, 6-electron process (maximal efficiency):

$$BH_3OH^-(aq) + 6OH^-(aq) \rightarrow B(OH)^{4-}(aq) + 3H_2O(l) + 6e^- \quad (2)$$

Or 3-electron process (low efficiency), producing molecular hydrogen:

$$BH_3OH^-(aq) + 3OH^-(aq) \rightarrow B(OH)^{4-}(aq) + 3/2H_2(g) + 3e^- \quad (3)$$

The factors which determine whether the oxidation of DMAB follows either (2) or (3) are the transition metal surfaces used as catalysts.

BH3OH- also decomposes by following reaction:

$$BH_3OH^-(aq) + 3H_2O(l) \rightarrow B(OH)^{4-}(aq) + 3H_2(g) \quad (4)$$

The reaction (4) is a side-reaction and can be minimized by increasing pH of solution above 12.

Figure 6 depicts the peak current density as a function of the area of Pd particles exposed to the electrolyte. The peak current density was proportional to the area of Pd particles, which was measured from SEM images by using Scion image. The same trend observed in both Figure 5 and 6 demonstrated that the sizes of Pd particles were similar to each other even when the catalyzing method was changed.

The peak current density of DMAB oxidation can be calculated on the theoretical basis. It was assumed that the oxidation of DMAB on Pd particles was irreversible since the electro-oxidation of DMAB on Au was known to be an irreversible process by many literatures.[20-22] The equation of the theoretical peak current density (Ip) for an irreversible system is as follows:[23]

$$\text{Irreversible system: } I_p = (2.99 \times 10^5)n(\alpha n_a)^{1/2}AD^{1/2}C^*\upsilon^{1/2} \qquad (4)$$

Where D is the diffusion coefficient of DMAB, n is the number of electrons used in the process, A is the electrode area and C* is the concentration of DMAB (0.05 M). The scan rate (υ) was 0.02 V/s. The number of electrons (n) in the DMAB oxidation can be either 6 or 3, dependent on the reaction pathway (2) or (3). The charge transfer coefficient (α) and the number of electrons transferred in the rate-determining step (n_a) were fixed to 0.5 and 1, respectively.

As reported by D. Plana, et al. who studied the electro-oxidation of DMAB on Au, the calculated D value of DMAB was 1.7×10^{-5} cm^2/s, assuming n equal to 3.[20] Figure 6 shows I_p calculated by equation (4) when n and D are 3 and 1.7×10^{-5} cm^2/s. The values were slightly lower than the experimental results, however, both two cases were comparable. It means that the electro-oxidation of DMAB on Pd particles was also an irreversible process. The number of

electron transferred, n = 3, indicated that DMAB oxidized on Pd particles with low efficiency. (Reaction (3)) The DMAB oxidation through Reaction (3) normally accompanies the production of molecular hydrogen, resulting in hydrogen evolution which was clearly observed during the potential sweep. The lower calculated I_p values compared to the experimental results are possibly originated from the Pd area calculation. This is because the Pd area measured by Scion image was the projection area, assuming that Pd particles formed two-dimensionally. However, the actual shape of Pd particle might be rather similar to hemisphere than circle. If the calculation was preceded by considering the shape of Pd particle, higher I_p could be obtained. It was also supposed that other side reactions such as Ta oxidation might perturb the accurate measurement of the oxidation current of DMAB.

4. Optimization of catalyzing process

The optimization of the catalyzing process was then performed by using the relationship between the peak current density and Pd particle density. The experimental conditions for both the Sn sensitization and Pd activation were changed by varying HCl concentration and process time. The concentrations of $SnCl_2$ and $PdCl_2$ were maintained constant, at 30 mM and 0.6 mM, respectively. The calculated density and average size of Pd particles for each sample were listed in Table 1.

Figure 7 (a) and (b) show the linear sweep voltammograms on Pd-activated substrates

according to HCl concentration and immersion time in Sn sensitization process, respectively. As shown in Figure 7 (a), the peak current density was changed with HCl concentration and it reached the highest value at 60 ml/L of HCl. It was reported that the chloride ion (Cl^-) from HCl acted as a counter ion, affecting the size and zeta potential of Sn colloids in the solution.[24] Therefore, the size of Sn colloid was normally decreased when HCl concentration increased, and it was well-presented in Table 1. The size of Sn colloid is known to be directly related to the size of Pd particles since the displacement reaction occurs between Sn colloid and Pd^{2+} ion; the size of Pd particle was decreased with the increase of HCl concentration. The density was also changed with HCl concentration because the zeta potentials of Sn colloid and substrate were altered by the pH change in solution. It seemed that the attractive interactions between them were maximized at 60 ml/L of HCl. The slight peak shift observed in Figure 7 (a) might be due to the different chemical environment of Pd particles which was surrounded by Sn-containing chemicals.

The effect of Sn sensitization time at 60 ml/L of HCl was also tested as illustrated in Figure 7 (b). The peak current density reached its maximum when Sn sensitization time was 2 min and the positive peak shift was observed with the increase of immersion time, resulting from Ta oxidation. It was reported that Ta oxide film acting as an insulator appeared when Ta was immersed in aqueous solutions.[25] The thin Ta oxide film formed during the Sn sensitization might inhibit the current flow at the initial stage of the sweep, requiring higher potential for DMAB oxidation. Therefore, the growth of Ta oxide dependent on immersion time shifted the

oxidation peak to the positive direction in the potential. The highest oxidation current at 2 min might be originated from that the following: shorter immersion time than 2 min was not enough for Sn colloid to be adsorbed on the surface and longer time induced the detachment of Sn colloids on the surface that was oxidized in Sn sensitization solution.

The optimization of Pd activation was performed in the same way as Sn sensitization. Figure 8 (a) depicts linear sweep votammograms of Pd-activated substrates with varying HCl concentration in Pd activation solution. The highest peak was observed at 3 ml/L of HCl. It was uncertain why Pd particle density was decreased as HCl concentration increased, but it was inferred that the changes in zeta potentials of Pd particle and the substrate lead to the detachment of Pd particles. The slight peak shift caused by the chemical conditions of Pd particles was also observed.

The LSV affected by Pd activation time was also studied as shown in Figure 8 (b). The concentration of HCl was set to 3 ml/L. The highest peak current was obtained at 20 s which was then reduced as the time increased. Along with Pd activation time over 20 s, the average size of Pd particles and its standard deviation were increased with the decrease in Pd density. (Table 1) The maximum size of Pd particle observed at 300 s was over 60 nm which was 4 times larger than other ordinary Pd particles. This phenomenon was similar to the typical examples of Ostwald ripening. Ostwald ripening is normally derived by surface diffusion originated from the difference between surface energies of large and small particles under vacuum environment, resulting in the additional growth of large particles by consuming the small ones. It was also

suggested by P. P. Lau, et al. that it could appear in the electrolyte through dissolution and re-deposition process.[26] The noticeable peak shift was also observed in the cases of 120 s and 300 s, resulting from Ta oxidation during the immersion.

Therefore, from Figure 7 and 8, the optimized conditions for the maximum oxidation current peaks (the highest Pd particle density) were determined in the experimental range of 60 ml/L HCl with 2 min in Sn sensitization, and 3 ml/L HCl with 20 s in Pd activation. The Pd particle density was 5.05×10^{10} #/cm^2 (4% error).

5. Addition of PEG-3400 for the increase of Pd particle density

Pd particle density could be further increased by the addition of PEG-3400 to Sn sensitization solution as shown in Figure 9. It was found that the addition of 0.6 μM PEG-3400 increased both the Pd particle density to 6.83×10^{10} #/cm^2 (7% error) and the peak current to -2.9 mA/cm^2 at the optimized conditions mentioned above. PEG-3400 seemed to act as a surfactant and stabilizing agent for Sn colloids. It was supposed that PEG-3400 raised the affinity of substrate to water and enhanced the adsorption of Sn colloids as a consequence. This effect would be further investigated as an individual research with the zeta potential relation between Pd nanoparticles and Ta oxide surface.

6. Formation of Cu seed layer

Cu ELD was performed after the catalyzing process. To observe the effect of Pd particle density on Cu ELD, three substrates with Pd particle densities of (A) 1.33×10^{10} #/cm^2, (B) 5.05×10^{10} #/cm^2, and (C) 6.83×10^{10} #/cm^2 were prepared. Figure 10 illustrates the reciprocal sheet resistance change of the substrates with ELD time. The time for the increase in the reciprocal sheet resistance is normally regarded as the incubation time because the completion of Cu film can provide electrons with a continuous flow path, resulting in the decrease of sheet resistance. The reciprocal sheet resistance was not changed on A substrate even the ELD time was over 90 s. It means that a continuous Cu film was not formed after 90 s of Cu ELD. On the contrary, an increase in the reciprocal sheet resistance was observed from other samples. The incubation time of B was approximately 60 s and that of C was less than 40 s. It was found that the incubation time was decreased with the increase of Pd particle density, which indicated that the higher Pd particle density lead to the faster film formation.

The adhesion test (3M tape test) was also performed on A, B, and C. No flaking was observed on all seed layers because the adhesion strength of Pd on substrate was enough to stick the seed layer solidly. Some parts of deposited Cu were peeled in flakes when Cu ED was performed on the seed layers. The area of flakes was decreased as the Pd particle density increased, and the ED Cu film remained almost intact at the high Pd particle density (C). It seemed that higher Pd particle density provided higher adhesion strength of the deposited Cu film. The effect of Ta oxides itself, formed during the electrochemical sweep and dipping, on the adhesion strength

was almost negligible compared to that of the Pd particle density. It was considered that the amount of the Ta oxides were too small to affect the adhesion strength directly.

The thinnest Cu film was formed on the substrate C, which had the highest Pd particle density. The surface morphology of the Cu film and its cross section are shown in Figure 11. The continuous, 18-nm-thick Cu seed layer was deposited and its resistivity was 7.8 (± 0.9) μΩ·cm after annealing at 400℃ for 30 min in a N_2 atmosphere.

7. Conclusion

The electrochemical evaluation of Pd particle density with the oxidation current of DMAB was performed on Pd-activated Ta substrates. The oxidation current of DMAB was proportional to Pd particle density measured by SEM analysis. It was also found that the electro-oxidation of DMAB on Pd particles was an irreversible process producing 3 electrons per molecule. Using the electrochemical method as a tool to measure Pd particle density, the catalyzing process was optimized by controlling the process parameters of Sn sensitization and Pd activation. Through the optimization, a smooth 18-nm Cu seed layer with good adhesion was obtained at the thinnest thickness with the same deposition condition.

Table 1. The Density and Average Size of Pd Particles measured from SEM Images

Samples	Pd particle density $\times 10^{10}$ #/cm^2 (%error)	Average Pd diameter
(Fig. 7. (a)) 40 ml/L	1.70 (8%)	17 ± 6 nm
(Fig. 7. (a)) 60 ml/L	5.05 (4%)	14 ± 5 nm
(Fig. 7. (a)) 80 ml/L	2.31 (5%)	14 ± 5 nm
(Fig. 7. (a)) 100 ml/L	1.86 (5%)	13 ± 5 nm
(Fig. 7. (b)) 1 min	2.89 (6%)	18 ± 6 nm
(Fig. 7. (b)) 2 min	5.05 (4%)	14 ± 5 nm
(Fig. 7. (b)) 4 min	3.62 (7%)	16 ± 6 nm
(Fig. 8. (a)) 1.5 ml/L	4.93 (5%)	14 ± 5 nm
(Fig. 8. (a)) 3 ml/L	5.05 (4%)	14 ± 5 nm
(Fig. 8. (a)) 6 ml/L	2.84 (4%)	16 ± 5 nm
(Fig. 8. (a)) 12 ml/L	1.10 (4%)	18 ± 6 nm
(Fig. 8. (b)) 10 sec	4.52 (4%)	12 ± 4 nm
(Fig. 8. (b)) 20 sec	5.05 (4%)	14 ± 5 nm
(Fig. 8. (b)) 120 sec	4.23 (16%)	18 ± 7 nm
(Fig. 8. (b)) 300 sec	1.33 (24%)	20 ± 11 nm
(Fig. 9) w/o PEG	5.05 (4%)	14 ± 5 nm
(Fig. 9) w/ PEG	6.83 (7%)	13 ± 5 nm

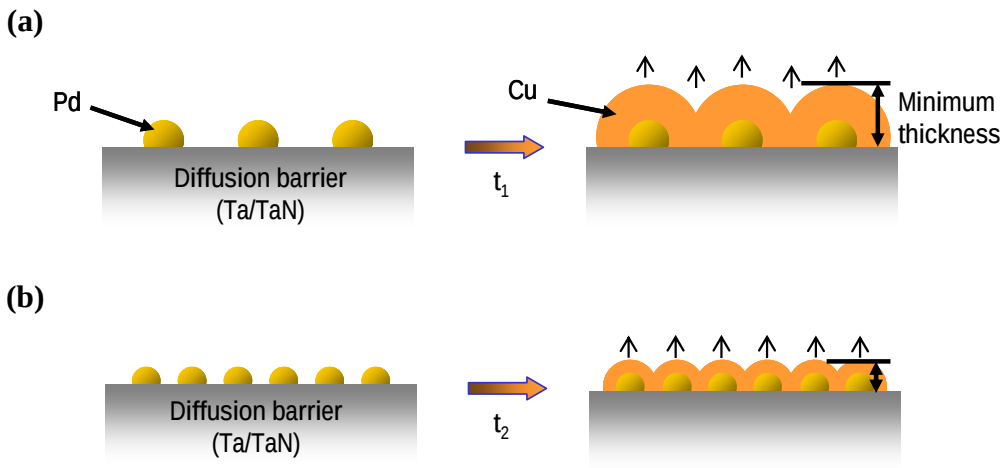

Figure 1. Schematic diagram of Cu growth in Cu ELD, (a) low and (b) high Pd particle density. The incubation time t_1 is longer than t_2 assuming that the deposition rate was same.

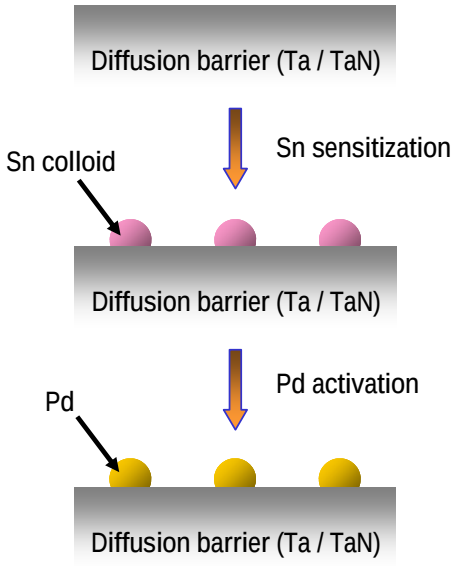

Figure 2. Schematic diagram of two-step activation.

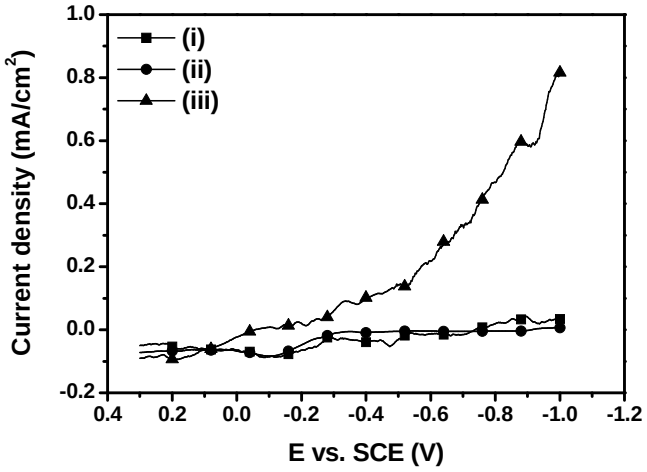

Figure 3. Linear sweep voltammograms of Ta substrates in KOH solution (pH 13.5), after (i) Ta oxide removal, (ii) Sn sensitization, and (iii) Pd activation.

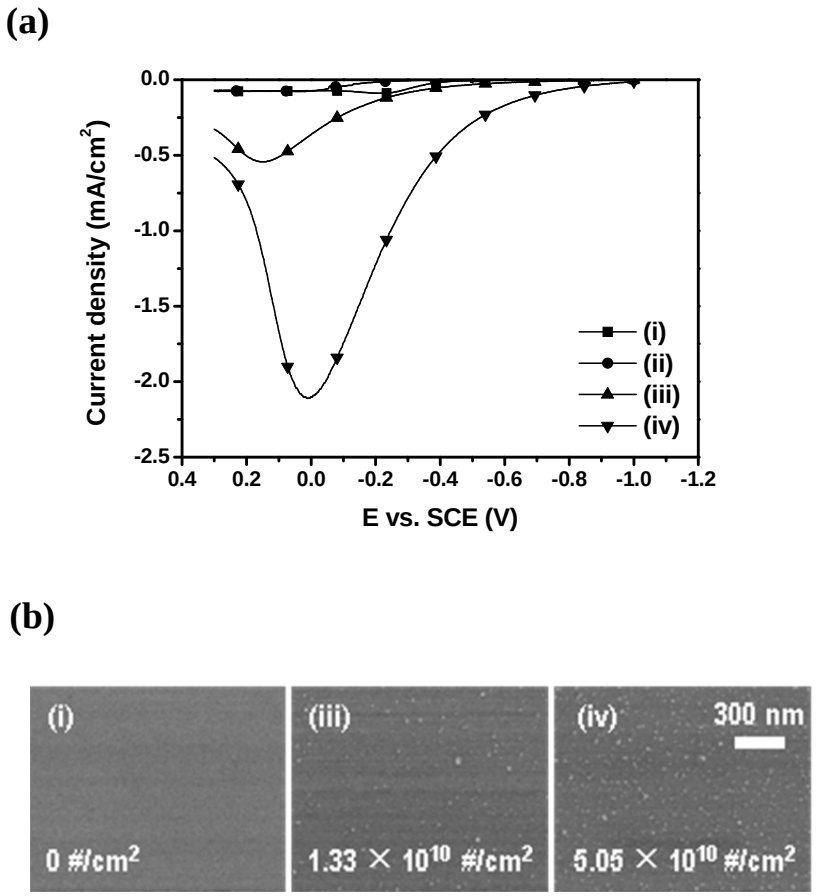

Figure 4. (a) Linear sweep voltammograms of Ta substrates in 0.05 M DMAB solution, after (i) Ta oxide etching, (ii) Sn sensitization, (iii) Pd activation with low Pd density, and (iv) Pd activation with high Pd density, (b) SEM images of Ta surfaces in (a). The experimental conditions of (a)-(iii) and (a)-(iv) were same as Figure 8 (b) 300 s and 20 s, respectively.

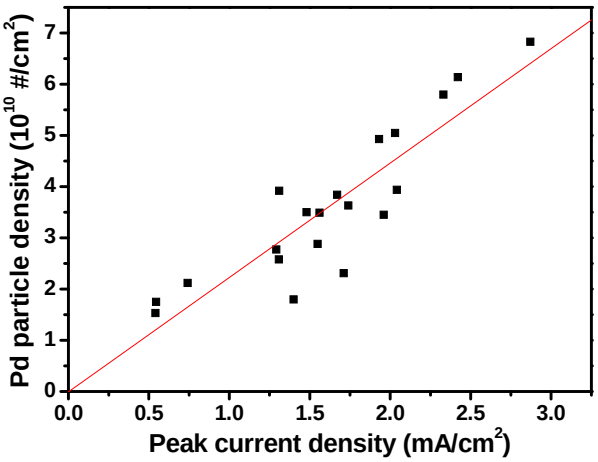

Figure 5. The correlation between the peak current density of DMAB oxidation and Pd particle density.

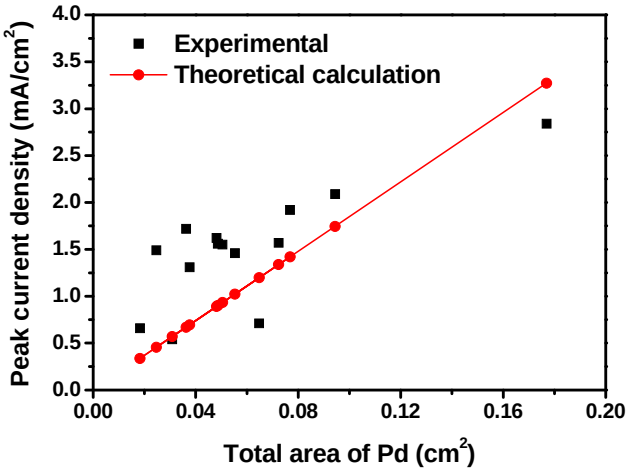

Figure 6. The correlation between the peak current density (I_p) of DMAB oxidation and the total area of Pd particles.

(a)

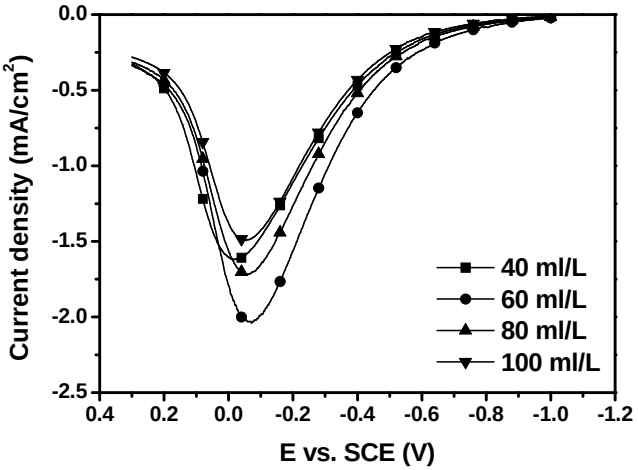

(b)

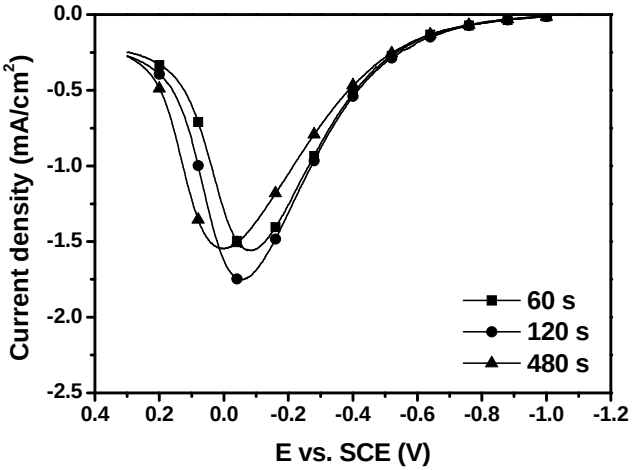

Figure 7. Linear sweep voltammograms of Pd-activated Ta substrates in 0.05 DMAB with (a) various HCl concentrations and (b) process times in Sn sensitization. The process time of (a) was 2 min.

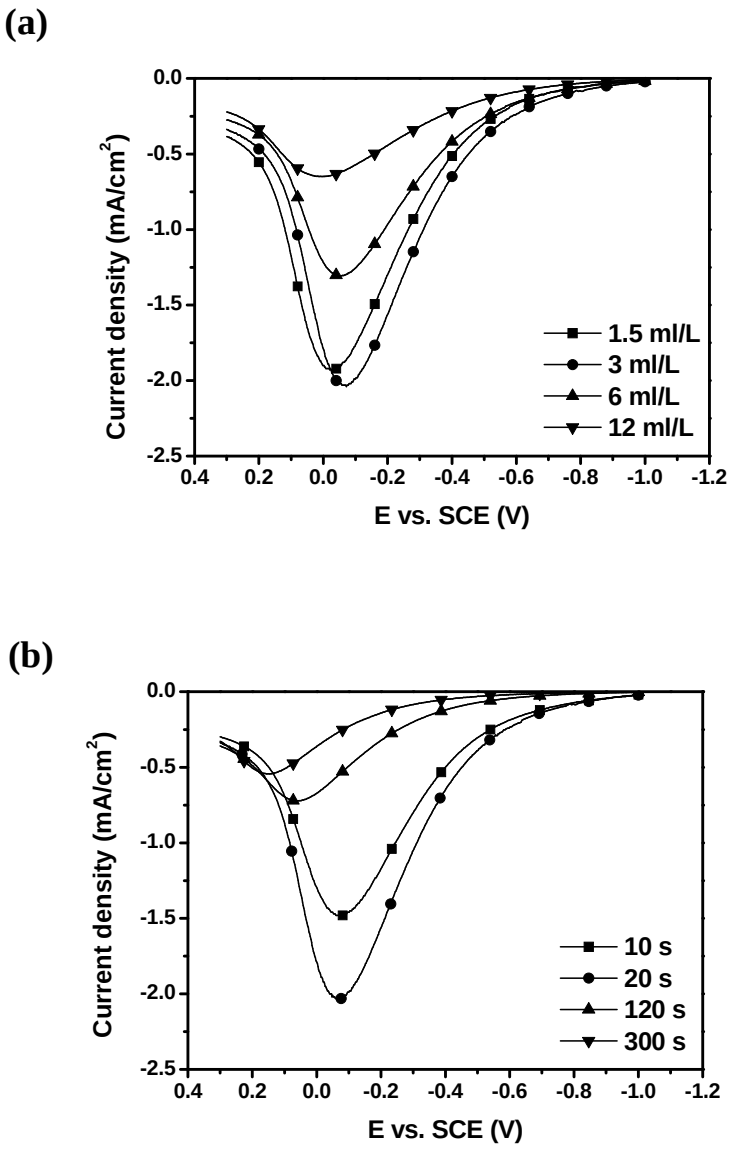

Figure 8. Linear sweep voltammograms of Pd-activated Ta substrates in 0.05 DMAB with (a) various HCl concentrations and (b) process times in Pd activation. The process time of (a) was 20 s.

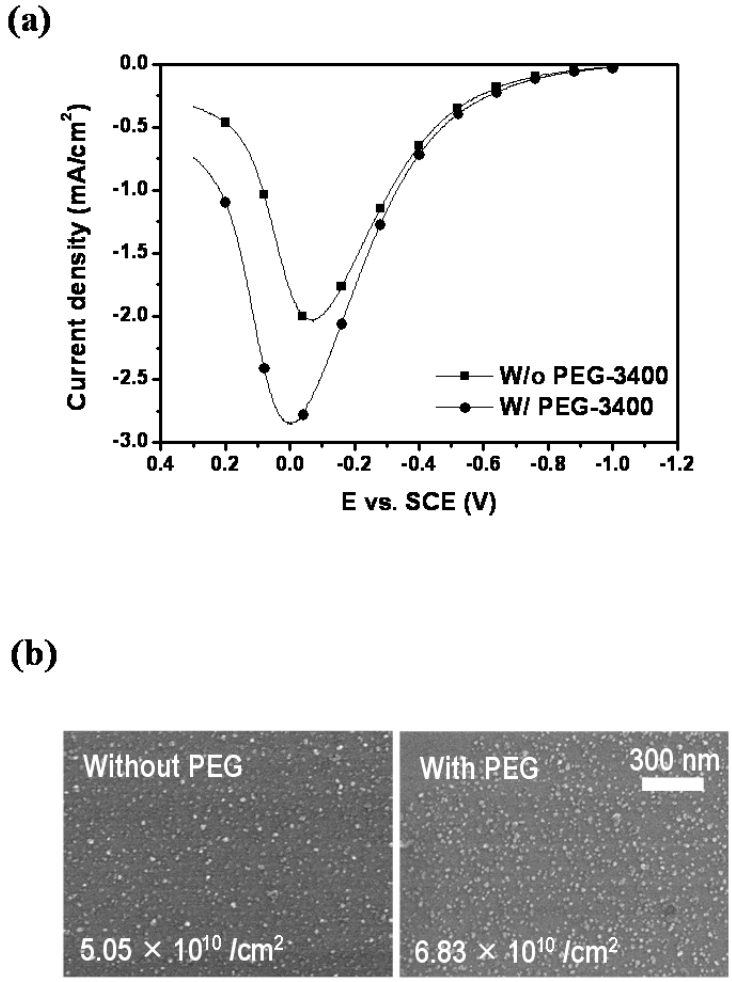

Figure 9. (a) Linear sweep voltammograms and (b) SEM images of Pd-activated Ta substrates in 0.05 DMAB when 0.6 μM of PEG-3400 was added to Sn sensitization solution.

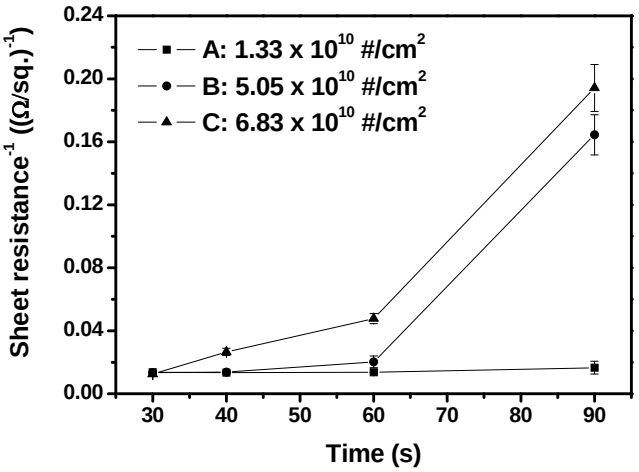

Figure 10. The reciprocal sheet resistance change of substrates according to ELD time.

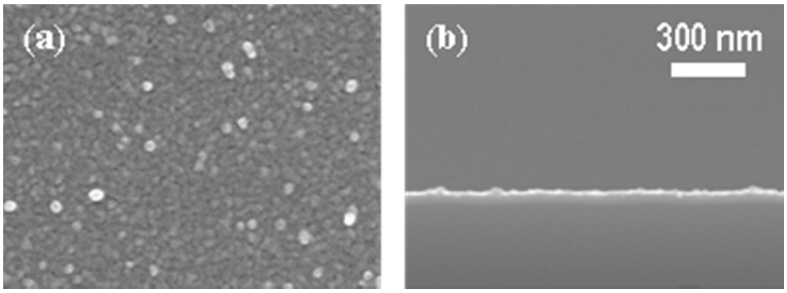

Figure 11. SEM images of the electroless Cu film on Ta substrate, (a) surface and (b) cross section after Cu ELD for 90 s.

References

1. K. Rahmat, O. S. Nakagawa, S.-Y. Oh, and J. Moll, *IEEE IEDM Tech. Dig.*, **245** (1995).
2. N. M. Martyak and P. Ricou, *Mater. Sci. Semi. Proc.*, **6**, 225 (2003).
3. J. Reid, *Jpn. J. Appl. Phys.*, **40**, 2650 (2001).
4. C. H. Lee, S. Hwang, S. C. Kim, and J. J. Kim, *Electrochem. Solid-State Lett.*, **9**, C157 (2006).
5. T. Smy, L. Tan, S. K. Dew, and M. J. Brett, *J. Electrochem. Soc.*, **144**, 2115 (1997).
6. H. T. Ng, S. F. Y. Li, L. Chan, F. C. Loh, and K. L. Tan, *J. Electrochem. Soc.*, **145**, 3301 (1998).
7. R. Sard, *J. Electrochem. Soc.*, **117**, 865 (1970).
8. S. Y. Chang, C. W. Lin, H. H. Hsu, J. H. Fang, and S. J. Lin, *J. Electrochem. Soc.*, **151**, C81 (2004).
9. R. L. Meek, *J. Electrochem. Soc.*, **122**, 1177 (1975).
10. T. Osaka and H. Takematsu, *J. Electrochem. Soc.*, **127**, 1021 (1980).
11. Y.-C. Sung, C.-H. Lai, S.-J. Lin, and S.-Y. Chang, *Electorochem. Solid-State Lett.*, **9**, C85 (2006).
12. X. Wu and W. Sha, *Appl. Surf. Sci.*, **255**, 4249 (2009).
13. J. P. Marton and M. Schlesinger, *J. Electrochem. Soc.*, **115**, 16 (1968).
14. C. H. Lee, S. H. Cha, A. R. Kim, J. H. Hong, and J. J. Kim, *J. Electrochem. Soc.*, **154**,

D182 (2007).

15. J. Horkans, C. Sambucetti, and V. Markovich, *IBM. J. Res. Develop.*, **28**, 690 (1984).
16. S. P. Chong, Y. C. Ee, Z. Chen, and S. B. Law, *Surf. Coat. Technol.*, **198**, 287 (2005).
17. F. Delaunois, J. P. Petitjean, P. Lienard, and M. Jacob-Duliere, *Surf. Coat. Technol.*, **124**, 201 (2000).
18. T. Homma, A. Tamaki, H. Nakai, and T. Osaka, J. Electroanal. Chem., 559, 131 (2003).
19. G. Andreasen, A. Visintin, R. C. Salvarezza, W. E. Triaca, and A. J. Arvia, *Langmuir*, **15**, 1 (1999).
20. D. Plana and R. A.W. Dryfe, *Electrochim. Acta*, **56**, 3835 (2011).
21. L. C. Nagle and J. F. Rohan, *Electrochem. Solid-State Lett.*, **8**, C77 (2005).
22. O. A. Sadic, H. Xu, and A. Sargent, *J. Electroanal. Chem.*, **583**, 167 (2005).
23. P. T. Kissinger and W. R. Heineman, *Laboratory Techniques in Electroanalytical Chemistry*, 2nd ed., p. 82, Marcel Dekker, Inc., New York, USA (1996).
24. V. E. G. Leuze and B. Saulgau, *Electroplating and Electroless Plating of Copper & its Alloys*, p. 138, CPI-Bookcraft, Bath, UK (2003).
25. M. Mahe, D. Devilliers, H. Groult, and J. Pouilleau, *Electrochim. Acta*, **44**, 2307 (1999).
26. P. P. Lau, C. C. Wong, L. Chan, A. See, and S. B. Law, *J. Electrochem. Soc.*, **151**, C436 (2004).
27. L. Bousse, S. Mostarshed, B. V. D. Shoot, N. F. D. Rooij, P. Gimmel, and W. Gopel, J. *Colloid Interface Sci.*, **147**, 22 (1991).

28. C. P., S. H. Y. Lo, C.-C. Wan, Y.-Y. Wang, *Collid. Surface. A*, **308**, 93 (2007).

Appendix II

Multiple activation for the increase in Pd particle density

The surface activation step was repeated several times to increase Pd particle density prior to Cu electroless deposition. The scheme of multiple activation was shown in Figure 12. It was planned to increase the number of Pd particles by repeating Sn sensitization-Pd activation steps several times. The density was increased with the increase in the number of repeated cycles, however, the size distribution of Pd particles was not uniform. The non-uniform distribution resulted in the rough surface of the film after the electroless deposition.

1. Multiple activation

The surface activation step was the two-step activation, which was explained in the experimental section in Appendix I. The substrate was a <Ta (PVD, 7 nm) / SiO_2> blanket coupon wafer. The two-step activation was performed twice for the increase in the Pd particle density. Figure 13 shows SEM images after the double activation. The Pd particle density was slightly increased with the double activation as shown in Figure 13 (b). However, the average size of Pd particles was increased from 15 (±6) nm to 19 (±11) nm, and the agglomerated

particles were frequently observed on the surface. The increase in the total Pd activation time seemed to affect the agglomeration, as it was revealed that the increase in the Pd activation time resulted in the increase in the average Pd particle size. (Appendix I) Therefore, the total Pd activation time was reduced to 20 s by fixing the Pd activation time at 10 s in one cycle. The surface image was shown in Figure 13 (c). In that case, the agglomerated Pd particles were rarely observed though the average size of Pd particles was still larger (18 (±6) nm) than that of the single activation. The Pd particle density was also slightly increased compared to Figure 13 (b).

It was observed that the decrease in the Pd activation time in the double activation step reduced the agglomerated Pd particles. Therefore, the total Pd activation time was further reduced to 10 s. Figure 14 shows the surface images with the number of activation steps at the fixed total Pd activation time (10 s). The highest Pd particle density was obtained when the double activation was performed. The triple activation might increase the absolute number of Pd particles, however, most of them were agglomerated with each other.

2. Formation of Cu seed layer

Cu ELD was performed on the double-activated substrate. Figure 15 shows the change in the reciprocal of sheet resistance according to the deposition time. The reciprocal of sheet resistance of the double-activated substrate increased faster than that of the single-activated substrate,

which indicated that the thinner Cu film could be obtained on the double-activated substrate. However, the surface was too rough due to the agglomerated Pd particles.

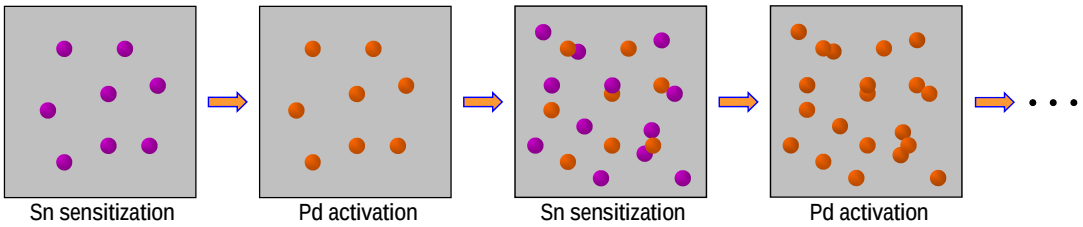

Figure 12. The scheme of multiple activation.

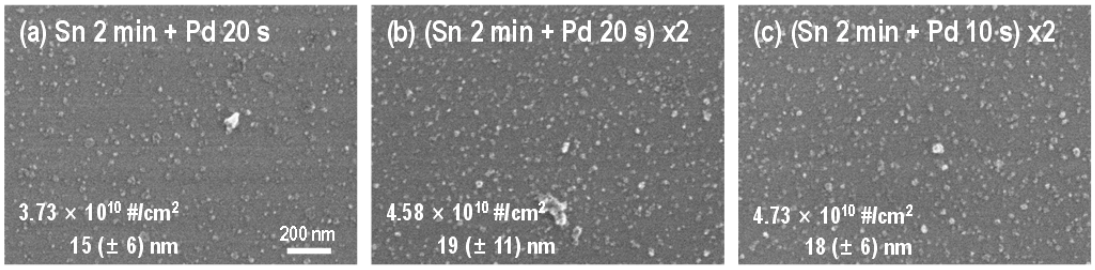

Figure 13. Surface images after (a) the single activation, (b) the double activation with 20 s of Pd activation time, and (c) with 10 s of Pd activation time. The time of Sn sensitization was fixed at 2 min.

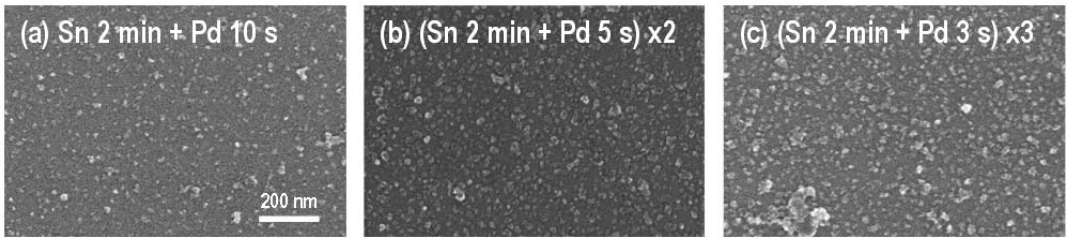

Figure 14. Surface images after (a) the single activation, (b) double activation, and (c) triple activation.

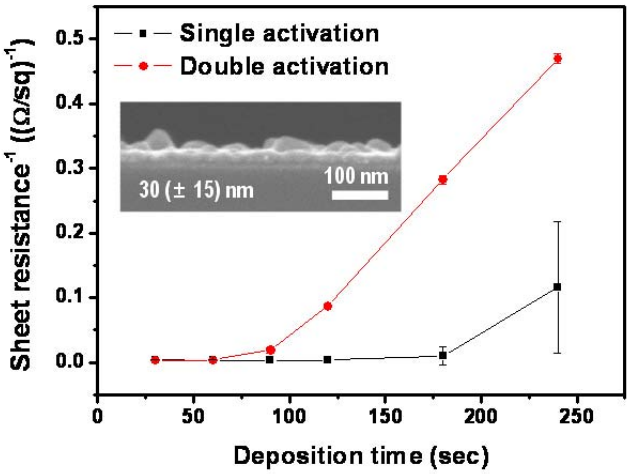

Figure 15. The change in the reciprocal of sheet resistance of the substrate according to the deposition time.